UC Berkeley
UC Berkeley Electronic Theses and Dissertations

Title
Characterization of Thallium Bromide (TlBr) for Room Temperature Radiation Detectors

Permalink
https://escholarship.org/uc/item/3rp4n06c

Author
Smith, Holland McTyeire

Publication Date
2013

Peer reviewed|Thesis/dissertation

eScholarship.org Powered by the California Digital Library
University of California

Characterization of Thallium Bromide (TlBr) for Room Temperature Radiation Detectors

by

Holland McTyeire Smith

A dissertation submitted in partial satisfaction of the
requirements for the degree of
Doctor of Philosophy

in

Engineering - Materials Science and Engineering

in the

Graduate Division

of the

University of California, Berkeley

Committee in charge:

Professor Eugene Haller, Chair
Professor Daryl C. Chrzan
Professor Eric Norman

Spring 2013

Characterization of Thallium Bromide (TlBr) for Room Temperature Radiation Detectors

Copyright 2013
by
Holland McTyeire Smith

Abstract

Characterization of Thallium Bromide (TlBr) for Room Temperature Radiation Detectors

by

Holland McTyeire Smith

Doctor of Philosophy in Engineering - Materials Science and Engineering

University of California, Berkeley

Professor Eugene Haller, Chair

Thallium bromide (TlBr) has emerged as a remarkably well-suited material for room temperature radiation detection. The unique combination of high-Z elements, high density, suitable band gap, and excellent electrical transport properties present in TlBr have brought device performance up to par with CdZnTe (CZT), the current market-leading room temperature radiation detector material. TlBr research is at an earlier stage than that of CZT, giving hope that the material will see even further improvement in electronic properties.

Improving a resistive semiconductor material requires knowledge of deep levels present in the material and the effects of these deep levels on transport properties. Very few deep level studies have been conducted on TlBr, and none with the depth required to generate useful growth suggestions. In this dissertation, deep levels in nominally undoped and doped TlBr samples are studied with electrical and optical methods. Photo-Induced Conductivity Transient Spectroscopy (PICTS) is used to discover many deep levels in TlBr electrically. These levels are compared to sub-band gap optical transitions originating from defects observed in emission spectra. The results of this research indicate that the origin of resistivity in TlBr is likely due to deep level defects pinning the Fermi level at least $\sim$0.7 eV from either the conduction or valence band edge. The effect of dopants and deep levels on transport in TlBr is assessed with microwave photoconductivity decay analysis. It is found that Pb-, Se-, and O-doping decreases carrier lifetime in TlBr, whereas C-doping does not.

TlBr exhibits weak ionic conductivity at room temperature, which both negatively affects the leakage current of detectors and leads to device degradation over time. Researchers are actively looking for ways to reduce or eliminate the ionic conductivity, but are faced with an intriguing challenge of materials engineering: is it possible to mitigate the ionic conduction of TlBr without harming the excellent electronic transport properties? Doping TlBr in order to control the ionic conductivity has been proposed and shown to be effective in reducing dark ionic current, but the electronic effects of the dopants has not been previously studied in detail. In this dissertation, the electronic effects of dopants introduced for ionic reasons are evaluated.

Contents

Contents **i**

1 Introduction **1**
1.1 Motivation: Radiation Detection for Homeland Security 1
1.2 Semiconductor Radiation Detectors 2
1.2.1 Principles of Operation 2
1.2.2 Room Temperature Operation 4
1.2.3 Resistive Detectors 5
1.2.4 Materials Requirements of Resistive Detectors 5
1.2.5 The “Right” Kind of Resistivity 7
1.3 Thallium Bromide (TlBr): A Promising Material for Resistive Detectors . . 7
1.3.1 TlBr compared to Cadmium Zinc Telluride ($Cd_{1-x}Zn_xTe$) 8
1.3.2 Growth of TlBr 9
1.3.3 Electrical Transport Properties 11
1.3.4 Outstanding Challenges 11
1.4 Conclusion: Opportunities for Materials Engineering 12

2 Photo-Induced Conductivity Transient Spectroscopy (PICTS) **13**
2.1 Experimental Detection of Deep Levels 13
2.1.1 Capture and Emission Kinetics 14
2.1.2 Thermally Stimulated Conductivity (TSC) and Deep Level Transient Spectroscopy (DLTS) 15
2.2 Photo-Induced Conductivity Transient Spectroscopy (PICTS) 17
2.2.1 Experimental Overview 17
2.2.2 PICTS Data Analysis: Two-Gate and Four-Gate Technique 19
2.3 Building a Modern PICTS Measurement System 20
2.3.1 Instrumentation 20
2.3.2 Control Software 23
2.3.3 Data Analysis Software 25
2.4 PICTS Results on Semi-Insulating Gallium Arsenide (SI GaAs) 25
2.4.1 Sample Preparation 25
2.4.2 PICTS Results 26

2.4.3 Comparison with Literature . . . 26
2.5 Conclusion . . . 27

3 Electrical Characterization of Deep Levels in TlBr 29
3.1 Background and Theory . . . 29
3.2 Experimental Methods . . . 31
3.3 PICTS on Nominally Undoped TlBr . . . 33
3.3.1 Description of Nominally Undoped Samples . . . 33
3.3.2 Glow Discharge Mass Spectroscopy of Nominally Undoped TlBr Samples 34
3.3.3 PICTS of Nominally Undoped Samples below 250 K . . . 35
3.3.4 PICTS Signal Behavior above 250 K . . . 37
3.4 PICTS on Doped TlBr: TlBr:C, TlBr:O . . . 39
3.4.1 Description of Doped Samples . . . 39
3.4.2 Secondary Ion Mass Spectrometry (SIMS) of TlBr:C and TlBr:O . . . 40
3.4.3 PICTS on TlBr:C . . . 40
3.4.4 PICTS on TlBr:O . . . 43
3.5 Discussion of Results . . . 44
3.5.1 Traps in Common . . . 44
3.5.2 Implications for the Origin of Resistivity in TlBr . . . 45
3.6 Conclusion . . . 47

4 Optical Characterization of Deep Levels in Doped and Undoped TlBr 48
4.1 Background and Theory . . . 48
4.2 Experimental Methods . . . 50
4.2.1 Sample Preparation . . . 50
4.2.2 Photoluminescence System Description . . . 51
4.3 Photoluminescence Results . . . 51
4.3.1 PL of Nominally Undoped TlBr . . . 51
4.3.2 PL of TlBr:C . . . 52
4.3.3 Cathodoluminescence System Description . . . 54
4.4 Cathodoluminescence Results . . . 54
4.4.1 CL of Nominally Undoped TlBr . . . 54
4.4.2 CL of TlBr:C . . . 54
4.4.3 CL of TlBr:O . . . 56
4.5 Comparison of PICTS and Luminescence Data . . . 57
4.6 Conclusion . . . 58

5 Carrier Lifetime in Doped and Undoped TlBr 59
5.1 Introduction . . . 59
5.1.1 Measuring the $\mu\tau$ product and mobility . . . 59
5.1.2 Measuring carrier lifetimes . . . 60
5.1.3 MWPC as a tool to assess the relative quality of TlBr samples . . . 61

5.2 Experimental . . . 62
5.2.1 Samples measured . . . 62
5.2.2 Experiment Description . . . 62
5.3 Results and Discussion . . . 63
5.3.1 Nominally Undoped TlBr . . . 63
5.3.2 TlBr:O, TlBr:Pb, TlBr:Se . . . 66
5.3.3 TlBr:C . . . 67
5.4 Conclusion . . . 68

6 Dopant Mitigation of Ionic Conductivity in TlBr 70
6.1 Background and theory . . . 70
6.2 Experimental . . . 72
6.2.1 Samples Used . . . 72
6.2.2 Measurement Details . . . 73
6.3 Results and Discussion . . . 73
6.3.1 PICTS on Pb- and Se-doped TlBr . . . 73
6.3.2 CL on Pb- and Se-doped TlBr . . . 73
6.3.3 Comparison of PICTS and CL . . . 75
6.3.4 MWPC on Pb- and Se-doped TlBr . . . 77
6.3.5 Forming the Picture of Mid-Gap States . . . 77
6.4 Conclusion and Future Outlook . . . 77

7 Conclusions and Future Work 79

Bibliography 82

A Polymorphism of TlBr and First Principles Band Structure Calculations 93
A.1 The Polymorphism of TlBr . . . 93
A.2 Phase Stability and Band Structures for TlBr(I), TlBr(II), and TlBr(III) . . 94
A.2.1 Description of Density Functional Theory Calculations . . . 94
A.2.2 Summary of Results . . . 95
A.2.3 Comparison of Calculated Band Structures and Experiments . . . 96
A.3 Conclusion . . . 96

B *Mathematica* Notebook for PICTS Analysis 98
B.1 PICTS Analysis Notebook . . . 98
B.2 Additional Functions Used in PICTS Analysis Notebook . . . 112

C *Mathematica* Notebook for Calculation of Photo-Generated Free Carrier Concentrations in MWPC Experiments 116

Acknowledgments

My graduate school experience was enriched by many generous and talented people, without whom the completion of this work would not have been possible.

First, I would like to acknowledge Professor Eugene Haller. Professor Haller's amazing scientific accomplishments and ethics are matched by an unwavering dedication to his students. His warmth of personality, rigorous standards, and breadth of interests serve as a role model to me of how a scientist should be. I truly feel lucky to have been a part of his group.

I am indebted to Daryl Chrzan for serving as my second research advisor, and lending computational punch to my experimental data. I would also like to acknowledge the outstanding classes taught by Professor Chrzan. MSE 102, 202, and 215 were simply among the best classes I have ever taken, thanks to the immense effort and care Professor Chrzan puts into teaching. I also greatly benefitted from collaborating with Professor Nancy Haegel from the Naval Postgraduate School. I am thankful for her sharp scientific acumen and willingness always to discuss a subject further or to read another draft. Our joint publications were immensely improved by her insightful eye.

I would like to acknowledge Nate Miller and Joel Ager for giving me my first job in science, when I was still an undergraduate at Berkeley. My days of working on and admiring experimental equipment Nate had built were formative for my later trajectory in graduate school. I also acknowledge the great personal support provided by the graduate students mentoring me during my first summer at the lab - Nate Miller, Joe Wofford, Peter Stone, Marie Mayer, Robert Broesler, and Doug Detert. This group of brilliant people provided me with many educational and/or entertaining interactions. It was a pleasure to work with all of them and bittersweet to see them graduate.

I would also like to acknowledge current Haller group members Erin Ford and Karen Bustillo. Our radiation detector project benefitted from Erin's dedication and skill at growing PbO. Karen Bustillo provided kind personal support and encouragement. She also generously kept the laser lab running, which was essential for many of my experiments.

Speaking of experiments, I would like to acknowledge Dr. Hans Bechtel for helping me with FTIR experiments at the Advanced Light Source, and Dr. Antonio DiPasquale for low temperature XRD measurements in the Department of Chemistry at Berkeley. I would like to thank Dr. Ian Sharp for generously allowing me to use his microwave photoconductivity measurement system. Austin Arey helped me build my PICTS system.

I am deeply indebted to Jeff Beeman for any number of things. First and foremost, the construction of the PICTS system described in this dissertation would have been impossible without his guidance and technical genius. Jeff was also always available for personal discussions, where his humor and deep wisdom was much appreciated. I would like to thank Bill Hansen for his expert chemical knowledge, and his constant consumption of scientific literature that led to many relevant articles being placed in my mailbox. I must also thank David Hom for all of the work he did (much of which I will never know about) to keep my life at the lab running smoothly. David always knew how to accomplish anything at the lab - the kind of guy you are glad to have on your side.

I would like to thank Professor Oscar Dubon for his warmth and encouragement when I was an undergraduate to continue on to graduate school in Materials Science. I acknowledge Professor Mark Asta for doing an excellent job serving as my Graduate Advisor. His door was always open and he was very helpful when I needed advice navigating the department. I am also grateful to Professor Eric Norman from Nuclear Engineering for serving on my Qualifying Exam and Dissertation Committee.

I would like to thank Len Cirignano, Guido Ciampi, and Hadong Kim from Radiation Monitoring Devices for providing TlBr and working with me to prepare the samples in the best way for electrical and optical measurements. Without the TlBr, this dissertation simply would not exist.

I would like to acknowledge the support of my family. My mother, and father, and sister have provided me with much love and support throughout my long educational history. My golden retriever Turbo has been a beloved companion throughout my time at Berkeley, bringing me joy through our daily walks. Finally, I would like to thank Cela Smith for the personal and emotional support for most of my time at Berkeley.

I was supported by the Office of Naval Research through a National Defense Science and Engineering Graduate Fellowship. Additional support for this work was provided by the US Department of Homeland Security under the Grant Award number 2009-DN-077-ARI-026-04. Some equipment used at LBNL was funded by Director, Office of Science, Office of Basic Energy Sciences, Materials Science and Engineering Division of the U.S. Department of Energy under contract No. DE-AC02-05CH11231.

Chapter 1

Introduction

1.1 Motivation: Radiation Detection for Homeland Security

A heightened awareness of potential terrorist threats is an unfortunate fact of living in modern times. Foiled plots and exposed risks are frequently reported in the news. Color-coded threat level reminders urge vigilance. With the fall of the Soviet Union and the consequent relaxation of control mechanisms, serious concern has arisen among security experts about the large supply of radioactive isotopes in Russia and former Soviet Republics. The supply includes weapons-grade plutonium and uranium that have attracted the interest of terrorist groups. Between 1993 and 2003, the International Atomic Energy Agency (IAEA) reported 884 incidents of illicit trafficking of nuclear and other radioactive materials.[1] The greatest concern about these materials is their potential for use in a radioactivity dispersal device, or "dirty bomb." Dirty bombs are simple to make, requiring only a conventional explosive, and present devastating psychological and physical consequences if detonated in a populous area. The risk of a terrorist group acquiring conventional nuclear weapons is considered smaller, as such weapons are nearly impossible for a small group to build from raw materials and are much more difficult to steal and transport.

The Department of Homeland Security (DHS) in the United States is tasked with the prevention of terrorist threats, relying on a combination of intelligence work and technology. As part of a prevention plan for dirty bombs, the DHS identifies and monitors potential sources of radioactive material. With domestic sources, the DHS has the necessary authority to implement sufficient regulatory practices. However, it is often the case that the DHS has no ability to monitor in areas of high risk, such as sites in former Soviet Republics. For this reason, a detection system must be in place for all points of entry into the country where such material might be smuggled.

The radioactive material in a dirty bomb emits a characteristic spectrum of decay products including alpha, beta, and gamma radiation. A detector with sufficient energy resolution can fingerprint the energies of these decay products, identifying their source as illicit even

against a background of naturally occurring radioactive materials. A small component of Homeland Security's interdiction program for dirty bombs therefore involves installing radiation detectors at ports and shipping terminals across the United States. Systems in place today consist of three stages of detection. The first stage is the channeling of all passengers and cargo entering the country through radiation portal monitors (RPM). These are large walk-through or drive-through devices equipped with many types of detectors optimized for gamma and neutron detection (see Figure 1.1). RPMs act as counters and do not have high energy resolution. A positive "hit" from an RPM means that the person or cargo passing through needs to be investigated further. In the second stage of inspection, hand-held gamma and neutron search detectors are used to pinpoint the location of the source of ionizing radiation. In the third and final stage, a radionuclide identification device (RID) with high energy resolution is used to fingerprint the emission spectrum and thus chemically identify the source of radiation. Examples of RIDs are shown in Figure 1.2. It is at this third stage that a potentially illicit ^{137}Cs source would be distinguished from a common medical isotope such as ^{99}Tc. Ideally, identification devices should be small and cheap, and able to be distributed widely with low cost and maintenance.

Figure 1.1: A radiation portal monitor (RPM) at an airport.

1.2 Semiconductor Radiation Detectors

1.2.1 Principles of Operation

A simple radiation detector must satisfy at the minimum two requirements: it must indicate the presence and absence of ionizing radiation. These are the "on" and "off" states of the device. The ability to discriminate between emission spectra from different sources imposes a third requirement on the device - it must produce a response proportional to the

Figure 1.2: A selection of hand-held radionuclide identification devices.

energy of the incident ionizing radiation. Security applications in particular require high energy resolution. Figure 1.3 shows the necessity of high energy resolution to detect an illicit isotope against a background of other non-illicit sources.

Semiconductors have proven ideally suited for radiation detection. The general principles of operation of a semiconductor detector are as follows:

1. A large bias is placed across the device. A very small leakage current flows, which is minimized either by the use of a p-n (or p-i-n) junction architecture, or the use of a material with high resistivity. This is the "off" state of the device.

2. Incident ionizing radiation strikes the device and generates electron-hole pairs. The number of pairs created is proportional to the energy of the incident radiation.

3. The electric field in the device sweeps the generated carriers to the contacts. The concentration of electron-hole pairs created by the ionizing radiation is much greater than the background free carrier concentration. The time resolved current flowing through the device, or the charge collected across a summing capacitor after the strike, serves as the detector response. This is the "on" state of the device.

As introduced previously, an ideal detector response should indicate not only the presence of ionizing radiation, but the energy of the incident radiation as well. With semiconductors, this proportionality is achieved by the fact that ionizing radiation events generate a number of electron-hole pairs that is proportional to the incident energy of the radiation. Thus, for a semiconductor material, an electron-hole pair (EHP) creation energy can be measured which quantifies the amount of free charge that will be generated by an ionizing event of a given energy. The EHP creation energy has been found to be proportional to the band gap of the

material.[2] It is thus possible to measure the energy of incident radiation on a detector by collecting and counting the charge created by a single event.

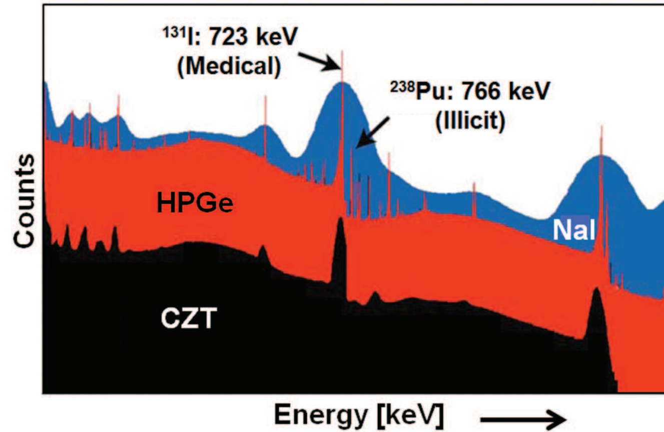

Figure 1.3: Emission spectra taken with three different detectors from a mixed source containing a medical isotope ^{131}I and an illicit isotope ^{238}Pu. These two isotopes emit gamma rays with similar energies: 723 keV and 766 keV. The NaI scintillator and CZT semiconductor detector have insufficient energy resolution to resolve the two closely spaced peaks. Only the high-purity germanium detector can resolve them clearly. Adopted after reference [3].

1.2.2 Room Temperature Operation

Semiconductor detectors have achieved the greatest energy resolution of all detection techniques, better than gas ionization chambers and scintillators.[4] Historically, germanium detectors hold the record for the best energy resolution ever obtained among semiconductor detectors for gamma rays with energies of hundreds of keV. However, germanium's relatively small bandgap means that a Ge detector must be cooled below ∼150 K, as detectors are operated under high bias and the thermal leakage current of germanium swamps the detector signal at room temperature. Additionally, germanium is a light element relative to many other elements used in semiconductor detectors. The stopping distance of ionizing radiation in matter depends strongly on the atomic number Z of the constituent atoms. Over the energy range in which photoelectric absorption is the dominant stopping mechanism, the dependence is as strong as $Z^{\sim 4.5}$. Thus, Ge detectors must be larger than detectors comprised of heavier elements in order to have equivalent stopping power. For security applications, researchers have sought materials with higher Z and a higher bandgap than germanium to make small detectors, capable of operating at room temperature, with excellent energy resolution.

1.2.3 Resistive Detectors

Germanium detectors are based on diode designs that take advantage of the phenomenal purity crystal growers have achieved. In such a design, the p-n junction ensures that minimal leakage current flows under high reverse bias. The depletion layer in a typical germanium detector under a few thousand volts reverse bias is up to several centimeters thick. This can only be achieved with a semiconductor material that has an extremely low net concentration of electrically-active shallow level impurities - around 10^{10} cm^{-3}.[5] Only germanium and silicon have been grown with the requisite purity to make diode detectors of significant size. These stringent purity requirements rule out the use of the large diode device structure for other, less-pure semiconductors.

Resistive semiconductor detectors present an alternative to diode detectors. In the absence of radiation, a resistive detector acts simply as a resistor. The leakage current that flows through a resistive device upon application of a bias V is given by Ohm's law. When ionizing radiation strikes the device however, large amounts of electron-hole pairs are created and separated by the applied electric field. The resulting sharp increase in current defines the "on" state of the detector. These priniciples are illustrated in Figure 1.4.

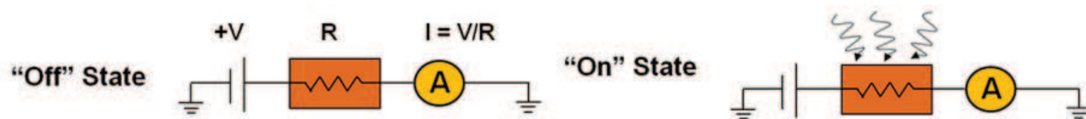

Figure 1.4: The operational principles of a resistive semiconductor radiation detector. In the off state, very little current flows due to large R. In the "on" state, ionizing radiation generates large amounts of electron hole pairs that flow as current.

Most "new" materials being investigated today for room temperature radiation detectors are materials that are suitable as a resistive device, as opposed to a junction device. This is because there are many more semiconductors that can be made highly resistive than those that can be grown intrinsically pure, or easily doped both p- and n-type to make a high quality junction.

1.2.4 Materials Requirements of Resistive Detectors

The important materials properties governing device performance for resistive detectors are:

- Resistivity
- Band gap
- Density

- Average Z
- $\mu_{(e,h)}\tau_{(e,h)}$ - the mobility-lifetime products of charge carriers

The resistivity must be high enough to ensure that the leakage current is small compared to the expected signal current. The higher the resistivity of the material, the better the “off” state of the device. The band gap should be high enough so that the quantity of thermally generated charge carriers is much smaller than the quantities produced by ionizing radiation in the energy range of interest. However, higher band-gaps also lead to higher electron-hole pair creation energies, which in turn reduce the magnitude of the detector signal. Thus, a band-gap range of ∼1.4-3.0 eV practically satisfies these two opposing constraints.[6] Both the density and average Z of the material relate to the stopping distances of ionizing radiation in the device. Materials with higher Z and higher density allow for smaller detectors.

An additional important requirement of a good detector is that its output should not depend on where the ionizing radiation strikes the device. For a semiconductor, this means that the electron-hole pairs created during ionizing events must be able to be swept to the contacts completely, regardless of where in the device they are created. The consistency of response, and hence the energy resolution of a semiconductor device is determined largely by the uniformity of its charge collection.[7] This is illustrated in figure 1.5.

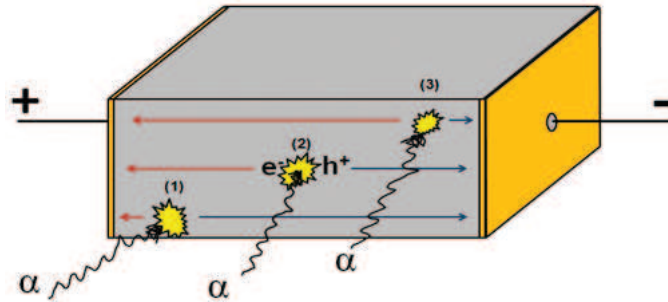

Figure 1.5: A diagram depicting a semiconductor radiation detector being struck by alpha particles at three different locations, marked with numbers. The red and blue lines show the direction and lengths that the generated electrons and holes travel respectively. For strike **(1)**, the electrons travel a short distance to the contact, whereas holes must traverse nearly the whole length of the device. For strike **(3)**, the situation is reversed. For strike **(2)**, in the middle of the device, the electrons and holes must drift an equal distance to be collected.

The important figure of merit for assessing uniform charge collection in a detector is the mobility-lifetime product, $\mu\tau$. By knowing the $\mu\tau$ products of free carriers in a material, one can estimate how large a device can be made without compromising charge collection. A simple dimensional analysis (equation 1.1) shows the importance of $\mu\tau$.

$$[\mu\tau] = \frac{[cm^2]}{[V \cdot s]} \cdot [s] = \frac{[cm^2]}{[V]} \tag{1.1}$$

Multiplying the mobility-lifetime product by an applied electric field, with units of V/cm, yields a drift length. This is the average distance a carrier travels in the material under the applied electric field before recombining. Ideally, this distance should be equal to or longer than the longest dimension of the detector itself, in order to ensure complete charge collection. A typical operating bias for a detector is 1000 V/cm. Thus, the value of $\mu\tau$ required for complete charge collection in a cubic detector with a volume of 1 cm^3 is found as follows:

$$\mu\tau[\frac{cm^2}{V}] \cdot \frac{1000V}{cm} = 1cm \Rightarrow \mu\tau = 10^{-3}\frac{cm^2}{V} \tag{1.2}$$

The matter of charge collection is slightly complicated by the fact that the drift lengths of electrons and holes in materials are different. The discussion of this complication is beyond the scope of this work, but the results of several clever detector designs and electronic schemes have created devices that count charge collection of a single carrier only. Thus, the carrier with the highest $\mu\tau$ determines the energy resolution of the device, as long as the $\mu\tau$ product of the other carrier satisfies a few more requirements enumerated elsewhere.[7] By modern standards, a material must achieve a single carrier mobility-lifetime product of at least 10^{-3} cm^2/V to be considered a good candidate for radiation detection.

1.2.5 The "Right" Kind of Resistivity

The charge collection constraints discussed in the previous section highlight an important consideration in materials selection for resistive detectors. The materials must be highly resistive in the *right* way. This can be seen by examining the formula for the conductivity of a semiconductor:

$$\sigma = ne\mu_e + pe\mu_h \tag{1.3}$$

Here, n and p are the concentrations of free electrons and holes, μ_e and μ_h are the mobilities of electrons and holes, and e is the charge of an electron. The overall conductivity of a semiconductor will be low if n and p are low, μ_e and μ_h are low, or both. However, for good charge collection, μ_e and μ_h must be as high as possible. Therefore, resistive detectors require materials with very low concentrations of free electrons and holes (ie: low n and p), but high electron and hole mobilities.

1.3 Thallium Bromide (TlBr): A Promising Material for Resistive Detectors

Thallium Bromide (TlBr) has emerged as a promising candidate for room temperature resistive semiconductor detectors. TlBr satisfies all of the materials and device requirements introduced in Section 1.2.4. The subject of this dissertation is the experimental characterization of deep levels in TlBr, with the goal of improving the electrical properties of the

material. Therefore, the next several sections will introduce TlBr and give a brief summary of its development. TlBr is first compared to the market leading room temperature detector material - $Cd_{1-x}Zn_xTe$ - to give an idea of the properties and performance with which TlBr must compete. Then, an overview of the growth, processing, and performance of TlBr detectors is presented.

1.3.1 TlBr compared to Cadmium Zinc Telluride ($Cd_{1-x}Zn_xTe$)

Table 1.1: $Cd_{1-x}Zn_xTe$ & TlBr - Relevant Materials Properties [8, 9, 10, 11]

Material	Atomic Number	Density $[\frac{g}{cm^3}]$	Band Gap [eV]	μ_e $[\frac{cm^2}{V\cdot s}]$	τ_e $[s]$	μ_h $[\frac{cm^2}{V\cdot s}]$	τ_h [s]
CZT	48,40,52	6.2	1.57	800-1300	$(1-5) \times 10^{-6}$	~30-80	$\sim 10^{-6}$
TlBr	81,35	7.56	2.68	~50	$\sim 10^{-5}$	~5	$\sim 10^{-5}$

The current leading material for room temperature radiation detection is Cadmium Zinc Telluride ($Cd_{1-x}Zn_xTe$ or CZT). Commercial CZT detectors with energy resolution sufficient for security applications are commercially available from companies such as Redlen[1] and EI Detection and Imaging Systems (formerly eV Products)[2]. Typical $Cd_{1-x}Zn_xTe$ detectors have an x value of 0.1, which leads to a material with a bandgap of 1.57 eV, sufficient to ensure negligible thermally generated leakage current at room temperature. Cd (48) and Te (52) have significantly higher Z values than Ge (32), and the density of CZT is 6.2 g/cm^3 compared to 5.32 g/cm^3 for germanium.[12]. CZT detectors can be smaller than Ge detectors for the same stopping power. A summary of important materials properties of CZT is given in Table 1.1.

With a $\mu_e \tau_e$ product of 10^{-3} cm^2/V and state of the art device packaging and readout electronics, the best CZT detectors have energy resolutions just below 1% for a 662 keV gamma ray at room temperature. For comparison, high purity germanium detectors have a resolution of 0.2% at the same energy.[4, 13] Thus, any material that would replace CZT must achieve at least the sub-1% energy resolution benchmark.

CZT is at a mature stage of development after over 40 years of productive materials research. The electronic properties of the best CZT grown today are in many ways optimal and unlikely to improve. The state of CZT research and development is beyond the scope of this work and can be found in several review articles.[12, 9, 14] The biggest problem facing CZT is the difficulty of growing large crystals with spatially uniform charge transport properties. The uniformity problem leads to low yield of detector grade material, which increases the cost of producing CZT. Currently, top quality CZT is too expensive for widespread use in security applications.

[1]www.redlen.ca
[2]www.evmicroelectronics.com

Thallium Bromide presents a serious alternative to CZT, though development of the material is still far behind that of CZT. The high-Z of Tl (81) combined with the high density of the material of 7.56 g/cm^3 [15] ensure excellent stopping power of ionizing radiation, and the relatively large 2.68 eV bandgap leads to very low thermally generated leakage current at room temperature operation. Table 1.1 compares important materials properties of TlBr and CZT. Figure 1.6 shows the stopping power of TlBr compared to CZT and Si.

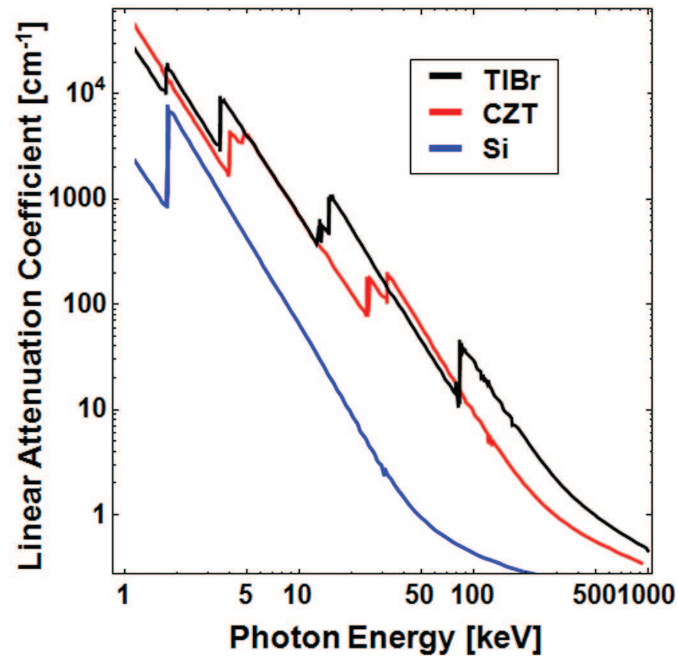

Figure 1.6: The linear attenuation coefficient of TlBr compared to those of CZT and Si. Replotted with data taken from Reference [16].

1.3.2 Growth of TlBr

As opposed to many "new" materials being developed in thin film form for a myriad of electronic applications, TlBr is relatively easy to grow in bulk. This is extremely important for a detector material, as detectors must be bulk-sized to stop gamma rays. TlBr has a simple cubic CsCl structure at room temperature and melts congruently, making it simpler to grow than CZT.[16] Bulk crystals of TlBr have been grown as early as 1933, and used as detectors as early as 1947, following the successful report of an AgCl radiation detector in 1945.[17, 18]

A common technique for growing bulk TlBr is the Bridgman-Stockbarger method.[19, 17]] In this method, starting material of either highly pure TlBr salts or polycrystalline TlBr is sealed in an ampoule. Before crystal growth, the ampoule is usually zone refined up to

several hundred times to further purify the starting material. The ampoule is typically made of Pyrex or fused quartz, and can be treated to reduce surface adhesion of the TlBr crystal during growth. After refining, the whole ampoule is heated above the melting temperature of TlBr (480° C). Once the material is fully melted, a directional temperature gradient is induced by slowly removing the ampoule from the heater, either by lowering or raising it out of the heater, often into another heater held at a lower temperature to control the temperature gradient across the material. The crystal solidifies directionally as the material cools. [20, 17, 21, 22, 23]

Another common method to grow TlBr is the traveling molten zone (TMZ) method. The starting material of zone purified TlBr in an ampoule is the same for both TMZ and Bridgman growth. In the TMZ method however, the crystal is grown in essentially the same way as the zone refining is performed. The main difference between TMZ growth and zone refining is that the rate at which the molten zone is moved across the material (either by moving the heater or by moving the ampoule through the heater) is much slower, by at least a factor of ten. TMZ growth can be done with the same equipment as zone refining, which reduces handling and possibly contaminating the material.[24, 15, 20] In recent years, crystals grown by the TMZ method tend to have superior electronic properties to those grown by the Bridgman process. Most of the TlBr samples studied in this dissertation were grown by the TMZ method, with the exception of the Se-doped and Pb-doped samples.

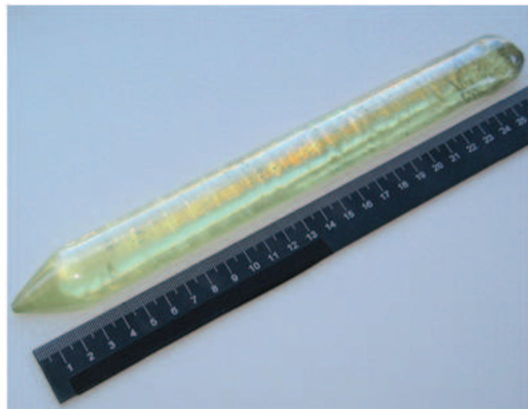

Figure 1.7: A TlBr crystal grown by the Traveling Molten Zone Method. The left side is the pure seed end, and the right side shows clearly a higher concentration of dark impurities. (From Reference [24].)

Typical sizes of crystals grown by the TMZ and Bridgman methods range from 2 mm to over 1 cm in diameter. For reference, the mean free path of 511 keV photon in TlBr is 1 cm, which makes a detector of 1 cm^3 or more in size desirable. [16] These two methods of growth are responsible for producing the best detector-grade TlBr crystals reported in the last decade. However, other methods have been used and proposed. One of the more interesting variations is the Electro-Dynamic Gradient (EDG) method, in which a temperature gradient

similar to the Bridgman method is induced along the melt, but the difference is that the gradient is produced by electrical variation of the heating zone, as opposed to mechanical movement of the material, potentially leading to higher crystal quality with less mechanical damage.[25] TlBr thin films have been grown as well. The simplest reported method involves growth by thermal evaporation on aluminum and silicon plates.[26]

It is important to note that the growth of single crystal TlBr is easier than it is for CZT. CZT growth is plagued by tellurium inclusions that act as charge trapping centers and have a detrimental effect on device performance.[27] Such microstructural defects reduce the yield of usable detectors cut from large CZT crystals, and thus much research has been invested in 3D characterization of CZT crystals before cutting in order to optimize device yield.[28, 29] In this respect, the relative ease of growing large TlBr single crystals is potentially a substantive commercial advantage of the material. However, the performance of detectors made from TlBr are still limited by the purity and structural quality of the crystals being grown.[30, 17] Thus, increasing material purity remains one of the most important challenges for improving the electronic properties of TlBr.

1.3.3 Electrical Transport Properties

TlBr is one of only a few wide band gap resistive materials to achieve a $\mu_e\tau_e$ of $10^{-3}cm^2/V$ for electrons, and values of both $\mu_e\tau_e$ and $\mu_h\tau_h$ are now on par with those of CZT. Typical values of $\mu_e\tau_e$ and $\mu_h\tau_h$ in commercial grade CZT are around $8-9\times10^{-3}$ and 10^{-5} cm$^2/V$ respectively.[31] These numbers have not improved significantly in the last 20 years of growth. In contrast, TlBr has witnessed a dramatic increase in transport properties as a result of focused research. In 1989, a typical reported value for $\mu_e\tau_e$ and $\mu_h\tau_h$ was 3×10^{-6} and $2\times10^{-6}cm^2/V$.[16] By 2002, several groups had reported material with $\mu_e\tau_e$ on the order of $10^{-4}cm^2/V$.[11, 22, 32] Recent efforts have pushed this even further, with the best values for $\mu_e\tau_e$ now being reported in the mid 10^{-3} cm^2/V range. [33, 34, 15] Thus, 1 cm^3 and larger devices have now been achieved in TlBr, making it the only other compound semiconductor with a bandgap larger than 1.5 eV to have comparable transport properties to CZT. The first TlBr detectors with energy resolution at or below 1% for a 662 keV gamma ray have been reported.[35] This two orders-of-magnitude improvement in transport over the last 25 years is due mainly to progress in the purification of TlBr, as well as crystal quality enhancement through growth and handling refinement.

1.3.4 Outstanding Challenges

TlBr radiation detectors pose a few challenges that are unique to the material and not relevant to CZT. The most important challenge is that TlBr is a strongly ionic material with a large dielectric constant. As a consequence, the material has relatively low defect formation energies and thus large equilibrium concentrations of vacancies. TlBr has been proven to conduct ionically at room temperature, and it has been suggested that the vacancies are primarily responsible for mediating the ionic conductivity.[36, 37, 38, 39, 40, 41] Ionic con-

ductivity is undesirable in a radiation detector, as it contributes to the leakage current of the device. As a TlBr device is operated under bias, moving ions also contribute to the build up of an internal electric field that opposes the applied bias. This issue is presented in more detail in Chapter 6. The reduction or mitigation of ionic conductivity at room temperature is an area of active research.

TlBr is a soft material that is easily mechanically damaged. Mechanical damage can lead to the creation of charge trapping extended defects that reduce the performance of TlBr detectors. Thus, greater care must be taken when working with TlBr compared to CZT devices. However, proper handling and device packaging can minimize the risks of device degradation.

1.4 Conclusion: Opportunities for Materials Engineering

The remarkable improvement of the electrical properties of TlBr over the last 25 years gives hope that material may yet be improved even further. Improving a resistive semiconductor requires knowledge of deep levels present in the material and the effects of these deep levels on transport properties. Very few deep level studies have been conducted on TlBr, and none with the depth required to generate useful growth suggestions. In contrast, CZT has greatly benefited from three decades of research into the deep levels that control resistivity in the material. This dissertation reports progress in several types of experimental deep level studies performed on state-of-the-art detector grade TlBr, with the goal of further improving the material.

Chapter 2

Photo-Induced Conductivity Transient Spectroscopy (PICTS)

The purpose of this chapter is to introduce Photo-Induced Conductivity Transient Spectroscopy (PICTS) - a powerful technique well-suited for studying deep levels in the highly resistive materials being considered for room temperature radiation detection. Before introducing PICTS, a brief overview of the experimental study of deep levels in semiconductors will be given, covering earlier techniques that are relevant to the development of PICTS. The construction of the PICTS system used in this dissertation is described. Finally, results of measurements taken with the system on semi-insulating gallium arsenide (SI GaAs) are presented and compared to values reported in literature.

2.1 Experimental Detection of Deep Levels

The principle properties of interest in experimental deep level studies are:

1. Number of distinct traps in the material
2. Trap type: majority or minority carrier
3. Trap concentration [cm^{-3}]
4. Thermal activation energy of the trap, measured from the conduction or valence band edge [eV]
5. Capture cross-section [cm^2]
6. The chemical or structural origin of the deep level

With the exception of the last item, these properties can be determined by observing the role of deep levels in two important kinetic processes: the capture of free carriers and

emission of trapped carriers. These two processes change measurable electronic properties of a material, such as the conductivity of a resistive sample or the capacitance of a depletion layer. The goal of a deep level experimental method is thus to identify and measure a signal that corresponds to either carrier capture or emission, and then to calculate the quantities of interest from the known functional dependencies of the identified signal.

2.1.1 Capture and Emission Kinetics

The capture rate of an electron trap[1] is given by:

$$c_n = \sigma < v_n > n \tag{2.1}$$

Here, σ is the capture cross section of the trap, v_n is the average thermal velocity of an electron in the material, and n is the concentration of free electrons in the material. It is important to note that the concentration in this equation is time dependent, ie: $n = n(t)$. As an electron trap captures electrons, the concentration of free electrons decreases.

The emission rate of an electron trap is given by:

$$e_n(T) = \gamma T^2 \sigma_{na} e^{-\frac{E_{na}}{k_B T}} \tag{2.2}$$

Here, the prefactor γ is given by $\gamma = 2\sqrt{3} M_c (2\pi)^{\frac{3}{2}} {k_B}^2 m^* h^{-3}$, where M_c is the number of conduction band minima, and σ_{na} is the "apparent" capture cross section. E_{na} is the thermal activation energy of the deep level, which is equal to $(E_c - E_T) + \Delta E_\sigma$, where ΔE_σ is related to changes in the lattice vibrational and electronic entropies associated with the deep center changing its charge state. A detailed derivation of these equations, along with an enumeration of assumptions, is found in chapters 7 and 8 of P. Blood and J.W. Orton[42].

Equation 2.2 is of enormous importance to experimental deep level studies. The equation contains two of the principle quantities of interest of a deep level: the thermal activation energy, and the capture cross section. It is common to rearrange equation 2.2 as follows when plotting measured emission rates as a function of temperature:

$$\begin{aligned} e_n(T) &= \gamma T^2 \sigma_{na} e^{-\frac{E_{na}}{k_B T}} \\ \frac{e_n(T)}{T^2} &= \gamma \sigma_{na} e^{-\frac{E_{na}}{k_B T}} \\ ln(\frac{e_n(T)}{T^2}) &= -\frac{E_{na}}{k_B T} + ln(\gamma \sigma_{na}) \end{aligned} \tag{2.3}$$

It can be seen that by plotting the log of the emission rate divided by T^2 versus 1/T, the result is a straight line, where the slope of the line is $-E_{na}/k_B$, and the y-intercept is $ln(\gamma\sigma_{na})$.

Because of the richness of information contained in such plot, the general strategy of deep level experimental techniques is to measure a signal related to the emission of carriers

[1] An exactly analogous expression can be derived for a hole trap: $c_p = \sigma < v_p > p$. Electron traps only are presented here for simplicity of notation, but an identical analysis for hole traps applies.

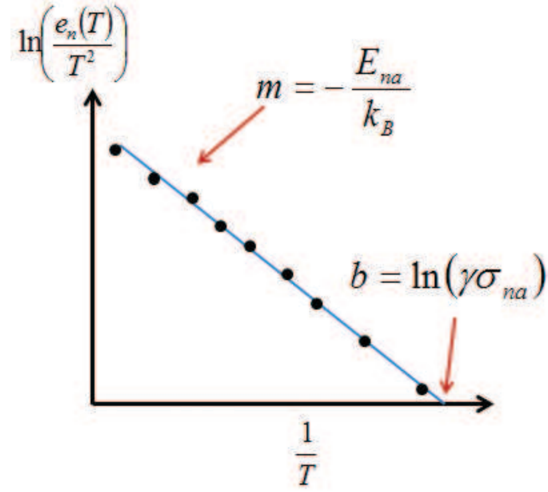

Figure 2.1: A schematic arrhenius plot of the carrier emission rate of a deep level as a function of temperature, showing the relations between the trap quantities of interest and plot features.

in order to extract emission rates as a function of temperature. Carrier capture rates are typically harder to measure experimentally and do not yield as much useful information about the trap. Once the emission rate of a trap has been recorded at several different temperatures and plotted, the thermal activation energy and capture cross section can be quickly be determined by making an Arrhenius plot. The linearity of the plot is a good and fast quality check of the data as well. If the plotted emission rates diverge strongly from linearity, the experimentalist knows that either the physical process being measured is not isolated emission from a single trap, or the measurement results have large errors. Strong linearity over a wide dynamic range on the other hand suggests good agreement with the underlying physical assumptions.

2.1.2 Thermally Stimulated Conductivity (TSC) and Deep Level Transient Spectroscopy (DLTS)

One early and very simple method of studying deep states in resistive semiconductors is thermally stimulated conductivity (TSC), first proposed by Urbach in 1930 and later extensively analyzed.[43, 44] A simple TSC experiment on a highly-resistive material with ohmic contacts is performed as follows. First, the sample is cooled in the dark to a low temperature, typically 77K. The sample is then illuminated with light of suitable energy for a sufficient time to fill traps in the material - typically many minutes to an hour. A bias is placed across the sample, and the current flowing through the material is recorded as a function of time with a sensitive ammeter. Next, the sample is heated up at a known rate. As the material warms up, deep levels within the bandgap thermally release free carriers

that were trapped during the optical excitation stage. The release of free carriers triggered at temperatures related to the depth of the trap responsible causes a transient increase in conductivity, which is recorded as current by the ammeter. Once all of the finite number of trapped carriers at a given trap are released, the conductivity restores to a baseline value, leading to a conductivity spectrum as a function of temperature characterized by peaks indicating the presence of traps. With suitable analysis and by using different heating rates, trap energies and concentrations can be calculated.

The experimental simplicity of TSC and the richness of information given make it an important measurement. However, the technique suffers from several disadvantages as well. First, the technique is only suitable for materials with an extremely low background conductivity, so that the thermal release of carriers from traps can be detected against the background. Additionally, the measurement is a "one-shot" technique, and as such, is relatively slow. The sample must first be measured across the whole temperature range of interest without any optical pumping of traps, to establish the conductivity baseline as a function of temperature. The experiment must then be performed several times more with different heating rates in order to calculate quantitative trap parameters. Each thermal scan over a broad temperature range can take several hours to a day, leading to a several-day time period required to measure one sample, and completely ruling out the possibility of practical signal averaging for a given heating rate.

In 1974, D. V. Lang at Bell Labs proposed a powerful technique that overcomes many of the shortcomings of TSC to experimentally characterize deep levels in semiconductors - Deep Level Transient Spectroscopy, or DLTS.[45] In a DLTS experiment, the capacitance of a depletion region of a p-n junction or Schottky barrier is recorded as a function of time. The depletion region width, and hence the capacitance, is initially held constant by a steady state bias. The depletion region width is then modulated by a change in the applied bias. A momentary decrease in reverse bias allows majority carriers to enter the formerly depleted region, filling majority carrier traps. A momentary pulse of forward bias injects minority carriers as well and fills minority carrier traps. When the initial constant bias is restored, the return of the capacitance to the steady state value is characterized by a transient related to the emission of majority and minority carriers from deep levels in the material. In the simplest case, considering a single trap level at a fixed temperature and neglecting carrier retrapping, the transient can be shown to have the form of a single exponential with a time constant related to emission from the trap.[46]

$$\frac{\Delta C(t)}{C(\infty)} = -\frac{N_T}{2N_D} exp(-e_n t) \tag{2.4}$$

In DLTS, the sign of the transient indicates the trap type - majority or minority carrier.[45, 47] The spectroscopic aspect of DLTS comes from the fact that the capacitance transients are recorded over a wide temperature range. As shown in equation 2.2, the emission rates of traps are strongly temperature dependent. In general, at very low temperature, the emission rate of a trap is negligible, and at very high temperatures, the emission rate is very fast. Between these extremes, there is a range of temperatures over which the emission rate of a

given trap falls within the time scale of the instruments being used to record the transient with high sensitivity. For traps with different thermal activation energies, this specific range of temperature will be different. Therefore, by sweeping across a wide temperature range, emission from traps with different thermal activation energies can be resolved individually.

DLTS experiments provide a wealth of information about deep levels in a semiconductor material. The analysis gives information on the number of distinct traps in the material and their concentrations, energy levels, capture cross sections, and trap types. This information is enormously important for many semiconductor devices, where precise control of properties such as the minority carrier lifetime can be achieved by engineering the deep level concentrations. DLTS measurements also facilitate averaging, leading to higher sensitivity and signal-to-noise ratios than in TSC measurements. Typical emission rates measured with DLTS equipment span the time range from tenths of microseconds to tens of milliseconds. One can therefore configure a system to measure and average many capacitance transients per second at a given temperature. DLTS systems can be built in such a way so that only a single temperature scan is necessary, making it a faster measurement than TSC as well.

For the right kind of materials, DLTS was a major breakthrough for rapid and sensitive characterization of deep levels. However, DLTS experiments require a high quality p-n junction or Schottky barrier with very low leakage currents. They cannot be performed on poor quality diodes with prohibitively large leakage currents, or on high resistivity materials where the series resistance of undepleted material distorts the measurement. Additionally, the capacitance transients observed in materials with large trap concentrations are not exponential, complicating analysis.[42] Thus, other techniques are needed to characterize deep levels in the highly resistive semiconductor materials being considered for room temperature radiation detection.

2.2 Photo-Induced Conductivity Transient Spectroscopy (PICTS)

2.2.1 Experimental Overview

Photo-Induced Conductivity Transient Spectroscopy (PICTS) was introduced in 1978 as a way to characterize deep levels in highly resistive materials, combining the strengths of TSC for resistive materials with the power of the signal averaging and repetitive rate window analysis of DLTS. [48] Trap information is obtained by recording conductivity transients, as opposed to capacitance transients. In a PICTS measurement, a resistive material with ohmic contacts is placed under bias in a dark cryostat. Over a wide temperature range, the sample is periodically illuminated with a pulse of light. The current flowing through the sample is monitored with a fast current amplifier.

In order to interpret the information contained in such a measurement, it is useful to separate the expected current behavior into two stages: when the light is turned on, and when it is turned off. At the onset of illumination, free carriers are photo-generated in

significant concentration, increasing the conductivity of the sample and leading to a rapid increase in current. The increase is slowed by the trapping of free carriers at deep levels, giving the initial rise of the photocurrent a curvature that is related to the capture rates of the levels. A steady state is reached when the traps saturate and the rate of photogeneration of carriers equals the rate of recombination. When the light is turned off, the measured current can be broken into two components. The first component is a very fast decline due to carrier recombination, including band-to-band, Shockley-Read-Hall, and Auger processes. In a direct band-gap semiconductor, this component of the signal is typically on the order of a few nanoseconds. The second component is a slower transient related to the emission of free carriers from deep levels that were captured during the illumination phase. These emission rates are strong functions of temperature, and experimental methods typically measure transients in the range of microseconds to milliseconds. A schematic of the expected PICTS signal is illustrated in figure 2.1.

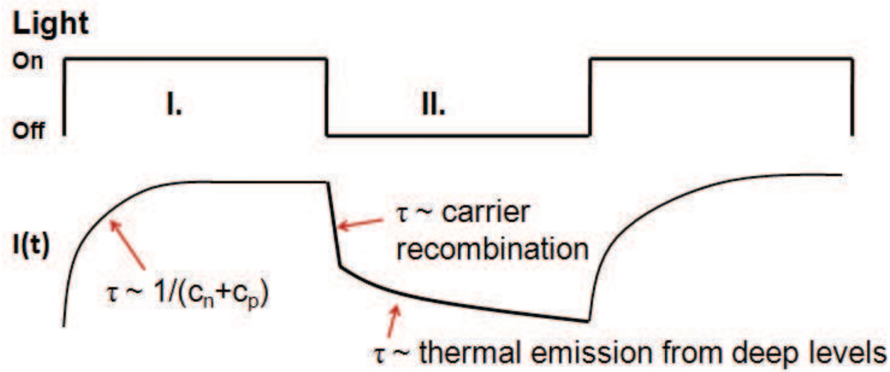

Figure 2.2: A schematic of the signal observed in a PICTS measurement.

It can be shown that for a sample with ohmic contacts and a single deep level electron trap (and with a few other simplifying assumptions[2]) that the expected current transient related to thermal emission will have the form[49]:

$$\Delta J_c(t) = -e\varepsilon\mu_e\tau_e e_n n_t(0)exp(-e_n t) \tag{2.5}$$

Here, e is the electron charge, ε is the electric field applied across the sample, and μ_e and τ_e are the mobility and lifetime of electrons. The concentration of filled traps when the light is turned off, $n_t(0)$, can be assumed to be equal to the total concentration of traps if the light pulse is of sufficient intensity and duration to fill all traps. The carrier mobilities and lifetimes in Equation 2.5 depend on the temperature. These quantities can be consolidated along with the trap concentration and electric field information into a temperature-dependent prefactor to rewrite the equation in a simpler form:

[2] A detailed discussion can be found in P. Blood and J.W. Orton, chapter 7.8

$$\Delta J_c(t) = B(T)e_n exp(-e_n t) \tag{2.6}$$

From this equation, it can be seen that by measuring the slower current transient of a sample once the light is turned off, and fitting it to a single exponential, one can directly measure the emission rate e_n of a trap. By repeating this process over a wide temperature range, Arrhenius plots can be made and trap parameters determined.

2.2.2 PICTS Data Analysis: Two-Gate and Four-Gate Technique

While the theoretical trap signal shown in Equation 2.6 is expected to be a single exponential, PICTS raw data is not usually analyzed by fitting transients with an exponential function in order to extract the time constant, for several reasons. One reason is that the trap signal is convoluted with a temperature dependent recombination signal, as shown in Figure 2.2, which makes it unclear where to start an exponential fit. Another practical reason relates to the early equipment used in PICTS measurements and the storage capacity of computers. As with DLTS measurements, early PICTS systems were not able to record complete transients. A transient consisting of many thousands of data points requires many kilobytes to store, and complete data sets of transients across several hundred degree temperature ranges can take up hundreds of megabytes of storage. Because of the relatively large size of such a data set, early PICTS systems reported in literature did not record whole transients. Instead, they stored only the time constant associated with the transient, which was calculated with analog electronics using a single or double boxcar integrator.[48, 50, 51] These methods have been found to be as accurate at determining time constants as direct fitting with single exponential functions, and more accurate than single-exponential fitting when the underlying signal is composed of multiple exponential processes.

A single boxcar integrator is an analog implementation of two-gate analysis technique for PICTS data. A two-gate PICTS signal is composed as follows: from a current transient at a constant temperature, two points are selected in time, t_1 and t_2. These two points determine the "rate window" of the measurement, which is defined as $t_1 - t_2$. The two-gate "signal" is defined as the current at t_1 minus the current at t_2, ie:

$$S_{two-gate}(T) = I(T, t_1) - I(T, t_2) = B(T)e_n(T)(exp(-e_n(T)t_1) - exp(-e_n(T)t_2)) \tag{2.7}$$

Plotting $S_{two-gate}$(T) versus temperature for a chosen rate window results in a spectrum with peaks. By differentiating Equation 2.7 with respect to the emission rate e_n, it can be shown that under certain conditions the maximum of a peak in a two-gate spectrum corresponds to a point in temperature at which the chosen rate window equals the time constant of the exponential emission rate of the trap. Thus, by recording peak positions in temperature for different rate windows, the emission rates of traps in the material can be determined as a function of temperature. This information is then fit to Equation 2.2 to extract trap parameters.

The temperature dependent prefactor in Equation 2.7 complicates two-gate analysis however. If the temperature dependence of carrier mobilities and lifetimes in a material is strong, the contribution from the prefactor can negatively affect the clarity of the two-gate spectrum, leading to distorted peaks on top of a strongly varying baseline. To address this issue, four-gate PICTS analysis was developed.[49] Figure 2.3 shows a schematic of the four-gate analysis approach. In four-gate analysis, four points in time are chosen: t_0, t_1, t_2, t_3. As with two-gate analysis, two of the gates define the rate window of the experiment: t_2 - t_1. The other two gates are used to define a normalization window: t_3 - t_0. The four-gate signal is then given by:

$$S_{four-gate}(T) = \frac{I(T,t_1) - I(T,t_2)}{I(T,t_0) - I(T,t_3)} = \frac{exp(-e_n(T)t_1) - exp(-e_n(T)t_2)}{exp(-e_n(T)t_0) - exp(-e_n(T)t_3)} \tag{2.8}$$

Equation 2.8 shows that by normalizing the PICTS signal, the temperature dependent prefactor present in Equation 2.6 is eliminated from the four-gate spectrum entirely. Once again, plotting $S_{four-gate}(T)$ leads to a spectrum with peaks. By taking the derivative of Equation 2.8 with respect to e_n, peak maxima are found to occur when:

$$e_{n,max} = \frac{1}{t_2 - t_1} ln(\frac{t_2 - t_0}{t_1 - t_0}) \tag{2.9}$$

The rest of four-gate analysis is identical to two-gate analysis. Different rate windows are chosen to vary the position of peaks versus temperature, and Equation 2.9 is used to calculate the emission rate of traps from the peak positions.

Four-gate PICTS analysis has been shown to give the best spectral resolution and accuracy for analyzing traps in PICTS. [49, 42] One consequence of the normalization however is that information pertaining to the trap concentration is also lost in the process. Thus, trap concentrations cannot be determined using four-gate PICTS analysis.

2.3 Building a Modern PICTS Measurement System

A PICTS system was built to perform the PICTS measurements reported in this dissertation. The construction of the system is the subject of this section. The hardware used is described, as well as the control and analysis software that was developed.

2.3.1 Instrumentation

In order to provide a dark environment capable of facilitating a wide temperature range, an IR-Lab dewar capable of being cooled with either liquid helium or nitrogen was chosen. In PICTS experiments, lower temperatures correspond to the detection of shallower energy traps. For practical experimental purposes, liquid nitrogen temperatures are usually sufficient to detect the shallowest deep levels. The dewar was connected to a turbo-molecular and

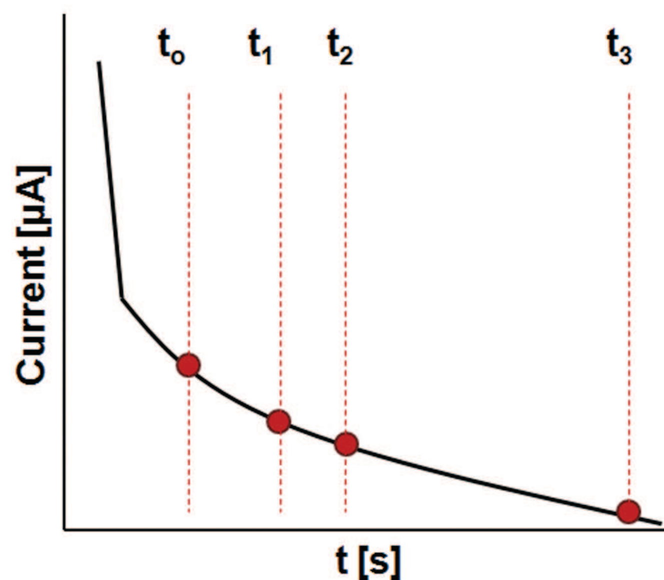

Figure 2.3: An idealized PICTS signal showing the principle of 4-gate PICTS signal analysis.

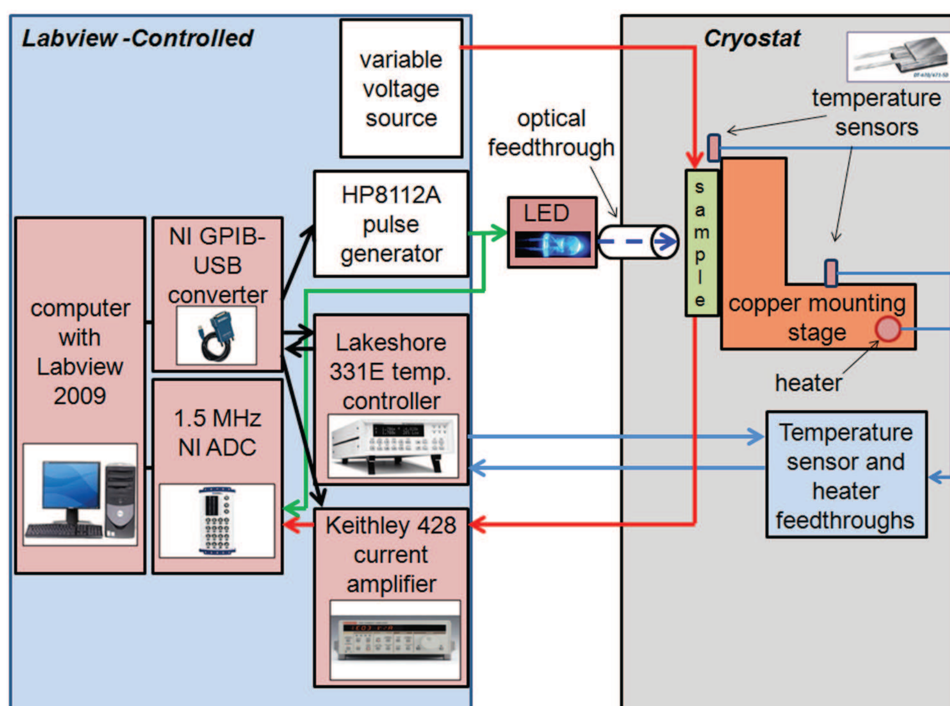

Figure 2.4: A schematic of the PICTS system constructed, showing the instruments used and signal paths.

roughing pump vacuum system capable of achieving an operating vacuum level of $\sim 1 \times 10^{-6}$ torr.

A copper platform in the shape of an "L" was machined to serve as the sample stage inside the dewar. Samples were mounted vertically to the sample stage and affixed and thermally coupled with copper tape and Apiezon N cryogenic vacuum grease. Two Lakeshore Cryotronics DT-670 temperature sensors were used to measure the temperature inside the cryostat. To read the temperature of the sample under measurement, one of the sensors was mounted on the copper stage as closely to the sample as possible, typically within a millimeter. This sensor was removable, and was remounted with each new sample. To control the temperature of the mounting stage, the other sensor was permanently attached to the base of the copper platform. This sensor was further away from the sample, but the permanent attachment was important to avoid the sensor losing contact with the copper platform and thus breaking the temperature control circuit. The two sensors usually agreed to within 1 K. Figure 2.5 shows the copper stage with a TlBr sample mounted to it.

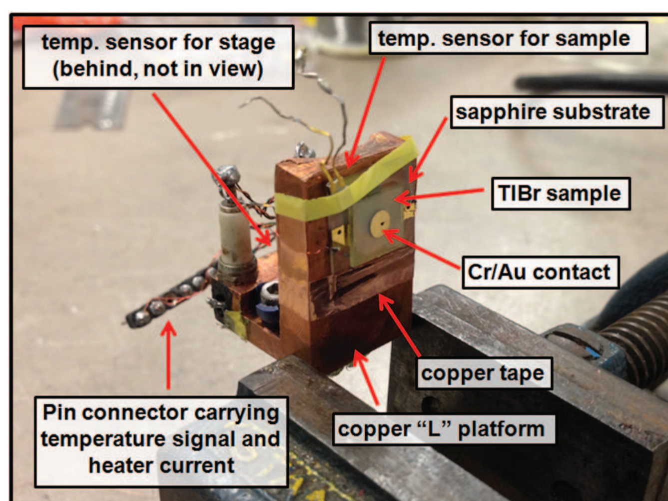

Figure 2.5: The PICTS mounting stage with a TlBr sample.

The sample stage was heated by a 50-ohm resistor potted into the platform with Stycast epoxy. The output from the two diode temperature sensors and the leads of the heater circuit were connected to a Lakeshore Cryotronics Model 330 auto-tuning temperature controller. With the heater power on the "medium" setting of the controller (corresponding to a maximum power of 5 Watts), the controller was able to stabilize the temperature over the range 80-350 K.

Light pulses were directed onto the sample via an optical vacuum feedthrough. A quartz rod was inserted through a feedthrough and vacuum-sealed by an O-ring to act as a wave guide. One end of the rod faced the sample inside the cryostat. The other end of the rod outside of the cryostat was connected to an interchangeable set of high-brightness light emitting diodes (LEDs), and shielded from external light by an enclosing aluminum sheath

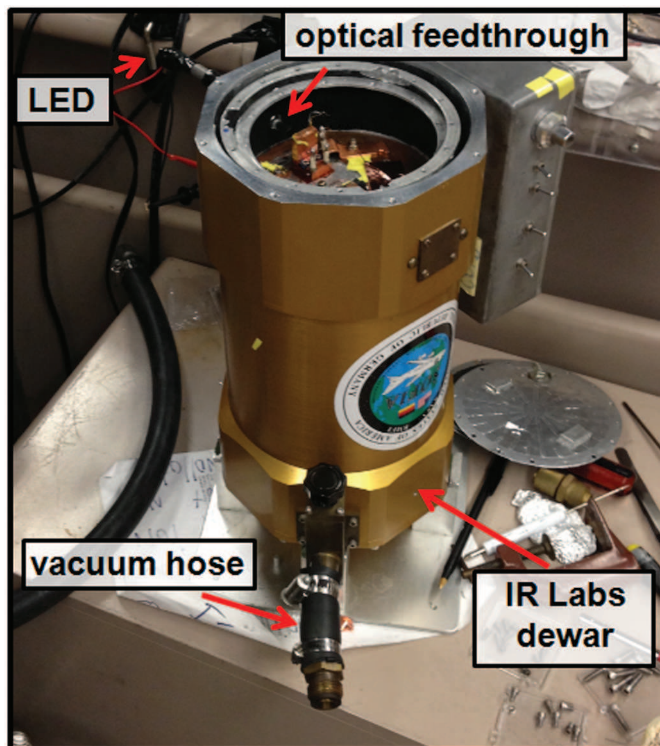

Figure 2.6: The IR Labs cryostat outfitted for PICTS, with the top off.

and black electrical tape. The wavelength of the LED was chosen based on the sample being measured. For TlBr with a bandgap of 2.68 eV, a CREE high brightness LED peaked at 450 nm (2.76 eV) was used as the illumination source. For semi-insulating gallium arsenide (SI GaAs) samples with a bandgap of 1.42 eV, an LED peaked at 660 nm (1.88 eV) was used. The diodes were turned on and off by an HP 8112A pulse generator. The pulse generator also served as the timing device for the measurement, as described in section 2.3.2.

The sample was biased with an MPJA 50-Volt variable power supply. The time-resolved current flowing through the sample was measured with a Keithley 428 fast current amplifier. The output of the Keithley was connected to an oscilloscope for signal monitoring, and to a National Instruments USB-6210 analog-to-digital converter (ADC) with a 1.5 MHz sampling rate. The NI ADC was connected to a computer, where the digitized current transients were saved during a measurement.

2.3.2 Control Software

The PICTS experimental control software was written in NI LabView 2009. To operate the PICTS program, a temperature range for the measurement is selected - typically 80-300 K, progressing in increments specified by the user (usually 0.5 K). The sample is mounted in the cryostat, which is connected to the vacuum pumps and cooled with liquid nitrogen to

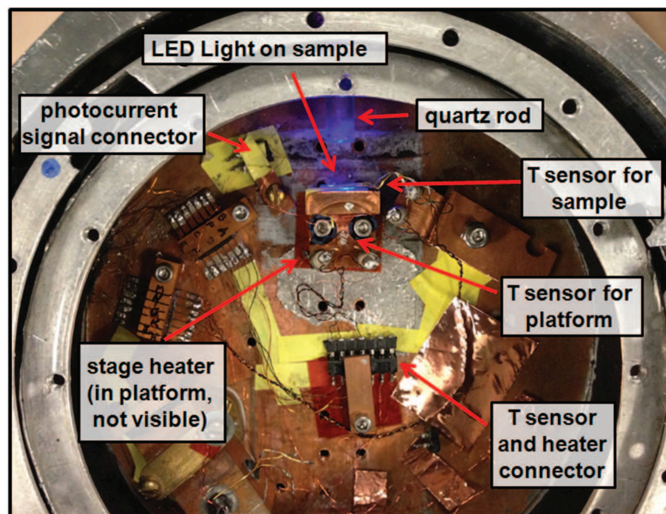

Figure 2.7: Top-view of the inside of the PICTS dewar, showing the stage with a TlBr sample mounted to it, connected to the dewar feed-through wiring. The LED (peaked at 450 nm, 2.76 eV) is on, and the blue light coming through the quartz rod and reaching the sample is visible.

the starting temperature. The program waits until the starting temperature stabilizes before beginning to record data. The user specifies what is considered a "stable" temperature by choosing a range that the temperature must read between (usually +/- 0.1 K from the temperature set point), and the time period over which the temperature must read within this range (usually 1 to 2 minutes).

Once the starting temperature has stabilized, the program is ready to record data. The program monitors the output of the pulse generator, which is connected both to the LED and to the USB-6210. When the pulse falls, the light turns off, and the program is triggered to record data with a sampling rate and time period specified by the user. Using the pulse generator both to power the LED and to trigger the data acquisition minimizes the potential for jitter in the averaged recorded data. For TlBr measurements, the pulse generator was typically configured to turn on for 350 ms, and off for 150 ms. The photoconductivity transient decay was thus recorded for 150 ms, at a sampling rate of 1 MHz. In order to improve the signal-to-noise ratio, the program averages many signals at a fixed temperature. The number of averages is specified by the user, with 100-300 averages being a range of typical values. A total cycle time of 500 ms (350 ms on, 150 ms off) allows two photoconductivity transients to be recorded per second.

When the program has finished recording and averaging transients at the starting temperature, the temperature set point is increased by an increment specified by the user (usually 0.5 K). The temperature controller heats the sample to the new temperature, and the stabilization and recording procedures begin again. The program runs in this manner until the upper temperature limit specified by the user has been reached.

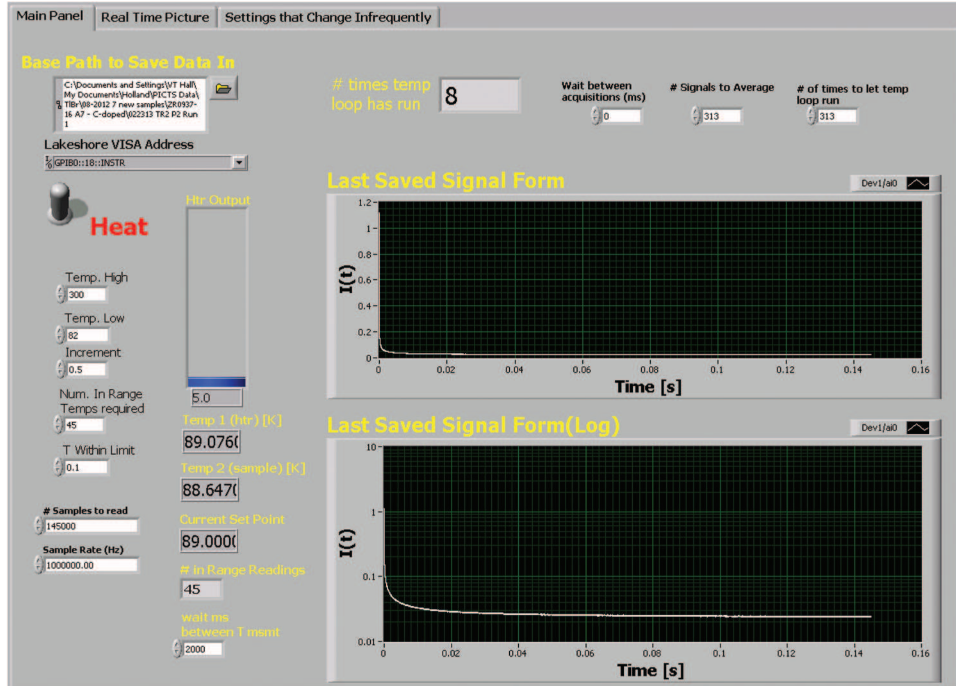

Figure 2.8: A screen shot of the front panel of the main PICTS program, written in LabView.

2.3.3 Data Analysis Software

A program to perform the two- and four-gate analysis schema introduced in section 2.2.2 was written in *Mathematica*. A complete annotated notebook is included in Appendix B.

2.4 PICTS Results on Semi-Insulating Gallium Arsenide (SI GaAs)

Once the system was constructed, calibration samples were required to show that the system functioned correctly. SI GaAs was the original material for which the PICTS technique was developed, and many reports of the results of PICTS measurements on SI GaAs exist in literature. Thus, SI GaAs was chosen as a suitable material to test the output of the system.

2.4.1 Sample Preparation

Six SI GaAs reference samples were made for PICTS measurements. The starting material was a bulk 300 micron-thick SI GaAs wafer grown by the liquid encapsulated Czochralski (LEC) method. Approximately 5 mm by 5 mm squares were cleaved from the wafer. The

cleaved samples were etched in HCl and masked with aluminum foil with cutouts for contacts. Rectangular Au/Ge/Ni contacts with thicknesses of 2000 Å/1000 Å/250 Å were deposited by electron beam evaporation. Both contacts were deposited on the polished side of the SI GaAs pieces to form a detector with planar geometry, with an intercontact spacing of ~2-3 mm. I-V measurements from -50V to 50V showed excellent linear behavior, confirming the ohmicity of the contacts.

2.4.2 PICTS Results

Figure 2.9 shows four-gate PICTS spectra for SI GaAs sample #6 calculated using rate windows (defined as t_2-t_3 in four-gate analysis) ranging from 170 to 8387 microseconds in length. Separate peaks in the spectra indicate separate traps, and the movement of each peak in temperature as the rate window is changed is what is used to determine the emission rate of the trap as a function of temperature, as described in section 2.1.1. Four peaks in the spectra were clearly resolvable and given labels A, B, C, and D, in order of increasing temperature at which they were discovered. Figure 2.10 shows the Arrhenius plots generated for the four peaks, and Figure 2.11 gives a summary of the calculated trap parameters.

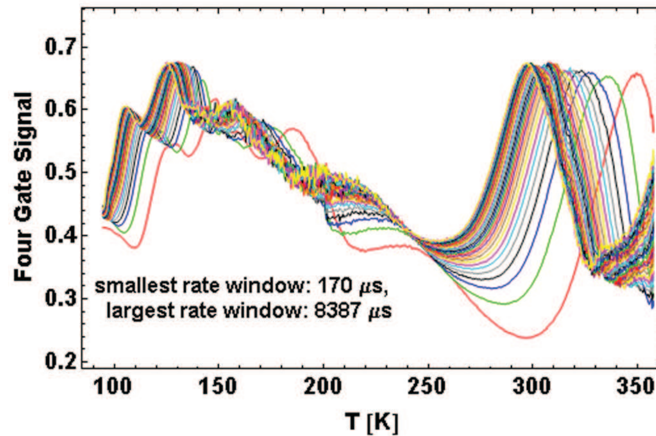

Figure 2.9: 4-Gate PICTS spectra shown for a SI GaAs sample.

2.4.3 Comparison with Literature

The calculated trap parameters from the four peaks that were clearly calculable were compared to reports of traps in SI GaAs recorded with PICTS in literature. The concentration and presence of various traps depend on growth methods as well as post-growth handling, and can vary greatly between different SI GaAS samples. Nevertheless, enough strong similarities between observed traps exist in literature to conclude with certainty when the same trap has been observed in different samples. Table 2.1 gives a summary of traps found with our system compared to similar traps reported in literature.

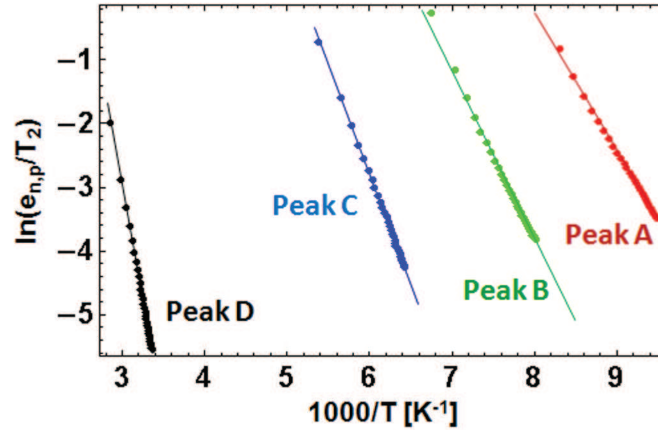

Figure 2.10: Arrhenius plots for four peaks shown in Figure 2.9.

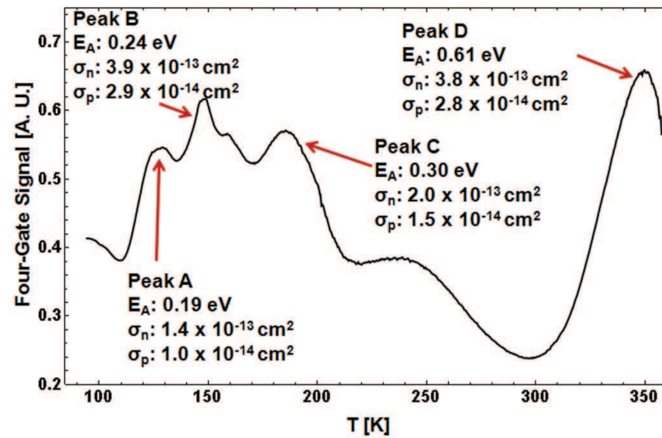

Figure 2.11: A single four-gate PICTS spectrum for SI GaAs sample #6, showing the calculated trap energies and trap parameters.

Both the general shape of the spectra and the values of the calculated trap parameters agree very well with several reports of PICTS on SI GaAs grown by the LEC method.

2.5 Conclusion

The construction of a modern PICTS system that records whole current transients was described, including details of the instrumentation and control software. The system records larger amounts of data than early PICTS system in order to allow the analysis to be done entirely in software, as opposed to using hardware to store processed data that takes up less space at the cost of losing some information about the original signal. SI GaAs samples were fabricated to compare the output of the new system with results reported in literature. SI

Table 2.1: Comparison of SI GaAs levels found with literature

Peak	Approx. Temp.	E_A [eV]	Literature Reports	Tentative Identification
A	110 K	0.19	0.19 eV [52]; 0.18 eV [53]	EL9, EL10, EL14
B	130 K	0.24	0.23 eV [52]; 0.21 eV [54]	EL8
C	160 K	0.30	0.34 eV [52]; 0.35 eV [54]	EL6
D	300 K	0.61	0.60 eV [52]; 0.61 eV [55]	

GaAS is a well studied material for which several groups have reported PICTS measurements. Four clearly resolvable traps were detected in the SI GaAs samples whose parameters agree very well with reported data. From these agreements, as well as from the overall quality of the signal and fit of the data to physical models, it was concluded that the system was ready to measure TlBr - a material for which only one PICTS report existed in literature previously.

Chapter 3

Electrical Characterization of Deep Levels in TlBr

In this chapter, the results of Photo-Induced Conductivity Transient Spectroscopy (PICTS) measurements are reported for nominally undoped, C-doped, and O-doped TlBr samples. These studies are the first of their kind on state-of-the-art detector grade material, provided by Radiation Monitoring Devices Inc. The measurements were performed using a system constructed at Lawrence Berkeley National Lab. A detailed discussion of the construction and calibration of the system is provided in Chapter 2.

3.1 Background and Theory

The role of deep levels in TlBr is relatively unexplored experimentally compared to what has developed in CZT over many years. Specifically, the level of understanding of the relationships between deep levels, resistivity, and carrier lifetime in CZT has not been reached yet for TlBr. Several groups have used optical techniques to look at mid-gap transition levels, which will be discussed in Chapter 4. Only a few reports of electrical characterization of deep levels in TlBr exist in literature. Kazukauskas et al. performed Thermally Stimulated Conductivity (TSC) measurements on TlBr single crystals grown by the Bridgman-Stockbarger method and found five potential deep levels. Their measurements were complicated by observations of persistent photoconductivity and sample prehistory effects.[56, 57] Another group reported the results of TSC and Photo-Induced Conductivity Spectroscopy (PICTS) measurements on TlBr crystals grown by the Bridgman method in various ambients.[58] These are the only reports of electrical measurements aimed directly at characterizing deep levels in TlBr, and none have been done on state-of-the-art nominally undoped detector grade TlBr grown by Traveling Molten Zone (TMZ).

Despite the small amount of experimental investigation, deep levels in TlBr are of great importance, as they influence both the resistivity and the electrical transport properties of the material. It is true in general that for a material with relatively high carrier mobilities

such as TlBr to be highly resistive, the free carrier populations must be low, which implies that the Fermi level must lie near the middle of the material's band gap. This can be seen from the equations for free electron and hole concentrations for an extrinsic semiconductor: [59]

$$\begin{aligned} n &= N_c exp(-\tfrac{E_C-E_F}{k_BT}) \\ p &= N_v exp(-\tfrac{E_F-E_V}{k_BT}) \end{aligned} \tag{3.1}$$

Here, E_C is the conduction band edge, E_V is the valence band edge, E_F is the position of the Fermi level within the gap, and N_c and N_v are the effective density of states of the conduction and valence bands respectively. These last two quantities are materials properties, given by the expressions $N_c = 2(2\pi m_e^* k_B T/h^2)^{\frac{3}{2}}$ and $N_v = 2(2\pi m_h^* k_B T/h^2)^{\frac{3}{2}}$, where m_e^* and m_h^* are the effective masses of electrons and holes. From the definition of the bandgap $E_G = E_C - E_V$, it can be seen that if $E_F = \frac{1}{2}E_G$ and if m_e^* and m_h^* are equal, the concentrations of free electrons, n, and holes, p, will be equal and minimized.

In an intrinsic semiconductor, free carrier concentrations are equal and the Fermi level lies naturally near the middle of the band gap at 0 K. Germanium is the only semiconductor with which crystal growers have achieved intrinsic purity at room temperature from an electrical standpoint. Even silicon, though close, has not been grown intrinsically pure, and the purest compound semiconductor ever grown, GaAs, has electrically active impurity concentrations many orders of magnitude above intrinsic levels. It can thus be concluded that TlBr is not resistive because it is grown to intrinsic purity. In most resistive materials, including CZT, deep levels pin the Fermi level near the middle of the gap. This mechanism creates a trade-off in detector material engineering in that deep levels are necessary for high resistivity, and yet their presence can have detrimental effects on carrier mobilities and lifetimes, via scattering and trapping. Though beyond the scope of this dissertation, balancing the concentration of deep levels to achieve desired resistivities while minimizing transport effects was the focus of much research in CZT and is a good example of a synergy between fundamental materials science and practical device improvement.[9, 12, 60, 61]

Though very few deep level studies have been conducted in TlBr, it would be reasonable to assume that the high resistivity in TlBr is also due to deep levels. However, an interesting theoretical paper by M. H. Du suggests an alternate mechanism of high resistivity for TlBr. Du argues that the Fermi level in TlBr may be pinned in the middle of the gap not by deep levels, but by shallow native donor and acceptor defects.[62] This compensation mechanism is illustrated schematically in figure 3.1.

It is impossible to achieve the uniformity of shallow donor and acceptor concentrations required for high resistivity by intentional doping, as no known doping method can guarantee such precision. Because the model proposed concerns native defects, the limits of doping precision are not relevant to assessing the idea, though they would certainly argue against the possibility of practical shallow level compensation if they were. Instead, the idea behind the argument for shallow level compensation in TlBr rests on Density Functional Theory (DFT) calculations of native defect formation energies and charge transition levels. By

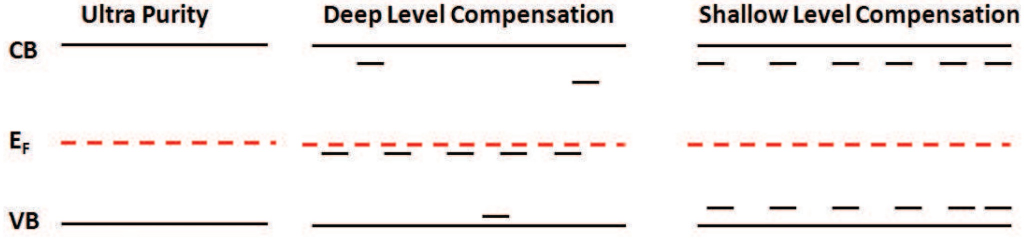

Figure 3.1: The three possible ways in which the Fermi level may lie in the middle of the bandgap of a semiconductor.

calculating the formation energies of Tl and Br vacancies, interstitials, and anti-site defects as a function of the Fermi level, relative equilibrium concentrations can be determined. In Du's work, the Schottky defect formation energy is found to have the lowest formation energy of all the native defects, suggesting that Tl and Br vacancies exist in the largest concentration of any native defects. Additionally, he finds that the respective Tl and Br vacancy formation energies are equal when the Fermi level is near the middle of the gap. From this, an equilibrium argument can be made that the Fermi level is pinned in the middle of the gap by shallow vacancies. Though beyond the scope of this dissertation, the argument amounts to saying that the Fermi stabilization energy of TlBr lies in the middle of the gap.[63]

The concept of Fermi stabilization energy is well supported experimentally, and there are known materials such as GaAs where the Fermi stabilization energy lies mid-gap. However, a typical stabilization energy argument relies on identifying a single dominant amphoteric defect level that changes its nature between being donor- and acceptor-like as the Fermi level shifts above and below the defect level. In this case, two shallow defect levels of opposing sign are proposed that are not amphoteric, but the principles are otherwise the same. TlBr growth is an equilibrium process, as opposed to a non-equilibrium method such as Molecular Beam Epitaxy (MBE). Therefore, it is reasonable to assume that native defects in the material exist in equilibrium concentrations, as opposed to defects and impurities specific to highly controlled growth conditions. Theoretically, the shallow compensation model cannot be immediately discarded, but without further experimental evidence, the correctness cannot be evaluated. The idea that resistivity can be achieved without high concentrations of deep levels however is an attractive one for detector science given that deep levels are responsible for lowering $\mu\tau$, as discussed previously. Deep level studies shine experimental light on these questions.

3.2 Experimental Methods

A liquid-nitrogen cooled IR Labs cryostat with a heated copper stage was used for PICTS measurements over the temperature range of 80-320 K. The TlBr samples were mounted to

sapphire substrates and thermally coupled to the copper stage with Apiezon N grease. The excitation source used was a CREE high-brightness light emitting diode peaked at 450 nm (2.76 eV). During a PICTS run, a bias of 25 V was applied across the contacts and the light was pulsed on for 350 ms and off for 150 ms. The PICTS measurements were performed with two polarities of bias in an attempt to separate electron and hole traps.[64] With a sandwich detector geometry and proper excitation conditions, the bias polarity determines which type of trap is more likely to be detected in a PICTS measurement.[65] To store the conductivity transients, a National Instruments USB-6210 ADC with a sampling rate of 1 MHz was used to digitize the output of a Keithley 428 current amplifier. Transients were recorded after stabilizing the temperature of the sample in increments of 0.5K across the whole temperature range of the measurement. At each temperature, conductivity transients were averaged at least 150 times before proceeding to the next temperature.

To analyze the data, both four gate and two gate analysis techniques were implemented in software. It was found that peaks were more easily resolved and distinct in the four gate analysis, owing to the significant variation of the baseline conductivity with temperature. Four gate analysis eliminates the temperature dependence of carrier mobilities and lifetimes from PICTS spectra.[49] In a typical four gate analysis, the rate window $t_2 - t_3$ was varied in width from 100 microseconds to 10 ms, and sampled a range of the conductivity decay from 100 microseconds to 20 ms. The normalization gates t_1 and t_4 were chosen so that t_4 was at least 10 times longer than t_3, and the ratios t_2/t_1 and t_3/t_1 were preserved when permuting gates. Nominally undoped TlBr has relatively long carrier lifetimes on the order of tens of microseconds at room temperature, increasing at lower temperatures.[10, 64] It was thus important to include rate windows starting well beyond these times to separate the thermally stimulated trap emission signal from the temperature dependent recombination signal.

A 150 ms conductivity transient recorded at 1 MHz generates 150,000 data points. Because of the relatively large size of such data, early PICTS systems reported in literature did not record whole transients, but rather stored only the time constant associated with the transient by using an analog single or double boxcar integrator, or correlator.[48, 50, 51] In this method, the raw transient data is lost, and only a processed signal is saved whose accuracy relies on the assumption that the photocurrent transient is composed of a single exponential process. If a transient exhibits unusual features, it would go undetected in such a system. As storage capacity of computers increased, ways of cleverly sampling transients were introduced to record more information without recording the whole signal.[66] With modern equipment however, it is now possible to store whole conductivity transients across a typical PICTS temperature range of several hundred Kelvin, obviating the need for analog signal post-processing. The extra cost in data storage is repaid by great flexibility in later data analysis. The system used in this dissertation was built to store whole transients. For a full PICTS run from 80-320K in increments of 0.5K, the system generates approximately 500 MB of data recording 150 ms transients sampled at 1 MHz. In this manner, no raw information contained in the conductivity transient is lost. As discussed in Section 3.3.4, this distinction was found to be important for studying transients in TlBr above 250 K.

3.3 PICTS on Nominally Undoped TlBr

3.3.1 Description of Nominally Undoped Samples

For PICTS measurements, five samples of nominally undoped detector grade TlBr were provided by Radiation Monitoring Devices, Inc. The five samples were cut from two different ingots labeled ZR43-62YD and ZR38-57YD. The crystals ZR38-57YD and ZR43-62YD were purified by 100 and 300 passes of zone refining, respectively. Both crystals were finally grown by the traveling molten zone (TMZ) method. A more detailed account of the growth and purification processes has been published elsewhere. [11] Pieces of dimension 5 mm x 5 mm x 500 microns were cut with a wire saw, lapped, and polished. To improve the surface quality, the samples used for PICTS were etched in a 5% Br-MeOH solution. Circular Cr/Au contacts with a 3 mm diameter were deposited by thermal evaporation on the top and bottom faces to form ohmic contacts. An I-V curve taken from an undoped sample with Cr/Au contacts provided by RMD is shown in Figure 3.2. The curve confirms that the contacts are not strongly rectifying, though a slight asymmetry is noticeable between the cases of reverse and forward bias. The presence of a built in electric field due to device polarization, discussed further in chapter 6, may be the reason for the asymmetry.

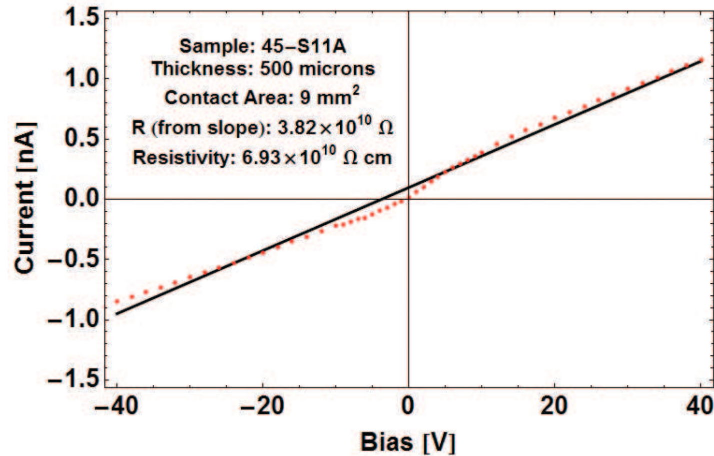

Figure 3.2: An I-V curve of a nominally doped TlBr sample with Cr/Au contacts. The curve follows an ohmic relationship, though a slight asymmetry is noticeable between cases of reverse and forward bias. The presence of a built in electric field due to device polarization could explain the asymmetry, and is discussed in Chapter 6.

After contacts were applied, the samples were wire-bonded and glued to sapphire substrates with gold pads to facilitate safe handling of the soft material. Thin 0.001" diameter palladium wires were used to connect the electrodes of the detector to the gold pads on the sapphire, secured in place by conductive carbon paste from Creative Materials. Thicker 0.008" diameter copper wires were attached to the gold pads with conductive silver epoxy.

The low curing temperature of the silver epoxy and carbon paste (75 °C) used was important, given the low melting point of TlBr (480 °C) and the unknown electronic effects of heating TlBr with metal contacts in atmosphere. Table 3.1 presents a summary of the nominally undoped samples used in PICTS measurements.

Table 3.1: Description of Nominally Undoped TlBr Samples

Sample Number	Name	Origin within ingot
#1	ZR43-62YD.A1	Head
#2	ZR43-62YD-PICTS1	Middle
#3	ZR43-62YD-PICTS2	Middle
#4	ZR38-57YD-PICTS1	Middle
#5	ZR38-57YD-PICTS2	Middle

3.3.2 Glow Discharge Mass Spectroscopy of Nominally Undoped TlBr Samples

Table 3.2: GDMS Summary of Nominally Undoped TlBr Samples

Element	Head Concentration		Middle Concentration	
	[ppm wt]	[cm^{-3}]	[ppm wt]	[cm^{-3}]
B	0.05	2.11 x 10^{16}	$<$ 0.01	$<$ 4.21 x 10^{14}
C	$\sim$ 4.5	$\sim$ 1.71 x 10^{18}	$\sim$ 8	$\sim$ 3.03 x 10^{18}
N	$<$ 1	$<$ 3.25 x 10^{17}	$\sim$ 2	$\sim$ 6.5 x 10^{17}
O	$\sim$ 2.5	$\sim$ 7.11 x 10^{17}	$\sim$ 10	$\sim$ 2.85 x 10^{18}
Na	0.03	5.94 x 10^{15}	$<$ 0.01	$<$ 1.98 x 10^{15}
Al	0.06	1.01 x 10^{16}	0.14	2.37 x 10^{16}
Si	$<$ 0.05	$<$ 8.11 x 10^{15}	0.06	9.73 x 10^{15}
K	0.63	7.34 x 10^{16}	1.2	1.40 x 10^{17}
Ca	0.02	2.27 x 10^{15}	$<$ 0.01	$<$ 1.14 x 10^{15}
Ti	0.04	3.80 x 10^{15}	$<$ 0.01	$<$ 9.51 x 10^{14}
Fe	$<$ 0.01	$<$ 8.15 x 10^{14}	0.05	4.08 x 10^{15}
Cu	0.02	1.43 x 10^{15}	0.02	1.43 x 10^{15}
I	$<$ 0.1	$<$ 3.59 x 10^{15}	$<$ 0.1	$<$ 3.59 x 10^{15}
Pt	$<$ 0.1	$<$ 2.33 x 10^{15}	$\leq$ 0.15	$\leq$ 3.50 x 10^{15}

The impurity concentrations of a zone-refined crystal vary along the length. To identify impurities present in the nominally undoped crystals, glow discharge mass spectroscopy (GDMS) was performed by Evans Analytical Group on samples cut from the head and

middle sections of the ZR43-62YD crystal. An edited summary of the concentration of impurities is given in Table 3.2. Only those impurities with concentrations greater than the detection limit of the system for the specific element (generally 0.01 - .5 ppm wt) are reported. Indium paste was used to mount the sample, and hence In results are also not reported.

3.3.3 PICTS of Nominally Undoped Samples below 250 K

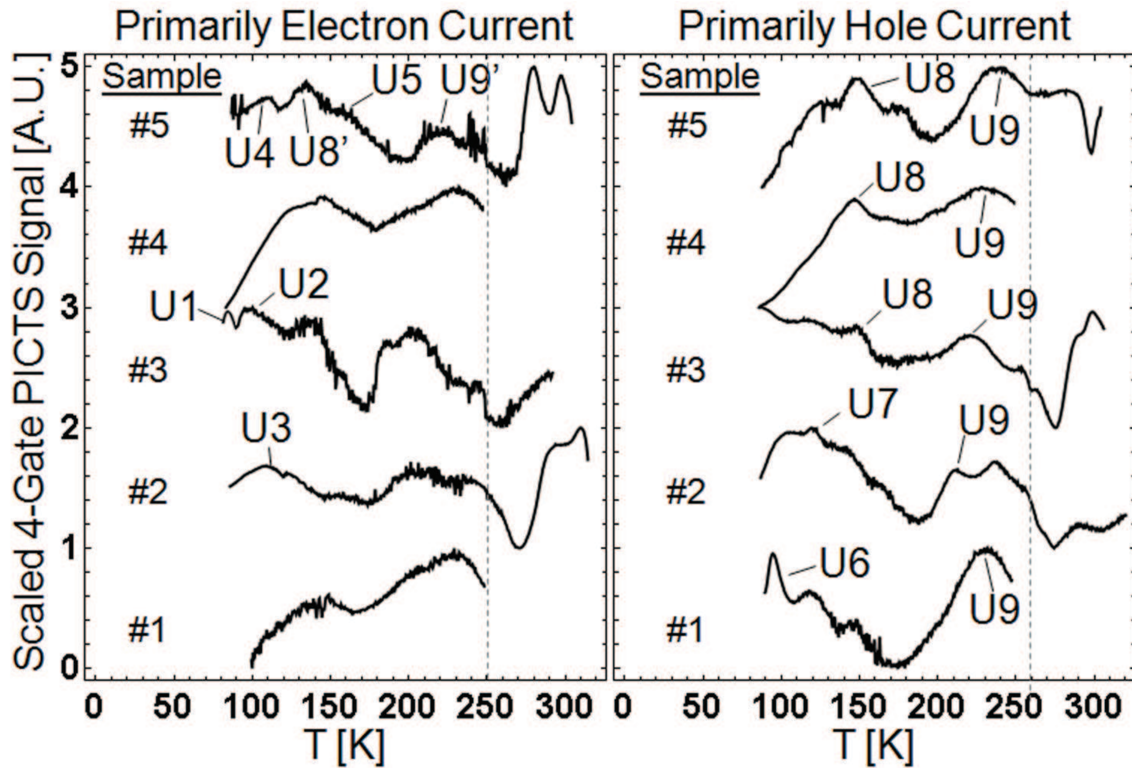

Figure 3.3: Four gate PICTS spectra for the 5 samples. Letters correspond to peaks from which trap parameters were calculated. Apparent peaks not marked by letters were either insufficiently distinct across multiple rate windows, or did not obey an Arrhenius relationship upon the changing of the rate window. Primed letters mark traps detected with both bias polarities.

The spectra of PICTS measurements using both bias polarities on all samples are shown in Figure 3.3. Distinct traps detected in a spectrum are marked with the letter “U” (to signify a nominally undoped sample), followed by a number. For reasons described in section 3.3.4, only the calculated values of traps discovered below 250 K are reported. Figure 3.3 shows the Arrhenius plots for the traps indicated in the spectra, and Table 3.3 presents a summary of their calculated parameters.

Five distinct traps were discovered running the PICTS experiment with the bias polarity favoring electron trap detection, and four traps were found with the bias polarity favoring hole trap detection. Among the apparent hole traps, trap U9 appears in all of the samples, and trap U8 appears in three. Traps found in different samples were judged to be the same based on similar Arrhenius plots, from which the calculated energy levels did not differ by more than 10-15%, and whose calculated capture cross sections agreed within approximately half of an order of magnitude. It is notable that none of the apparent electron traps appear conclusively in multiple samples.

Compared to the relatively sharp and distinct peaks of traps U1, U6, and U8, all other traps observed display broad peaks that often overlap depending on the rate window. Many of the spectra in which one peak is able to be calculated show features resembling other peaks, but with insufficient clarity over a wide range of rate windows to allow unambiguous identification. As an example, the hole trap spectrum for Sample #1 (ZR43-62YD-A1) shows features that strongly resemble those of peaks U7 and U8, but which overlap and occlude each other as the rate window is varied. In measurements of thermal emission from deep levels like PICTS and DLTS, broad overlapping peaks can indicate emission from deformation-induced levels such as point defects and dislocations.[67, 68] Broad peaks and line shape distortions are also characteristic of extended defects which form emission bands.[69]

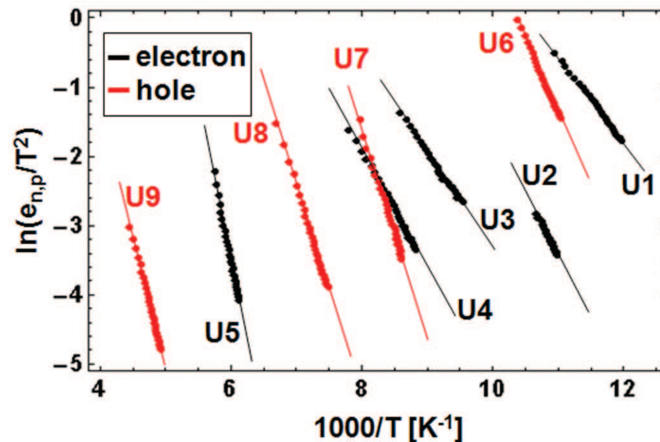

Figure 3.4: Thermal emission rates corrected by T^2 for the PICTS peaks observed in Figure 3.3.

TlBr is a soft material that is easily plastically deformed. It has been shown that various methods of cutting TlBr crystals, including delicate wire saw technique, lead to mechanically damaged surface layers from 20 microns to 1 mm thick.[70] Despite etching and careful handling, it is probable that defect centers related to stress and plastic deformations are present in the TlBr samples at significant concentrations. Deformation induces disorder on both the energy level and capture cross section of point defects.[71] Deformation-induced deep levels have been observed optically in TlBr.[72] It is thus possible that several of the

Table 3.3: Summary of Traps Detected with PICTS in Nominally Undoped TlBr

Trap Letter	Tentative Type	Sample(s) Found in	Activation Energy [eV]	Capture Cross Section [cm^2]
U1	electron	#3	0.11	9.4e-16
U2	electron	#3	0.16	4.6e-14
U3	electron	#2	0.12	6.1e-17
U4	electron	#5	0.14	2.5e-16
U5	electron	#5	0.41	1.0e-10
U6	hole	#1	0.19	3.1e-12
U7	hole	#2	0.26	2.9e-12
U8	hole	#3, #4, #5	0.26	7.7e-14
U9	hole	#1,#2, #3, #4, #5	0.34	7.6e-16

observed traps are related to deformation-related point and extended defects, though further experiments designed to study the matter are required. In contrast, traps U1, U6, and U8 could be related to point defects unassociated with structural deformation, such as impurities.

In sample #5, traps U8 and U9 were detected with both polarities of bias. The traps were determined to be the same based on very similar Arrhenius plots. This can be explained by the fact that the energy of the LED used, though higher than the indirect band gap of TlBr, was not high enough for complete absorption near the surface contact, which would ensure total separation of electron and hole currents through the bulk. Carriers of both types flowed through the bulk and were trapped during the illumination phase of the experiment, though in significantly different concentrations depending on the polarity. It was thus possible to measure carrier emission from a trap in both polarities, though in one polarity the signal would be much stronger than in the other. Both traps were more clearly resolved in the hole polarity spectra, and were found in other samples with only hole polarity bias as well, confirming their hole trap assignment.

The effect of the location of the crystal from which the sample was cut is noticeable in the electron trap polarity spectra. Sample #1 taken from the head of the ingot shows no resolvable electron traps and fewer spectral features compared to the samples taken from the middle of the crystal. In contrast, the spectrum of hole traps for sample #1 largely resembles that of the other samples, and features trap U9, which was found in all other samples. Further experiments employing intentionally doped materials and deliberately damaged materials would be useful to further explore the origins of the broad range of defect states in TlBr.

3.3.4 PICTS Signal Behavior above 250 K

It is generally desirable to go to as high a temperature as possible in a PICTS measurement in order to study the full energy range of deep levels. At higher temperatures, traps deeper in the band gap can be discovered. However, the conductivity transients above 250

K showed significantly non-exponential behavior, displaying unique shapes in both polarities previously unreported in literature. Figure 3.5 shows an example of the current recorded as a function of time after the end of the optical pulse for four different temperatures in the range 262-280 K. The dashed lines represent a rate window that could be used to analyze the signal. In an ideal measurement that isolates current from a single trap, the transient within the rate window should appear as a straight line in a log plot, with the slope changing with temperature. Even a transient containing components related to release from multiple traps should show a monotonically decreasing slope. Instead, within this temperature range a distinct increase in the slope dI/dt occurs in the transient and passes through the rate window as the temperature is increased, affecting any traditional PICTS analysis technique.

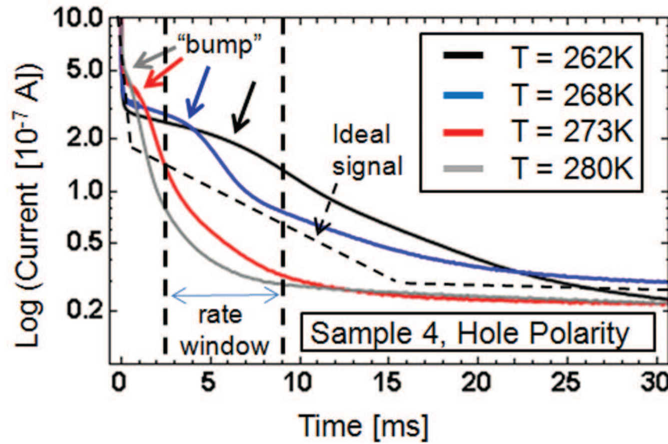

Figure 3.5: Current transients recorded after the LED was turned off at four different temperatures, plotted on a log scale. The dashed lines represent a typical rate window used in analysis. The transients exhibit an anomalous shape defined by non-monotonic dI/dt slope behavior within the rate window.

Figure 3.6 shows the results of applying a regular four-gate analysis to these transients. A peak appears centered near 270 K, within the range where the transients show strongly anomalous shapes. Varying the rate window and applying an Arrhenius analysis to the calculated emission rates yields an excellent fit, as shown in the insets of Figure 3.6. However, the calculated trap parameters from the analysis are unphysical. It is unlikely that a trap with depth 0.94 eV could be detected at such a relatively low temperature, and a cross section of $\sim 10^{-7}$ cm^2 is several orders of magnitude larger than typically measured values. Moreover, the four gate analysis assumes a series of rate windows can be identified over which the transient signal is dominated by a single exponential. The raw transient data shows that this is not the case. Thus, the analysis must be discarded as incorrect, though the quality of the Arrhenius fit would be tempting to trust. At least one previous report has noted the perplexing calculation of unphysical trap parameters when measuring PICTS of TlBr.[58] The group did not record complete transients and used simple two-gate analysis.

The full acquisition of the complete transient here suggests that two or four gate analysis is fundamentally inadequate at higher temperatures in TlBr.

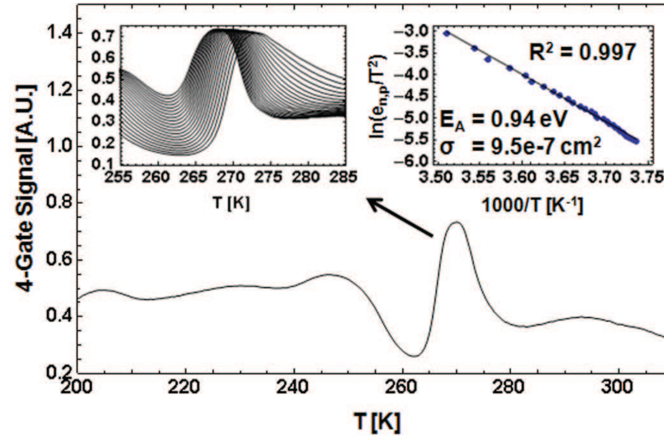

Figure 3.6: An apparent trap, analyzed with a traditional four gate technique, in the range T = 260-280K. The inset on the upper left shows the variation of the peak position with different rate windows ranging from 2 to 7 ms wide and starting from 500 to 1500 microseconds into the transient. The inset on the upper right shows the resulting Arrhenius plot and calculated trap parameters.

The cause of the anomalous photoconductivity transient shapes is unknown. A similar shape appeared in all measurements using both polarities of bias on the three samples that were heated above 250 K. In some cases, the slope of the conductivity transient switches sign from negative to positive before turning negative again, leading to the phenomenon of negative peaks in the PICTS spectrum for certain rate windows. It is unclear whether the transient process is of electronic or ionic origin, and further experimental investigation and modeling is required to explore the shapes further.

3.4 PICTS on Doped TlBr: TlBr:C, TlBr:O

3.4.1 Description of Doped Samples

Radiation Monitoring Devices provided 4 C-doped and 1 O-doped TlBr samples. The exact procedures for doping TlBr with C- and O- are the intellectual property of Radiation Monitoring Devices. Carbon was introduced into the TlBr crystal by adding carbon tetrabromide (CBr_4). Oxygen was incorporated by growing the crystal in an atmosphere of air, provided by a cylinder of compressed air. In contrast, nominally undoped TlBr is grown in an atmosphere of HBr and argon gas. Table 3.4 summarizes gives a summary of the details of the doped samples.

Table 3.4: Description of TlBr:C and TlBr:O Samples

Sample Number	Name	Origin within ingot	Dopant
PICTS-6	ZRC0937-16-A6	Head	C
PICTS-7	ZRC0937-16-A7	Head	C
PICTS-8	ZRC0937-16-B6	Middle	C
PICTS-9	ZRC0937-16-B7	Middle	C
PICTS-10	ZRC0937-17-A52	Head	O

3.4.2 Secondary Ion Mass Spectrometry (SIMS) of TlBr:C and TlBr:O

In order to verify the incorporation of dopants in each crystal, pieces cut from the head of both the C- and O-doped crystals were sent to Charles Evans and Associates for secondary ion mass spectrometry (SIMS). The SIMS data show the concentration of each dopant as a function of depth into the crystal. The observed concentrations of $\sim 10^{18} - 10^{19}$ cm^{-3} are several orders of magnitude above background concentrations of most of the impurities detected with GDMS in the nominally undoped samples (see section 3.3.2). The incorporation of the desired dopant was successful.

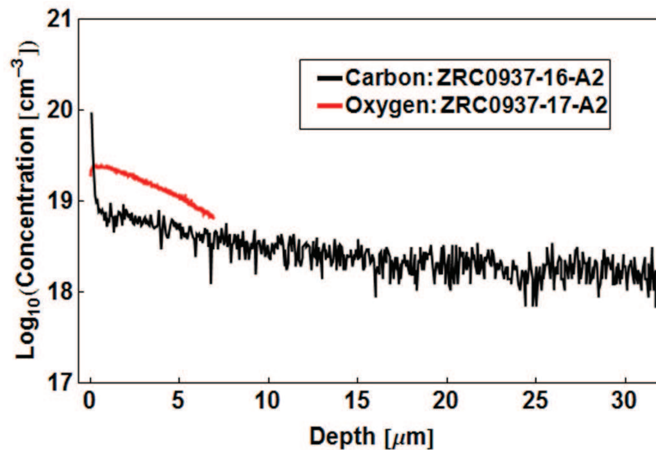

Figure 3.7: SIMS data showing the concentration of C and O dopants in the doped TlBr samples as a function of depth from the sample surface.

3.4.3 PICTS on TlBr:C

The spectra of PICTS measurements using both bias polarities on all samples are shown in Figure 3.8. Distinct traps detected in a spectrum are marked with a letter. For reasons

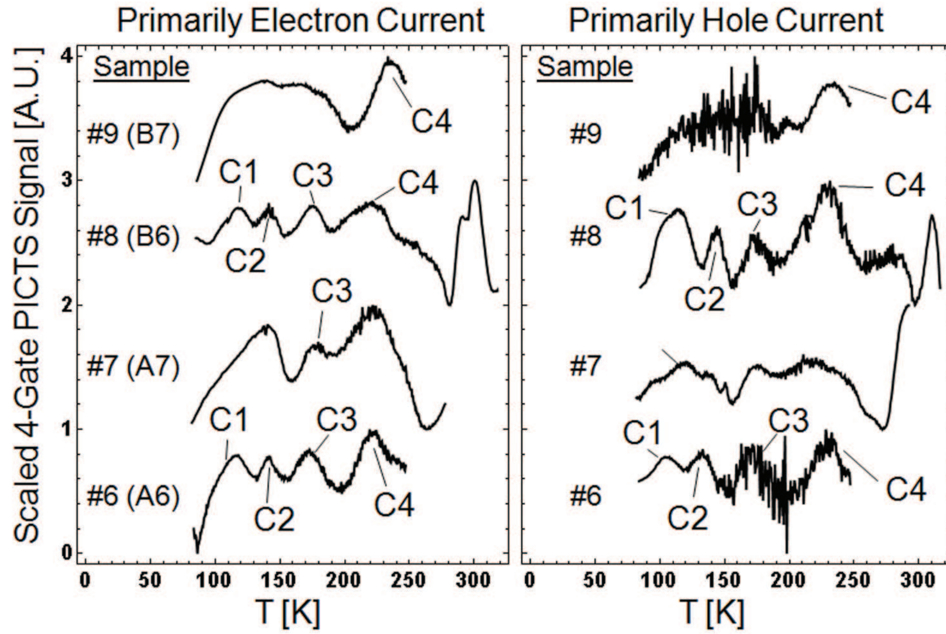

Figure 3.8: PICTS spectra for the four C-doped TlBr samples.Traps for which parameters could be calculated are marked with letters.

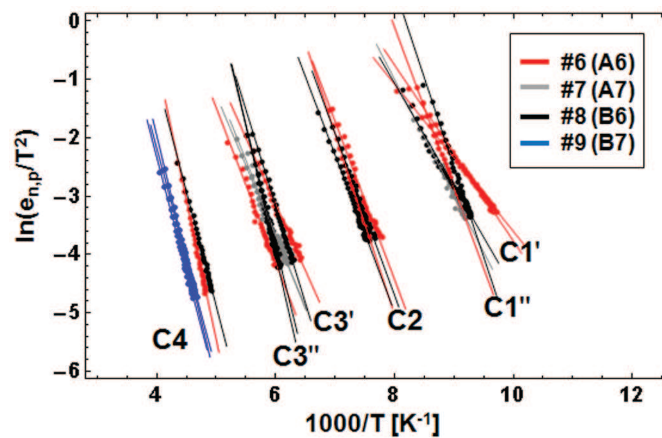

Figure 3.9: Arrhenius plots for traps found in C-doped TlBr. The colors correspond to the sample in which the trap was detected.

Table 3.5: Summary of Traps detected in C-doped TlBr

Trap Letter	Sample Number	Polarity	Energy [eV]	σ_e [cm^2]	σ_h [cm^2]	R^2
C1′	A6	electron	0.13	1.4e-16	3.3e-17	0.997
	A6	hole	0.11	1.4e-17	3.4e-18	0.998
	A7	hole	0.17	2.0e-17	4.7e-18	0.988
	B6	electron	0.15	7.6e-16	1.8e-16	0.985
C1″	A6	electron	0.24	5.8e-12	1.4e-12	0.997
	B6	hole	0.26	1.5e-10	3.5e-11	0.988
C2	A6	electron	0.27	6.6e-13	1.6e-13	0.998
	A6	hole	0.23	5.2e-14	1.2e-14	0.957
	B6	electron	0.24	6.6e-14	1.6e-14	0.972
	B6	hole	0.24	3.4e-14	8.1e-15	0.985
C3′	A6	electron	0.20	6.2e-17	1.5e-17	0.980
	A6	hole	0.23	2.2e-16	5.2e-17	0.980
	A7	hole	0.20	6.1e-17	1.4e-17	0.983
	B6	hole	0.26	7.6e-15	1.8e-15	0.993
C3″	B6	electron	0.38	1.3e-11	3.0e-12	0.992
	B6	hole	0.36	2.0e-12	4.7e-13	0.983
C4	A6	electron	0.37	2.4e-14	5.7e-15	0.981
	B6	electron	0.34	4.0e-15	9.5e-16	0.995
	B7	electron	0.33	7.6e-16	1.8e-16	0.998
	B7	hole	0.36	5.5e-15	1.3e-15	0.995

described in section 3.3.4, only the calculated values of traps discovered below 250K are reported. The C-doped PICTS spectra show a total of four traps, which are labeled C1, C2, C3, and C4. In contrast to the case of undoped TlBr, many of the traps show up in both the electron and hole-polarity spectra. As discussed in Section 3.3.3, this phenomenon is possible given the experimental conditions, but it makes it difficult to determine whether the detected trap is an electron or hole trap. The traps discovered in C-doped material are thus not assigned a tentative trap type. A summary of the calculated trap parameters is given in Table 3.5.

Figure 3.9 shows the Arrhenius plots for all of the traps indicated in the spectra. It can be seen that the trap signatures form four distinct groups. However, within some of these groups, strong variation exists between the slopes and y-intercepts that lead to variation in the calculated energy and capture cross-section values. The magnitude of variation is characteristic of traps with broadened peaks due to plastic deformation within the material. In this case, it is useful to adopt the convention of identifying traps not only on activation energy and capture cross section, but on their Arrhenius plot as well. Such a convention is typical in deep level studies of plastically deformed Si, as well as GaAs. [67]

The variation of energy level and cross section is more significant in the C1 and C3 groups compared to the C2 and C4 groups. It can be seen that the spread in recorded activation energies can be greatly reduced by breaking C1 and C3 into two groups, labeled C1′, C1″, C3′, and C3″. The C1 group spans activation energies from 0.11 to 0.26 eV, but C1′ and C1″ span a range from 0.11 eV to 0.17 eV and from 0.24 eV to 0.26 eV respectively. Similarly, the C3 group spans activation energies from 0.20 to 0.39 eV, but C3′ and C3″ span a range from 0.20 eV to 0.26 eV and from 0.36 eV to 0.38 eV. In contrast, calculated energies from C2 span the range 0.23-0.27 eV, and those from C4 span the range 0.34 eV to 0.37 eV. For comparison, activation energies calculated with PICTS measurements and reported in literature frequently vary by 10% to 20% and capture cross sections by one to two orders of magnitude, even in materials without defect level broadening due to deformation.

3.4.4 PICTS on TlBr:O

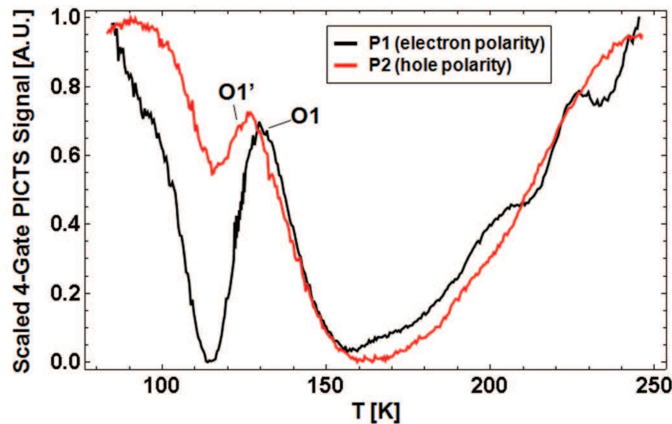

Figure 3.10: PICTS spectra for sample #10, O-doped TlBr.

Table 3.6: Summary of Traps detected in O-doped TlBr

Trap Letter	Polarity	Energy [eV]	σ_e [cm^2]	σ_h [cm^2]	R^2
O1	electron	0.18	5e-15	1.2e-15	0.994
	hole	0.17	1.5e-15	3.5e-16	0.998

The PICTS spectra measured with electron and hole polarity for O-doped Sample #10 below 250 K are shown in Figure 3.10. Only a single peak yielded calculable parameters in both polarities, though the electron polarity spectrum shows more potential features. The Arrhenius plots for the peaks are shown in Figure 3.11. Based on the similarity of

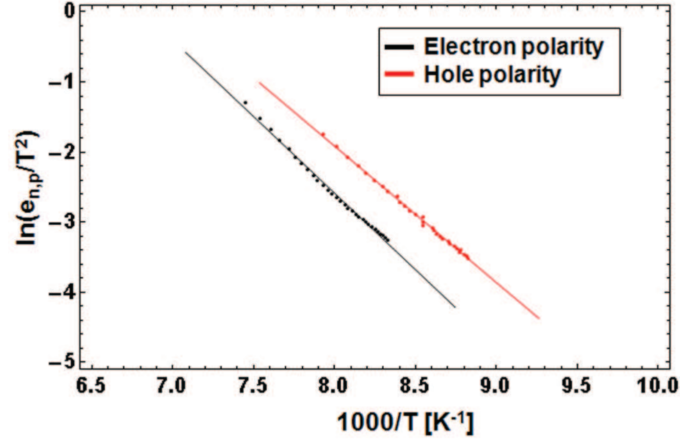

Figure 3.11: Arrhenius plots for traps detected in O-doped TlBr.

the Arrhenius plots and calculated activation energies, it is likely that the single calculable trap is the same in both spectra. Therefore, the tentative trap type is not assigned. The calculated trap parameters are summarized in Table 3.6.

3.5 Discussion of Results

3.5.1 Traps in Common

Figure 3.12 shows all of the Arrhenius plots for traps detected with PICTS in nominally undoped, C-doped, and O-doped TlBr samples. By comparing Arrhenius plots, it is possible to determine if traps detected in two different materials are likely to be the same. From the figure, it can be seen that the greatest diversity of Arrhenius plots occurs for traps detected at or below a temperature of ∼120 K, which includes traps U1-U4, U6, U7, C1′, C1″, and O1. These traps span a wide range of energies and capture cross sections, and include the shallowest traps detected, since the depth of detectable traps decreases with the temperature. Less variation in calculated trap parameters and Arrhenius plots occurs in traps detected above ∼120 K.

Judging from the plots in Figure 3.12, the following traps are likely the same:

- C1′ = U3
- O1 = U4
- C2 = U8
- C3″ = U5
- C4 = U9

Based on these observations, all of the traps observed in C-doped material were also observed in nominally undoped material, with the exception of C3′. If C3′ is a distinct trap from C3″, then it is possible that the carbon doping is responsible for the presence of the trap. The single calculable trap observed in the O-doped material was also found in nominally undoped material. Thus, oxygen doping does not appear to introduce unique deep levels measurable with PICTS in the temperature range from 80 - 250 K. With PICTS measurements alone, the origins of observed traps cannot be determined. However, it can be concluded that traps that are the same between samples of different doping are therefore likely unrelated to the dopant.

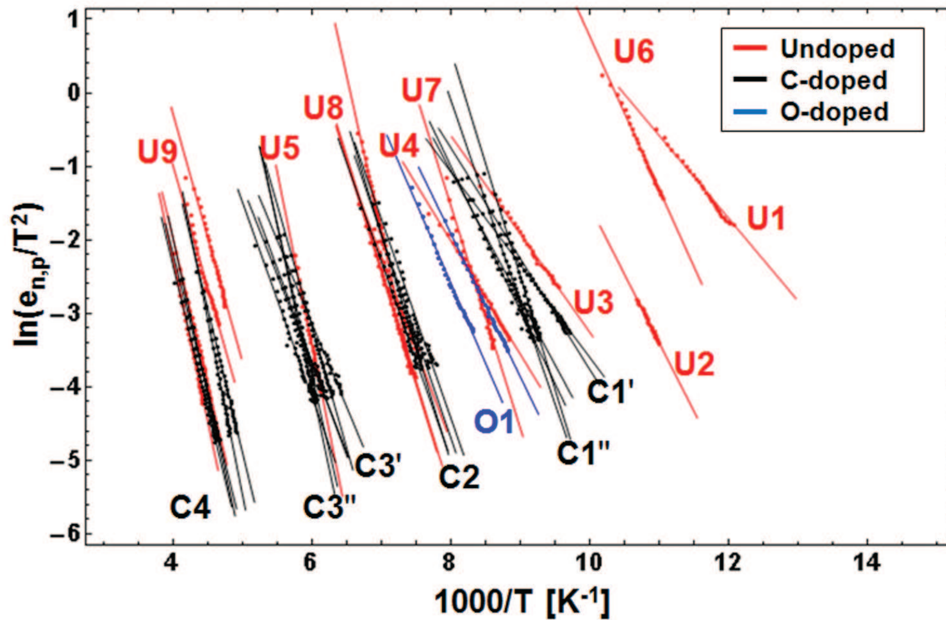

Figure 3.12: Comparison of the Arrhenius plots of traps detected in nominally undoped, C-doped, and O-doped TlBr.

3.5.2 Implications for the Origin of Resistivity in TlBr

The detection of deep levels with both electrical and optical techniques has implications for understanding the origin of resistivity in TlBr. As discussed in the introduction, it has been suggested that the Fermi level in TlBr is pinned near the middle of the gap by donor and acceptor shallow levels introduced by Tl and Br vacancies existing in equal concentrations.[62, 73] For this mechanism to be valid, Tl and Br vacancies must be the dominant defects in the material.

Let us consider an ideal TlBr crystal whose only electrically active defects are shallow Tl and Br vacancies existing in equal concentrations. The Fermi level is located near the middle of the gap, at the location at which the formation energy of the vacancies are equal.

Now let us assume a deep level defect is added into the crystal. As an example, we will choose trap U9, a hole trap about 0.34 eV from the valence band edge, which was detected in all five samples. Introducing trap U9 into the idealized crystal will have the effect of moving the Fermi level further toward the valence band. In doing so however, the formation energies of the Tl vacancies would increase and that of Br vacancies would decrease, as the formation energies of charged defects scale linearly with the position of the Fermi level. Thus, in an equilibrium growth process, an excess concentration of Br vacancies would form relative to Tl vacancies in order to compensate the deep level, keeping the Fermi level near the middle of the gap. This mechanism could occur as long as the concentration difference of the shallow vacancies, $|N_{D,shallow} - N_{A,shallow}|$, can adjust itself to equal the concentration of deep levels, $N_{A,deep}$. If the concentration of the deep level $N_{A,deep}$ was greater than the concentration difference between the shallow levels $|N_{D,shallow} - N_{A,shallow}|$ however, and if $N_{D,shallow} > N_{A,shallow}$, then the Fermi level would be pinned by the deep level near 0.34 eV above the valence band.[74] Thus, the relative concentrations of deep and shallow levels determine the position of the Fermi level and whether it is pinned by the shallow vacancies or the deep level.

The formation energy of a Schottky defect in TlBr has been experimentally measured to be 0.91 +/− 0.03 eV.[39] For a TlBr crystal cooled from a melt slowly to room temperature, this corresponds to Tl and Br vacancy concentrations on the order of 10^{15} cm^{-3}. While it is difficult to determine exact trap concentration information from PICTS measurements alone, the low end of typical concentration values reported and corroborated with capacitance DLTS measurements are 10^{12} cm^{-3} to 10^{13} cm^{-3}. Thus, if all of the traps detected in this study exist in concentrations lower than 10^{15} cm^{-3}, at the lower end of the sensitivity of PICTS measurements, then $|N_{D,shallow} - N_{A,shallow}|$ can adjust itself in an equilibrium process to compensate other electrical impurities, and the Fermi level position is controlled by the shallow donor and acceptor native defects introduced by Tl and Br vacancies.

However, it is also possible that deep levels in the material exist in concentrations equal to or exceeding the concentrations of native defects. This seems likely considering that many of the impurity atoms detected with GDMS, presented in Table II exist in concentrations on the order of 10^{15} cm^{-3} or higher. In this case, deep levels would pin the Fermi level and thus be responsible for the high resistivity of the material, as is the case in other well known highly resistive semiconductors such as SI GaAs and CZT. If trap U9 had the highest concentration relative to other traps and native defects, the Fermi level would be near 0.34 eV offset from the valence band, which is not deep enough to correspond to the measured resistivity values of 10^{10} $\Omega \cdot cm$ common to TlBr. Consequently, if deep levels pin the Fermi level in TlBr, there must be another level deeper than trap U9 in the samples we measured in order to for the samples to have the experimentally noted resistivity. The broad luminescence bands with peaks near 1.8 eV and 2.0 eV observed in the CL spectra and discussed in Chapter 4 correspond to defects with energies deep enough to pin the Fermi level at a position sufficient for high resistivity.

The Fermi level in TlBr must be offset by at least ∼0.7 eV from the top of the conduction band or bottom of the valence band in order to have free carrier concentrations on the order

of 10^7 cm^{-3}, and hence a resistivity of 10^{10} $\Omega \cdot cm$ or greater. However, it is not necessarily true that the Fermi level is pinned at 0.7 eV for a material with a resistivity measured at room temperature or higher of 10^{10} $\Omega \cdot cm$, as has been asserted.[10, 75] There is some experimental evidence that ionic conductivity dominates the total conductivity of the material at room temperature[38, 39, 40, 41]. Thus, the Fermi level could lie much deeper than 0.7 eV from a band edge leading to a higher purely electronic resistivity, but ionic conduction limits the total resistivity of the material to $\sim 10^{10}$ $\Omega \cdot cm$ at room temperature.

3.6 Conclusion

In this chapter, the first PICTS studies of state-of-the-art detector grade TlBr samples using 4-gate analysis are reported. For the five nominally undoped samples, a total of nine traps were detected in the temperature range from 90-250 K, their parameters calculated, and their trap types tentatively assigned. The broadened appearances of many of the trap peaks bear similarities to those found in deep level studies of mechanically damaged materials. The sample taken from the head end of the zone refined crystal was found to have fewer electron traps than samples from the middle, but equal numbers of resolvable hole traps. Six traps were found in the C-doped samples, and five of them were found to correlate with levels also present in nominally undoped TlBr. One trap was found in a single O-doped TlBr sample, and also correlated to a level found in the nominally undoped material. The implications of the deep levels on the origin of resistivity and position of the Fermi level in the material were discussed in light of the PICTS results. The theory that native shallow defects as opposed to deep levels pin the Fermi level mid-gap in TlBr is shown to be unlikely based on the experimental evidence.

Above 250 K, anomalous photoconductivity transient shapes were discovered, previously unreported in literature. Their discovery was enabled by a PICTS system that records whole photoconductivity transients as opposed to a processed signal (see Chapter 2 for further details). These shapes indicate other physical processes leading to conductivity transients convoluted with the signal from trap emission, and preclude the accurate determination of trap parameters using traditional PICTS analysis techniques. It is not known if the origin of the anomalous transient features is ionic or electronic. It is likely that both further experiment at temperatures in which the transients occur as well as modeling will be necessary to understand the origin of the signal.

Chapter 4

Optical Characterization of Deep Levels in Doped and Undoped TlBr

In this chapter, photoluminescence and cathodoluminescence measurements on TlBr are reported. In both of these techniques, light emitted from TlBr samples is recorded after excitation by a laser or an electron beam. The emission spectra reveal electronic transitions related both to intrinsic band features as well as extrinsic features. The emission data are compared to PICTS results in an effort to correlate deep level transitions observed with optical and electrical techniques.

4.1 Background and Theory

Early experimental studies of the emission spectra of TlBr were focused on establishing intrinsic features of the band structure of TlBr, in order to corroborate features predicted from theoretical calculations as well as to confirm experimental results of absorption experiments. Mid-gap emission peaks potentially originating from impurities were observed in the process, but were hindrances to the study of intrinsic band features. The intrinsic features common to nearly all reported emission spectra are sharp emission lines near 3.02 eV, and 2.65 eV, with expected variation amongst reports owing to different measurement temperatures and detector resolution. The line near 3.02 eV is universally attributed to a radiative transition across the direct band gap of TlBr, which has been well established by absorption measurements, as well as theoretical calculations. [76, 77, 78]. The emission line near 2.65 eV was first reported by Shimizu et al. and interpreted as a transition involving an indirect bandgap.[79] Shimizu's interpretation explained earlier observations of an onset of absorption at this value, which had been considered to be an Urbach tail, as well as features of the photospectral conductivity of TlBr. [76, 78] Subsequent emission measurements found the same emission line near 2.65 eV and supported the interpretation of an indirect transition.[80, 81, 82, 83, 84, 70].

The intensity of the indirect transition peak in TlBr emission spectra is strong, and there

is some debate in the literature about the transition pathway. Because of wave-vector conservation requirements, the radiative recombination of an electron and hole across an indirect band gap must be assisted by a phonon. The frequency of indirect recombination is orders of magnitude lower than direct recombination.[85] The indirect band gap of TlBr is lower than the direct bandgap, and photo-generated electrons in the conduction band rapidly thermalize to the indirect band minimum. The thermalization occurs on the order of picoseconds, compared to direct bandgap radiative recombination time scales of nanoseconds.[86, 87] This explains why the the indirect band gap is prominent relative to the direct band gap, as well as the observed phenomenon that the direct bandgap emission line is most visible in conditions of high excitation, when the indirect transition capacity is saturated. Shimizu et al. postulated that the 2.63 eV emission line is due to excitons bound at an isoelectronic impurity. Isoelectronic impurities break the translational invariance of the crystal, enabling optical transitions by relaxing the conservation of wave vector requirements. Nitrogen in the indirect gap semiconductor GaP is a famous example of this phenomenon.[85] A later report studying the effect of isoelectronic Cl doping in TlBr found no increase in the emission peak intensity near 2.63 eV with an increase in concentration of Cl-dopants, implying that the edge emissions are not related to the presence of Cl. The same report attributes the 2.63 eV emission line to the zero-phonon radiative decay of free excitons.[80] At least two reports of emission spectra do not show the transition near 2.65 eV at all, though insufficient crystal purity could be the reason.[88, 72]

Deep levels due to impurity atoms or defects are localized in real space, and hence broad in k-space. They provide additional optical transition possibilities which appear in emission spectra as photons with energies lower than the lowest band gap transition. A summary of the principle radiative recombination processes deep levels participate in is shown in Figure 4.1. When a trap captures a single free carrier without recombination, a photon can also be released with an energy equal to the optical ionization energy of the trap level. Photons originating from a process involving deep levels contain information about the position of the deep level within the gap, though they cannot be referenced to a specific band edge or mid-gap level without further experiments. Emission spectra can be usefully compared to deep level spectroscopy measurements such as PICTS, though one must be mindful of the difference between optical and thermal ionization energies. A detailed discussion of the difference between these two energies from a thermodynamical perspective can be found in several references.[89, 42]

Very little work has been done to identify impurity or defect-related emission in TlBr. Defects and impurities are typically characterized by broad emission bands with widths of several tenths of an eV, compared to sharper intrinsic or atomic transitions. In TlBr, several groups have reported a broad emission band near 2.45 eV. The origin of the peak is the subject of debate in literature. Proposed attributions of the origin include intrinsic lattice imperfections, structural deformation, unknown impurities, free-bound carrier recombination, cation vacancies and Frenkel pair recombination.[90, 72, 88, 82, 91, 92] The emission peak with the greatest agreement amongst researchers is a peak near 2.20 eV attributed to the presence of iodine. Working with iodine-doped material, Nakahara et al. found the inten-

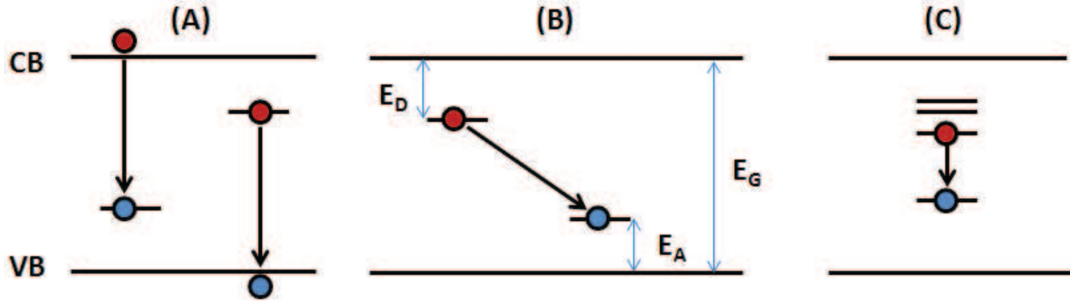

Figure 4.1: The three principle ways deep levels can participate in radiative recombination. (A) Free electrons or holes are captured by respective traps, releasing a photon in the process. (B) Donor-acceptor pair recombination. (C) Recombination between discrete atomic energy levels of a single impurity atom. From Reference [87]

.

sity of the peak near 2.20 eV to scale linearly with the concentration of iodine dopants.[80]. Subsequent reports of iodine-doped TlBr confirmed the finding, attributing the transition to a bound exciton at an iodine impurity.[88, 92]

4.2 Experimental Methods

4.2.1 Sample Preparation

Five nominally undoped sample from the same two nominally undoped crystals reported in Section 3.3.1 were used for luminescence measurements. One of the samples measured, Sample #1, was the exact same sample used in the PICTS measurements, and thus had polished surfaces and contacts. For the other four samples, 5 mm x 5 mm x 3 mm thick samples were cut from the same slices of the ingots as the PICTS samples. In contrast to the PICTS samples however, these were left unpolished and uncontacted. Table 4.1 summarizes the preparation details of the samples.

Four C-doped TlBr samples were provided for optical measurements. These samples of dimension 5 mm x 5 mm x $\sim$ 3mm were cut from the same slices of ingots as their counterparts for PICTS measurements, but were left unpolished and uncontacted initially. They were later polished for additional PL measurements. One O-doped TlBr sample was also used in optical measurements. This was the same sample used in PICTS measurements. A summary of all samples measured is given in Table 4.1. It is important to note that the numbers given to the samples are for the convenience of referencing them in this chapter only, and that the same sample may have a different number in another chapter.

Table 4.1: Description of Nominally Undoped TlBr Samples Used in Optical Measurements

Sample Number	Name	Origin within ingot	Surface Preparation	Dopant
#1	ZR43-62YD.A1	Head	polished and etched	-
#2	ZR43-62YD-PL1	Middle	as cut	-
#3	ZR43-62YD-PL2	Middle	as cut	-
#4	ZR38-57YD-PL1	Middle	as cut	-
#5	ZR38-57YD-PL2	Middle	as cut	-
#6	45-S10	Middle	polished and etched	-
#7	ZRC0937-16-A6	Head	as cut (polished later for PL)	C
#8	ZRC0937-16-A7	Head	as cut (polished later for PL)	C
#9	ZRC0937-16-B6	Middle	as cut (polished later for PL)	C
#10	ZRC0937-16-B7	Middle	as cut (polished later for PL)	C
#11	ZRC0937-17-A5	Head	polished and etched	O

4.2.2 Photoluminescence System Description

PL measurements were performed on the UV-Vis PL system in the Electronic Materials Program at Lawrence Berkeley National Laboratory. A HeCd laser with a fundamental wavelength of 325 nm (3.81 eV) and a power of 50 mW was used as the excitation source. The laser light was directed onto the sample with optics. Sample luminescence was collected with a focusing lens and directed to a SPEX 1404 0.85 m double spectrometer. A Hamamatsu R928 photomultiplier tube operating at room temperature served as the detector. The detectable wavelength range of the system in this configuration is 325 nm (limited by the laser energy) to 800 nm (limited by the grating in the spectrometer).

4.3 Photoluminescence Results

4.3.1 PL of Nominally Undoped TlBr

Representative PL spectra from nominally undoped TlBr are shown in Figure 4.2. The spectra of unpolished nominally undoped TlBr samples were found to differ from those of polished samples. The spectrum from Sample #6 shows a typical result for a polished undoped TlBr sample at 8 K. The spectrum is dominated by two narrow and sharp peaks centered at 2.98 eV and 2.60 eV. The sharpness of the peaks are in accordance with intrinsic band transitions, and their maxima are in excellent agreement with the direct and indirect band-gap transition energies of TlBr. In Figure 4.2, the two peaks related to the indirect and direct transitions respectively are marked with the letters A and B. A third broad peak, barely distinguishable in the figure, is centered at 1.75 eV. This broad defect luminescence is much weaker than the luminescence from the two intrinsic transitions.

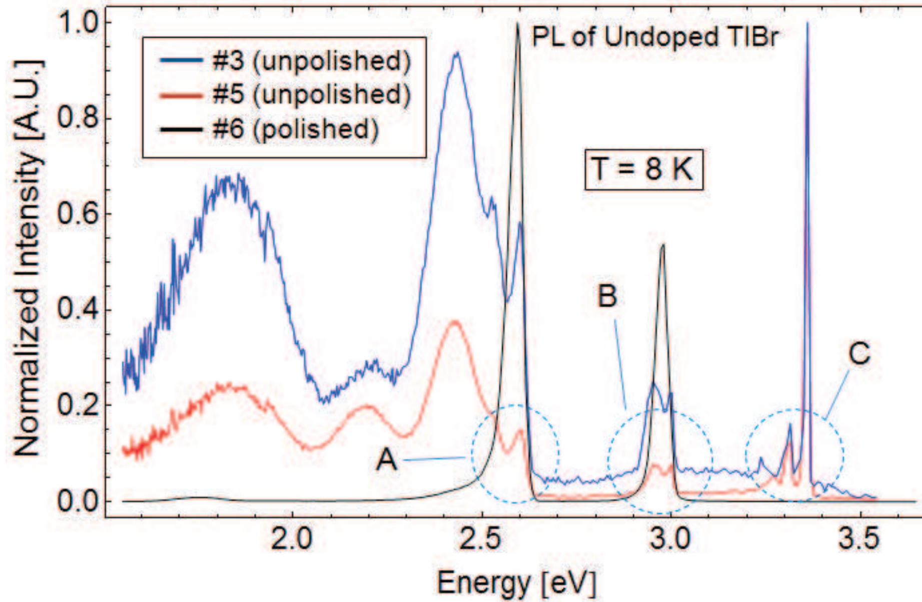

Figure 4.2: Photoluminescence spectra of nominally undoped TlBr, showing the difference between polished and unpolished samples.

The spectra from unpolished nominally undoped TlBr samples show additional features that are not found in the spectra from polished samples. The intrinsic transitions related to the indirect and direct band gaps are visible. However, the unpolished samples also show large defect peaks centered near 1.8 eV, 2.2 eV, and 2.4 eV. Furthermore, a cluster of very sharp lines appears near 3.3 eV. This cluster has been marked with the letter C in Figure 4.2. These lines are interesting in that they occur above the direct band gap of TlBr. Above-bandgap luminescence in ionic crystals associated with impurities has been reported in literature.[93] However, it is also possible that the peaks are related to intrinsic transitions of different phases of TlBr. This possibility is discussed in Appendix A.

4.3.2 PL of TlBr:C

PL measurements were performed on 4 C-doped samples: #7, #8, #9, and #10. Initially, these samples were sent by RMD as cut from the boule with a wiresaw, without polishing or etching being done. However, after polishing was seen to make a difference with the PL measurements of the undoped crystals, the four samples were sent back to be polished and etched. PL spectra from the samples after polishing are shown in Figure 4.3. The spectra are dominated by the two intrinsic indirect and direct transitions. Only very faint defect luminescence centered around $\sim$1.9 eV is evident.

Figure 4.4 shows PL spectra from sample #7 measured before and after the sample was polished. In the spectrum taken with the sample unpolished, the peaks related to the

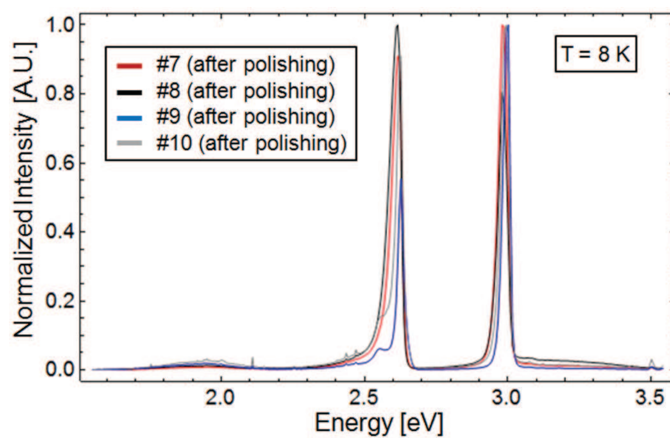

Figure 4.3: PL spectra from C-doped samples 7-10 after polishing.

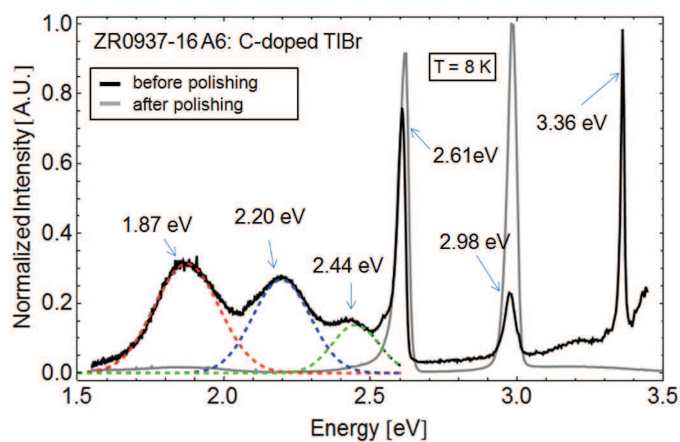

Figure 4.4: PL spectra from C-doped TlBr sample 7, measured before and after the sample was polished. The dashed lines show the result of fitting three Gaussian functions to the broad defect peaks visible over the range 1.5 eV to 2.5 eV.

intrinsic indirect and direct transitions are clearly visible at 2.61 eV and 2.98 eV respectively. In addition, three broader defect peaks centered at 1.87 eV, 2.20 eV, and 2.44 eV are visible. The peaks at 2.20 eV and 2.44 eV occur at similar energies for several defect peaks reported in the literature (see Section 4.1). All three of the defect peaks disappear upon polishing of the sample. Thus, it is possible that the defect peaks are related to mechanical damage in the material. Lastly, a sharp peak near 3.36 eV is evident in the unpolished C-doped sample spectrum, similar to those seen in the spectra from unpolished and nominally undoped TlBr samples. Once again, the possible origin of this peak is discussed in Appendix A.

4.3.3 Cathodoluminescence System Description

CL measurements were performed at the Naval Postgraduate School in the lab of Professor Nancy Haegel. A JEOL 840A scanning electron microscope was used for the measurements. Luminescence was collected with a parabolic mirror and dispersed with a 1/4 m grating monochromator. A cooled GaAs photomultiplier tube served as the detector, capable of detecting photons with energies down to 900 nm (1.4 eV). The samples were mounted to a cold finger with Apiezon N grease and were cooled with a continuous helium flow system. The electron beam energy used was 20 keV. Because of the high resistivity of the TlBr and charging effects, CL spectra were taken from an area of the sample 240 microns by 170 microns in size ($\sim$ 500x magnification) rather than the traditional spot mode. A description of the system has been published.[94]

4.4 Cathodoluminescence Results

4.4.1 CL of Nominally Undoped TlBr

CL data from three of the samples are shown in Figure 4.5. The two spectra from samples #3 and #5 not shown were identical to the spectra for samples #2 and #4. All three samples show peaks corresponding to the direct band gap of TlBr near 3.02 eV, and the indirect band gap near 2.7 eV, which have been reported previously.[78, 79, 80, 81, 82, 83, 84, 70, 64] The one polished sample, ZR43-62YD-A1, shows only a very broad and weak defect spectrum centered at 2.0 eV in addition to the two intrinsic transitions. The other two samples show broad peaks centered near 2.45 eV and 1.8 eV. In emission studies of TlBr, several groups have reported a broad band near 2.45 eV (see Section 4.1). The fact that it shows up clearly in the spectra from both unpolished samples but not the polished one suggests a possible relationship to sample preparation.

4.4.2 CL of TlBr:C

CL data from three of the C-doped samples (#7, #8, and #9) taken at 5 K are shown in Figure 4.6. Figure 4.7 shows the room temperature spectra for #8 and #10. At low

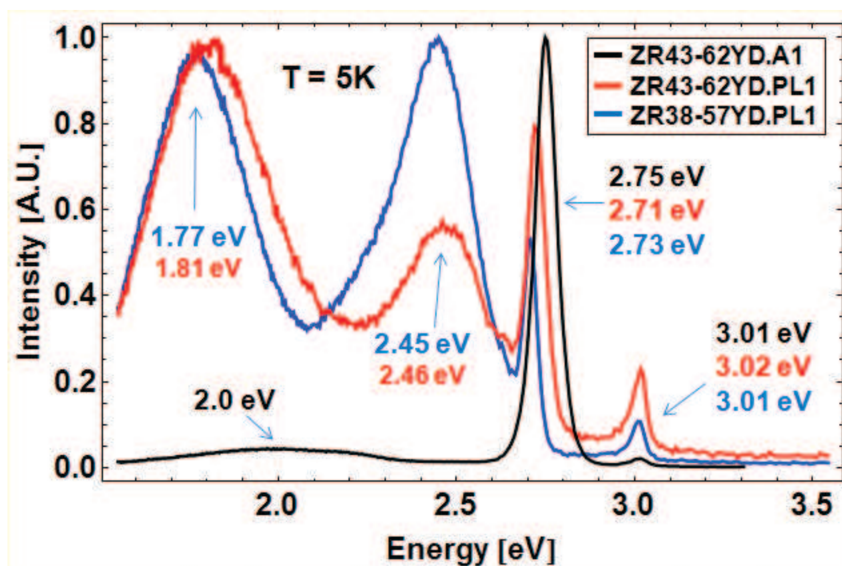

Figure 4.5: Cathodoluminescence spectra of 3 nominally undoped TlBr samples: #1, #2, and #4.

temperature, the peaks visible in the C-doped TlBr samples are the same as those visible in the spectra from the nominally undoped samples.

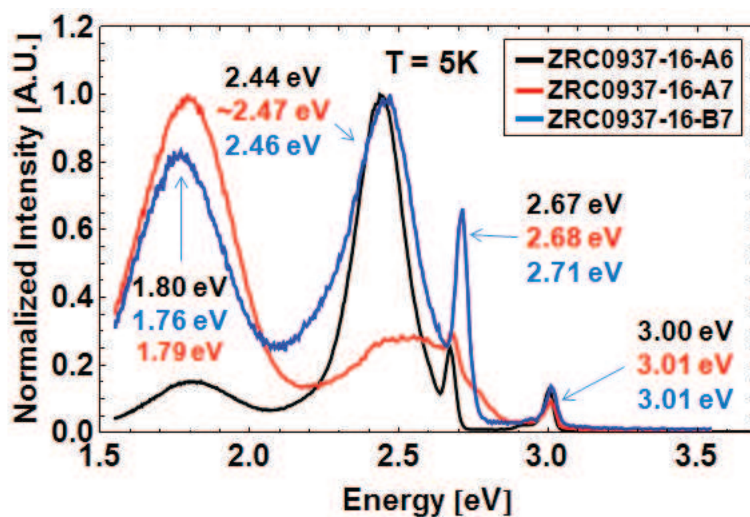

Figure 4.6: Cathodoluminescence spectra of 3 C-doped samples at T = 5K.

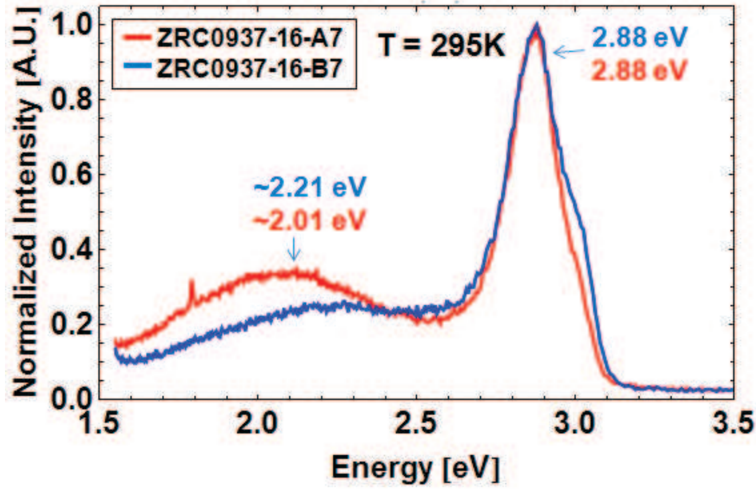

Figure 4.7: Cathodoluminescence spectra of 3 C-doped samples at room temperature.

4.4.3 CL of TlBr:O

The CL Spectra for the only O-doped TlBr sample measured (Sample #11) is shown in Figure 4.8. In comparison to C-doped or nominally undoped material, the defect peaks at 2.22 eV, 2.43 eV, and 1.80 eV are much larger than the intrinsic transition peaks at 2.67 eV and 3.01 eV. The peaks at 2.43 eV and 1.80 eV match up with CL peaks observed in the C-doped and nominally undoped materials as well. The peak at 2.22 eV does not appear in CL measurements of the other samples, but it is present in the PL spectrum of the C-doped sample shown in Figure 4.4.

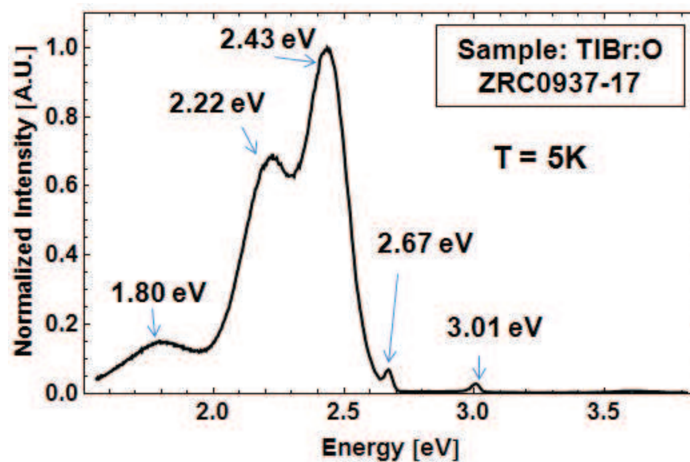

Figure 4.8: Cathodoluminescence spectra of an 0-doped sample at T=5K.

4.5 Comparison of PICTS and Luminescence Data

Table 4.2: Optically detected deep levels in nominally undoped, C-doped, and O-doped TlBr

Sample Type	Measurement	Peak Energy [eV]	$\Delta E_{indirect}$ [eV]	Sample(s) Found In
Nominally Undoped	PL	~1.75	~0.95	#6
	PL	~2.20	~0.5	#2 - #5
	PL	~2.42	~0.28	#2 - #5
	CL	~1.8	~0.90	#2 - #5
	CL	~2.0	~0.70	#1
	CL	~2.45	~0.25	#2 - #5
C-doped	PL	~1.87	~0.83	#7
	PL	~2.20	~0.50	#7
	PL	~2.44	~0.26	#7
	CL	~1.80	~0.90	#7- #10
	CL	~2.45	~0.25	#7- #10
O-doped	CL	~1.80	~0.90	#11
	CL	~2.22	~0.48	#11
	CL	~2.43	~0.27	#11

Table 4.2 summarizes the defect peaks detected with PL and CL measurements in the nominally undoped, C-doped, and O-doped TlBr samples. The values of energy at which these peaks appear are subtracted from the indirect band gap of TlBr (~2.70 eV at room temperature) in order to calculate the offset of the defect level from the band edge, which is labeled $\Delta E_{indirect}$ in the table. In this manner, the thermal transition levels measured in PICTS can be sensibly compared to the optical ionization energies measured with PL and CL.

The PL and CL spectra from nominally undoped TlBr show four peaks that are likely associated with defects. It can be seen that 3 of the 4 peaks have energies that are larger than any of the levels detected with PICTS. It is possible that these lower energy photons arise from transitions between traps, such as donor-pair recombination. Only the transition observed in CL corresponding to a defect level offset from the indirect band edge by ~0.25 eV is within the range of levels found with PICTS. Traps U7 and U8 found in the PICTS measurements both have similar activation energies of 0.26 eV, and could be related to the transition. Trap U8 seems more likely to be related considering that it appears in three of the nominally undoped samples, but was not detected in Sample #1. The CL spectrum from Sample #1 does not show the ~0.25 eV transition, in agreement with the PICTS results if the transition is due to Trap U8.

In optical data from the C-doped TlBr samples, three defect peaks are visible, though once again, only the 0.26 eV peak seen in both PL and CL measurements is shallow enough

to be correlated to a single transition level detected with PICTS. Traps C1$''$, C2, and C3$'$ all have suitably close activation energies to be associated with this transition. The optical peak at ∼2.44 eV looks the same in emission data from nominally undoped and C-doped TlBr, which suggests that it is possibly due to the same defect level. Additionally, traps C2 and U8 measured with PICTS are likely the same trap based on the similarity of their Arrhenius plots (see Section 3.5.1). Therefore, of the three candidates, trap C2 is the most likely to be associated with the optical transition at 2.44 eV.

The single trap detected with PICTS measurements in the O-doped TlBr sample does not appear to correspond well to any of the three observed defect peaks. However, the defect peaks observed with luminescence in O-doped material were also observed in C-doped and nominally undoped material.

4.6 Conclusion

Emission spectra using both laser and electron beam excitation have been presented for nominally undoped, C-doped, and O-doped TlBr in which several defect peaks are visible. The addition of C or O dopants does not appear to introduce optically detectable deep levels that are unique to the dopant. All defect peaks observed appear in all of the samples, though the relative magnitude of the defect peaks change with the sample. The condition of the surface of the sample affects PL measurements. PL spectra from unpolished samples of both nominally undoped and C-doped TlBr show three defect peaks, as well as sharp lumiscence peaks resembling intrinsic transitions above the direct band gap of TlBr in the CsCl phase. These features disappear or are greatly reduced upon polishing, suggesting a relationship between them and mechanical damage at the surface.

Chapter 5

Carrier Lifetime in Doped and Undoped TlBr

The goal of this chapter is to discuss the results of a method to characterize electrical transport in TlBr. The ambipolar carrier lifetime of both nominally undoped and doped TlBr was measured to assess the effects of dopants on lifetime in the material.

5.1 Introduction

As discussed in section 1.2.4, in order for a material to be considered a good candidate for room temperature radiation detection, the mobility-lifetime product of either electrons or holes in the material must be on the order of 10^{-3} cm$^2/V$. This requirement can be satisfied by materials representing two extremes - those with comparatively high mobility and short lifetimes, or those with comparatively low mobilities but long lifetimes. From the standpoint of energy resolution, any combination of properties that leads to a $\mu\tau$ greater than or equal to 10^{-3} cm$^2/V$ amounts to the same device performance. The individual magnitudes of the mobility and lifetime do affect the timing of the readout circuit of a detector however. The lower the mobility of the detector material, the more time is required to fully sweep generated charge out of the device. Therefore, detector applications involving high time resolution or high flux conditions are better satisfied by materials with high mobility. The mobilities of electrons and holes in CZT are about 1300 and 80 $cm^2/V \cdot s$, placing CZT in the category of high mobility resistive detectors.[8] By comparison, carrier mobilities in TlBr are approximately 25 $cm^2/V \cdot s$ for electrons and 2-20 $cm^2/V \cdot s$ for holes at room temperature[95, 96, 11]. Thus, TlBr is suitable for lower flux security applications.

5.1.1 Measuring the $\mu\tau$ product and mobility

A variety of methods exist to measure the $\mu\tau$ product of a detector. The most common way is to measure the charge collection efficiency of the detector as a function of bias. In this

technique, a resistive detector with contacts on two opposite sides (referred to as "sandwich geometry") is placed under a steady state bias. Alpha particles, x-rays, or strongly absorbing laser light with energy well above the bandgap of the material strike one side of the device near a contact, generating free carriers. Depending on the bias polarity, carriers of one type are quickly swept to the near contact, leaving carriers of the other type to flow through the bulk. The current that flows after carrier excitation is integrated to find the total charge collected after a strike. By knowing the electron-hole pair creation energy (see Section 1.2) of the material being tested and the energy of the incident alpha particle or laser pulse, the total charge generated can be calculated. Dividing the charge collected by the total charge generated yields the charge collection efficiency. In the single carrier case, the charge collection efficiency as a function of bias obeys a form of the Hecht equation given by:

$$Charge\ Collection\ Efficiency(V) = \frac{Q_{collected}(V)}{Q_{generated}} = \frac{\mu_{e,h}\tau_{e,h}V}{d^2}[1 - e^{\frac{d^2}{\mu_{e,h}\tau_{e,h}V}}] \tag{5.1}$$

In this equation, V is the applied bias, and d is the distance between the electrodes, corresponding to the device thickness. Fitting data taken at several values of applied bias to this equation yields the mobility-lifetime product.

With a time-resolved variation of the experiment described above, the transit time of the carriers through the device can be measured from the transient current shapes that result as generated charge is swept out of the device. The equation for the transit time is given by:

$$t_{transit} = \frac{d^2}{\mu_{e,h}V} \tag{5.2}$$

Once again, here V is the applied bias and d is the detector thickness. From the transit time, the mobility can be calculated. Thus, with a time resolved system, both the mobility-lifetime product, and mobility alone can be measured for both types of carriers. These are the two most widely-used techniques that have established the mobility-lifetime and mobility values published in literature for TlBr.[95, 16, 97, 11, 98, 99, 15]

5.1.2 Measuring carrier lifetimes

While carrier lifetimes can be calculated from mobility-lifetime products and mobilities, direct measurements of carrier lifetime in detector materials are less common. Lifetime can be measured with time-resolved luminescence studies if the material luminesces with sufficient intensity. Another powerful method to measure carrier lifetime that does not require radiative recombination is microwave photoconductivity decay transient analysis (MWPC). MWPC has many natural advantages that recommend it for detector characterization. As opposed to measurements involving Hecht analysis, MWPC measurements do not require contacts, and thus lifetime can be assessed without the difficulty of forming suitable ohmic contacts. Additionally, the analytical form of the Hecht equation relies on assumptions of

uniform transport characteristics throughout the entire volume of material being measured. It has been shown in both CZT and TlBr that charge transport in state-of-the-art crystals is strongly non-uniform spatially.[94, 27, 100] As discussed in section 1.3.2, non-uniformity of charge transport is the principle problem facing CZT growth. Thus, mobility-lifetime products measured with Hecht analysis and highly localized excitation sources such as alpha particles may be inadequately fit and show significant variation across a sample.

In an MWPC measurement, the material under study is placed at the end of a waveguide. Microwaves are directed toward the sample and transmitted and reflected in accordance with the dielectric function of the material. The transmitted or reflected microwave power is measured with a power meter. For simplicity, in this discussion it will be assumed that the reflected power is what is recorded, though a similar analysis applies to the case where transmitted power is recorded. The reflected power is first recorded before any perturbation of the dielectric function to establish a baseline. A short laser pulse is then used to generate free carriers in the material. Mobile free carriers are able to couple to microwave frequencies, and thus the absorption characteristics of a material in the microwave range will change when the concentrations of free carriers change. The change in the dielectric function due to the creation of mobile charge carriers dominates any other changes caused by the light pulse.[101] A typical resistivity for TlBr is 10^{10} $\Omega\cdot$cm, which corresponds to a background free carrier concentration of 10^{7} cm^{-3} at room temperature. A typical laser light pulse used in an MWPC experiment photogenerates free carriers concentrations on the order of $\sim 10^{20}$ cm^{-3} carriers (see Section 5.2.2 for an explicit calculation). Thus, the electronic contribution to the dielectric function of a resistive material changes dramatically under such conditions of photogeneration.

During the optical pulse, the reflected microwave power shows a sharp rise. At the end of the optical pulse, photo-generated carriers begin to recombine through several processes. In a semiconductor, carriers recombine across the band, via Auger recombination, and at traps and surfaces. As the free carrier concentrations diminish, the reflected microwave power decays with time constants reflecting the recombination processes in the material. By selecting appropriate excitation conditions and sample preparation, different processes can be emphasized.

5.1.3 MWPC as a tool to assess the relative quality of TlBr samples

With TlBr, it is desirable to know the ambipolar carrier lifetime of the material in the bulk. Given the indirect band gap of TlBr and the low background free carrier concentration, trap-assisted recombination is expected to be the dominant recombination pathway for free carriers. A sample with a higher ambipolar carrier lifetime relative to another is likely to have less traps, and is therefore of better quality from a device standpoint. The excitation wavelength and intensity in an MWPC measurement can be chosen so that carriers are generated close to the surface or uniformly throughout the bulk. In the first case,

surface recombination processes are expected to dominate the reflected power transient, and the measurement can give an indication of surface quality. In the second case, the surface component is also present but small relative to the signal from the volume, and the measurement gives an indication of bulk quality. Thus, both relative surface and bulk material quality can be assessed with MWPC measurements.

In a measurement involving uniform bulk excitation, it is difficult to separate out definitively each process affecting the population of free carriers. Even in cases where trap-assisted recombination is assumed to be dominant, there can still be many traps with characteristic trapping and detrapping times leading to complicated photoconductivity decay transients composed of several time constants. Therefore, the decay time that is measured in an MWPC experiment, while useful to discriminate between samples, must be cautiously interpreted.[102]

5.2 Experimental

5.2.1 Samples measured

Nominally-undoped and doped TlBr samples were measured with MWPC. The nominally undoped, C-doped, and O-doped samples were the same ones measured with PL and CL, and described in Section 4.2.1. Pb- and Se-doped samples were also measured. Growth and preparation details of the Pb- and Se-doped samples are given in Section 6.2.1.

5.2.2 Experiment Description

MWPC measurements were performed at the Joint Center for Artificial Photosynthesis, in the lab of Dr. Ian Sharp. The excitation source was a Nd:YAG laser pulsed at 3-5 ns with a repetition rate of 10 Hz. Depending on the experiment, the excitation wavelength was selected between 355 nm (3.49 eV, above bandgap) and 532 nm (2.33 eV, below bandgap), and the power adjusted with an attenuator over the range from 280 microjoules to 1.8 millijoules per pulse. Data were recorded using both below bandgap and above bandgap excitation to measure surface and bulk recombination processes. Lenses were used to focus the laser spot size on the sample to approximately 1 mm^2. Microwaves with a frequency of 38.3 GHz were generated with a Gunn diode oscillator. The microwaves were directed to the sample, which was placed at the end of an open waveguide. The reflected microwave power was measured with a Schottky diode finline detector and recorded with a 10 GHz Keithley oscilloscope.

In the case of above bandgap excitation at 355 nm (3.49 eV), the laser light was absorbed very close to the surface of the sample. The number of free carriers photogenerated by the light can be approximately calculated. The generation rate of free carriers as a function of depth in a material under optical excitation is given by:

$$G(x) = (1 - R)\alpha(h\nu)\Phi_o exp[-\alpha(h\nu)x] \quad (5.3)$$

In this equation, R is the surface reflectivity, α is the absorption coefficient, Φ_o is the incident photon flux, and x is the distance into the material from the illuminated surface. [42] The lowest excitation power used during all experiments was 280 microjoules per ∼3 nanosecond pulse, focused into a 1 mm^2 spot. At an excitation wavelength of 355 nm, the corresponding photon flux is $1.78 \times 10^{25} cm^{-2}s^{-1}$. The absorption coefficient of TlBr at 3.49 eV is $\sim 10^5$ cm^{-1}.[77] The surface reflectivity can be conservatively estimated to be 0.5, though is likely much lower. Integrating the generation rate from 0 to 500 microns, a typical sample thickness, and multiplying by the pulse duration yields a concentration of 2.68×10^{20} cm^{-3} free carriers (see Appendix C for the full calculation). Such a concentration is ∼13 orders of magnitude above the background free carrier concentration in TlBr, ensuring a strong transient reflected microwave power signal.

The number of photogenerated carriers in the case of sub-bandgap excitation at 2.33 eV is more difficult to estimate. Aside from the two-photon absorption process observed in cases of high incident intensity, the photogeneration of free carriers with sub-bandgap light requires mid-gap states. The absorption coefficient of TlBr in this range thus depends strongly on extrinsic features of the individual samples, and is not reported in literature. Even assuming the absorption coefficient to be 5 orders of magnitude lower than it is at 3.49 eV however, which is reasonable compared to reported sub-bandgap absorption coefficients in other wide bandgap semiconductors such as GaN, electron-hole pairs are generated in concentrations on the order of 10^{20} cm^{-3} as well.[103] Thus, the reflected microwave power signal is strong in both cases.

5.3 Results and Discussion

5.3.1 Nominally Undoped TlBr

The results of applying MWPC measurements to 3 undoped TlBr samples using sub-bandgap light are shown in Figure 5.2. It was found that the data were better fit with a double as opposed to a single exponential function. The orders of magnitude of the two time constants extracted from the fits are the same for all three samples. It is presumed that the fast component of the measured signal relates to the recombination of carriers generated near surfaces, whereas the slower component relates to recombination processes in the bulk. The time constants of the slower component of the signals have the correct order of magnitude required to interpret them as the bulk lifetime. Measured carrier mobilities in TlBr are on the order of 10 cm$^2/(V \cdot s)$, and measured mobility-lifetime products on the order of 10^{-3} cm$^2/V$ for electrons and 10^{-3}-10^{-4} cm^2/V for holes, requiring that carrier lifetimes be on the order of 10^{-4} s. This is exactly the order of the time constants obtained from the fit of the MWPC data.

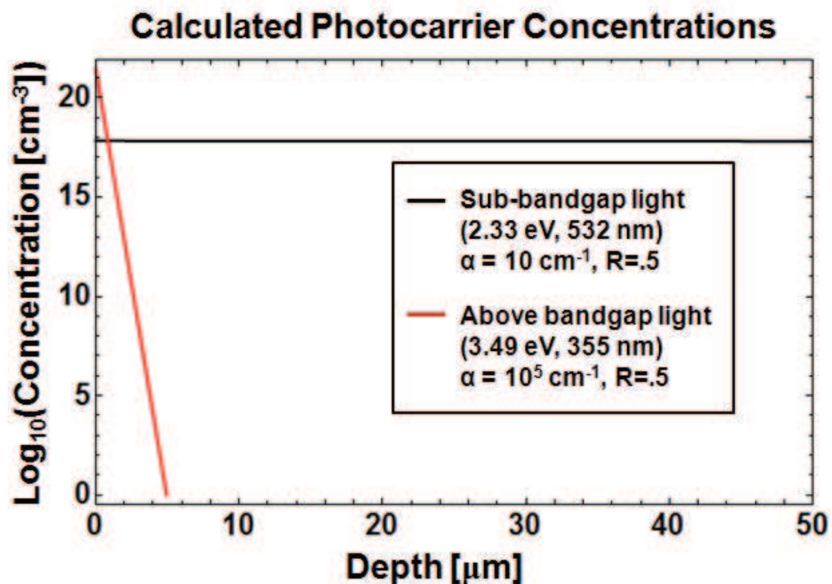

Figure 5.1: The calculated volume of free carriers generated by the laser light in an MWPC experiment as a function of depth in the case of above- and sub-bandgap excitation, plotted on a log scale. Despite the sharp difference in the depth profile of where the carriers are generated, integrating the expressions and multiplying by the illuminated volume yields total photogenerated carrier numbers on the order of $\sim 10^{12}$ in both cases, many orders of magnitude above the number of thermally generated free carriers in the same volume in TlBr at room temperature. (See Appendix C for complete calculations.)

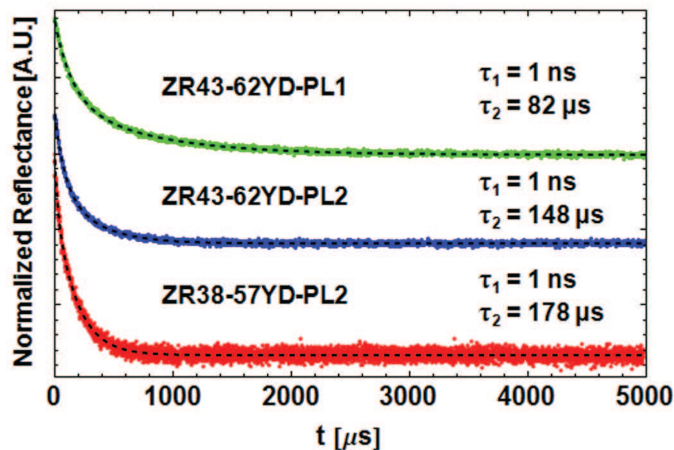

Figure 5.2: Reflected microwave power transients for 3 nominally undoped samples using 532 nm excitation (2.33 eV). The transients have been normalized and offset for clarity. The dashed lines show the result of a double exponential fit to the data. The laser power used was 280 μJ per $\sim$3 ns pulse, which is $\sim$ 93.3 kW.

Figure 5.3 shows the results of MWPC measurements taken with above bandgap light. In this case, carriers are generated very close to the surface of the TlBr samples (see Figure 5.1). Once again, double exponential functions were found to better fit the data than single exponential functions, but the underlying physics and interpretation of the numbers are not as clear as in the above bandgap case. The difficulties of simply fitting MWPC data in the regime of above bandgap excitation have been reported.[104, 105] The transient is complicated by the fact that the surface recombination velocity depends on carrier concentrations, which vary with time as carriers recombine. Additionally, spatial variations of the electric field modify the contribution of free carriers in different parts of the sample to the reflected microwave power signal. Thus, both recombination rates and the reflectivity signal itself depend strongly on the spatial variation and concentrations of photo-generated free carriers. The carrier kinetics are too complicated to yield a simple analytic form to expect from the microwave reflectivity.

Though not easy to interpret definitively, the results from the above-bandgap excitation do show that carriers recombine much faster in the case of near-surface generation than in the case of uniform bulk generation, which is to be expected in a material known to have a long bulk lifetime. Furthermore, comparing the signal from different samples gives some indication of the quality of the surface of the sample. The majority of TlBr samples measured with MWPC in this work were unpolished and likely had strongly mechanically damaged surfaces, making such a study unilluminating. However, specially prepared samples with different surface finishes could provide the starting point for a fruitful study of surface treatment techniques for TlBr samples.

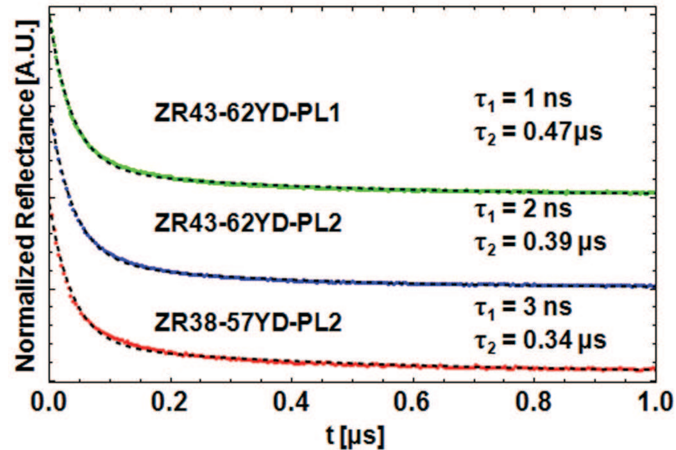

Figure 5.3: Reflected microwave power transients for 3 nominally undoped samples using 355 nm excitation (3.49 eV). The transients have been normalized and offset for clarity. The dashed lines show the result of a double exponential fit to the data. The laser power used was 280 μJ per ∼3 ns pulse, which is ∼ 93.3 kW.

5.3.2 TlBr:O, TlBr:Pb, TlBr:Se

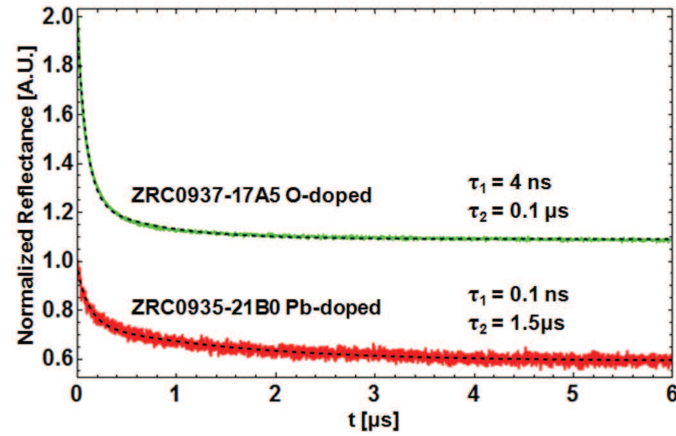

Figure 5.4: Reflected microwave power transients for one Pb-doped and one O-doped TlBr sample using 532 nm excitation (2.33 eV). The transients have been normalized and offset for clarity. The dashed lines show the result of a double exponential fit to the data. The laser power used was 300 μJ per ∼3 ns pulse, which is ∼ 100 kW.

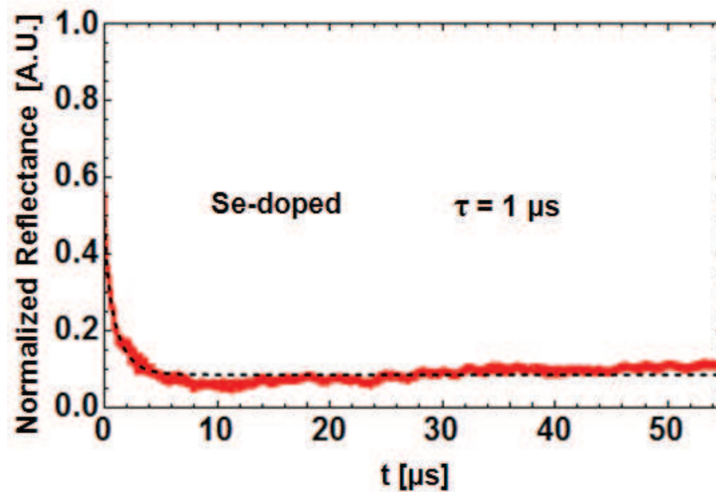

Figure 5.5: Reflected microwave power transients for one Se-doped TlBr sample using 532 nm excitation (2.33 eV). The transient has been normalized. The dashed lines show the result of a single exponential fit to the data. The laser power used was 2 mJ per ∼3 ns pulse, which is ∼0.66 MJ.

The results of MWPC measurements using sub-bandgap excitation (2.33 eV) on three TlBr samples doped with Pb, O, and Se are shown in Figures 5.4 and 5.5. The laser power

used was the same for the Pb and O samples. The Se-doped TlBr sample required a higher laser power in order to generate an MWPC signal of sufficient strength to measure, and is hence plotted separately. This can be explained by the different efficiencies of the excitation process in each sample in the regime below intrinsic absorption, owing to differences in mid-gap state concentrations and kinetics. Even at a higher laser power, the Se-doped sample's signal-to-noise ratio was lower than that of the Pb- or O-doped samples. In this case, a single exponential fit was found preferable to a double exponential, which seemed to fit features of the noisy background.

It can be seen that the calculated time constants in each of the three doped samples are much lower than those measured with undoped samples. The O-doped sample has the best lifetime of the three, but it is an order of magnitude lower than those of the undoped samples. The Pb and Se-doped materials are closer to two orders of magnitude lower in bulk lifetime. An MWPC measurement alone cannot determine the mechanism by which a dopant lowers lifetime, whether by introducing recombination centers or structural deformation or precipitates and extended defects. However, from the data it is possible to say that the TlBr samples doped with Pb, O, and Se have significantly lower lifetimes than the measured undoped TlBr samples. It is thus likely that Pb, O, and Se dopants have detrimental affects on carrier lifetimes in TlBr.

5.3.3 TlBr:C

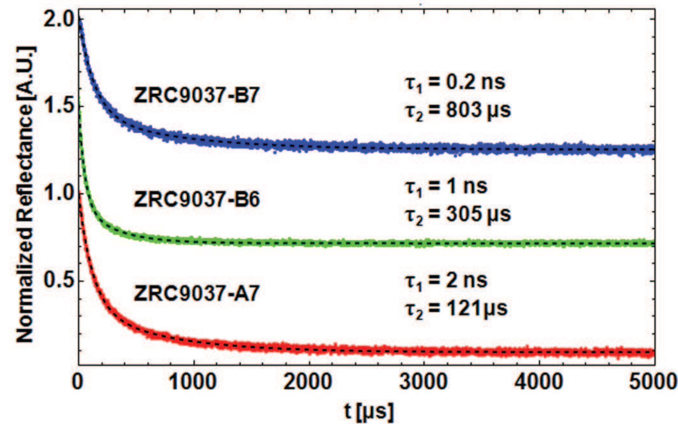

Figure 5.6: Reflected microwave power transients for 3 C-doped TlBr samples using 532 nm excitation (2.33 eV). The transients have been normalized and offset for clarity. The dashed lines show the result of a double exponential fit to the data. The laser power used was 280 μJ per ∼3 ns pulse, which is ∼93.3 kW.

It might seem that any dopant, being a point defect and imperfection in the lattice, would likely lower carrier lifetimes in a semiconductor. This is not always true. As an example, small elements such as lithium have been used to passivate electrically activate

defects in detector materials to increase carrier lifetimes.[4] Figure 5.6 shows the results of MWPC measurements on three C-doped TlBr samples in the case of sub-bandgap excitation. Remarkably, the calculated time constants do not show reductions from those of the undoped samples. Two of the samples appear to show an even longer lifetime compared to undoped samples. This initial result is interesting, but much more experimental work is required to explore the role of carbon in TlBr. It is not known where the carbon sits in the lattice, or what effect it could have electrically to influence carrier lifetimes.

5.4 Conclusion

Table 5.1: Summary of Measured Lifetimes in Nominally Undoped and Doped TlBr Samples

Sample Name	Dopant	Approximate Lifetime [μs]
ZR43-62YD-PL1	-	82
ZR43-62YD-PL2	-	148
ZR38-57YD-PL2	-	178
ZRC0937-A7	C	121
ZRC0937-B6	C	305
ZRC0937-B7	C	803
ZRC0937-17-A5	O	0.10
ZRC0935-21-B0	Pb	1.5
VBD03	Pb	0.30
VBD01	Se	1.0

A selection of nominally undoped TlBr samples were characterized with MWPC measurements in both above-bandgap and below-bandgap excitation regimes. In the case of below-bandgap excitation, an assumption of uniform bulk-absorption was made to interpret the observed transients as consisting of a fast component due to surface recombination, and a slow component related to recombination processes in the bulk. By interpreting the slow component of the microwave transients as the bulk lifetime, reasonable values were measured that agree with separate measurements of the mobility-lifetime product and the mobility in TlBr. MWPC measurements are thus shown to be a simple and effective way to evaluate the quality of bulk material without applying contacts. The case of above-bandgap excitation is also discussed briefly, but the samples used in this study had unpolished surfaces with remnant mechanical damage, making relative assessments of surface quality unimportant.

MWPC measurements in the sub-bandgap excitation regime were made to evaluate the effects of Pb, Se, O, and C-dopants on the bulk lifetime in TlBr. It was found that Pb, Se, and O-doped materials have dramatically lower carrier lifetimes by one to two orders of magnitude. In contrast, C-doped TlBr samples were found to have comparable or longer lifetimes compared to those of the undoped samples. Further experimental study is required

in the case of each dopant to determine the exact mechanism by which the lifetime is increased or decreased.

Chapter 6

Dopant Mitigation of Ionic Conductivity in TlBr

In this chapter, techniques introduced in the previous chapters are applied in concert to Pb- and Se-doped TlBr. The motivation for doping TlBr with Pb and Se is explained in the context of ionic conductivity in TlBr.

6.1 Background and theory

One of the principal challenges facing TlBr is the strongly ionic character of the crystal. It has been shown that TlBr exhibits ionic conduction at room temperature, which is a significant problem for detector performance. Ionic conductivity contributes to the leakage current and leads to the degradation of a TlBr device over time. The effect of ionic conduction on device performance can be understood as follows: when a bias is applied to the material, ions drift and build up an internal electric field that opposes the direction of the applied bias - a phenomenon known as polarization. Radiation detectors are typically operated at high bias (several hundred V/cm or higher) to ensure complete charge collection from an ionizing event. A TlBr detector that polarizes in such conditions will lose sensitivity over time, as the charge collection efficiency degrades with the increasing strength of the internal ionic field. In 2004, Vaitkus et al. proved this polarization experimentally by first applying a bias of 600V to a TlBr detector for several hours, and then reducing the bias to 30V. The dark current flowing through the device switched sign even though the applied bias did not, proving the presence of the reverse electric field caused by drifted ions.[106] Many later studies found similar results, often with notes reaffirming the importance of the problem.[107, 108, 109] Though the pace of degradation differs between samples, it is on the order of tens of hours to a couple of days between a state of successful operation and a state of complete degradation such that no useful signal can be obtained from the device, at room temperature.

The question of whether ionic conductivity can be mitigated or reduced is important for the commercial adaptation of TlBr as a detector material. In order to tackle the problem, the

mechanisms underlying the conductivity must be understood. The results of temperature-dependent impedance spectroscopy studies of TlBr at room temperature and above have been fit very well to a model of ionic conductivity that considers only mobile Tl and Br vacancies in the material.[38, 39, 40, 41] In this model, the ionic conductivity of TlBr at room temperature is given by:

$$\sigma_{total} = \sum_i |z_i| e[i] \mu_i = q[V_{Tl}^{/}]\mu_{V_{Tl}} + q[V_{Br}^{\cdot}]\mu_{V_{Br}} \tag{6.1}$$

Here, $[V_{Tl}^{/}]$ and $[V_{Br}^{\cdot}]$ are the Tl and Br vacancy concentrations (with the charge state expressed in Kröger-Vink notation, indicating that the Tl vacancy has a singular negative charge, and the Br vacancy has a singular positive charge), q is the electron charge, and $\mu_{V_{Tl}}$ and $\mu_{V_{Br}}$ are the respective vacancy mobilities. In a crystal free of all extrinsic defects, the concentrations of Tl and Br vacancies would be equal in order to satisfy the condition of charge neutrality. The Br vacancy mobility, though strongly temperature dependent, is experimentally found to be much higher than the Tl vacancy mobility at room temperature and above. Therefore, in a crystal with only intrinsic defects, the largest contribution to the ionic conductivity at room temperature comes from the concentration of Br vacancies. If it were possible to somehow lower the concentration of Br vacancies, the ionic conductivity would decrease.

One promising approach to lower ionic conductivity in TlBr has been to dope the material with ionic donors or acceptors, which change the concentrations of vacancies present in the material. From the standpoint of charge neutrality, doping TlBr with a donor atom with an extra electron allows a positively charged vacancy to exist. Alternatively, doping TlBr with an acceptor atom allows a negatively charged vacancy to exist in the material. The charge neutrality conditions can be expressed with the following relations:

In the case of no dopants:

$$[V_{Br}^{\cdot}] = [V_{Tl}^{/}] \tag{6.2}$$

“Donor”-doped:

$$[V_{Br}^{\cdot}] + [D_{Tl}^{\cdot}] = [V_{Tl}^{/}] \tag{6.3}$$

“Acceptor”-doped:

$$[V_{Br}^{\cdot}] = [V_{Tl}^{/}] + [A_{Br}^{/}] \tag{6.4}$$

Here $[D_{Tl}^{\cdot}]$ denotes the concentration of “donor” atoms sitting on a Tl site, and $[A_{Br}^{/}]$ denotes the concentration of “acceptor” atoms siting on a Br site. As an example, Pb has one more electron than Tl, and thus Pb on a Tl site acts as a donor. Se has one less electron than Br, and thus Se on a Br site acts as an acceptor. By doping TlBr with either Pb or Se, the concentrations of Tl and Br vacancies can be modified. Figure 6.1 illustrates the principal of charge neutrality doping.

Doping TlBr with donor Pb and acceptor Se dopants is expected to pin the concentration of Br and Tl vacancies respectively, allowing control over the dominant ionic conductivity charge carrier in extrinsic regimes. It has been calculated that doping TlBr to have a

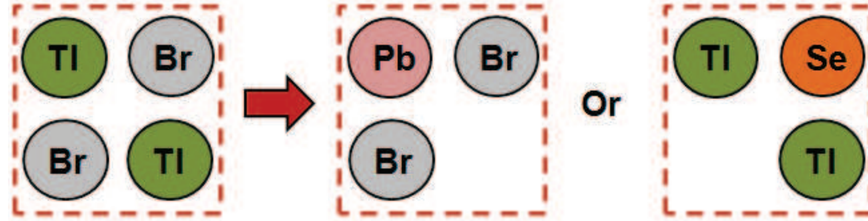

Figure 6.1: A cartoon showing three charge-neutral TlBr unit cells. In the first cell, the number of Tl atoms equals the number of Br atoms. In the second cell, Pb, which has one more electron than Tl, sits on a Tl site. In the third cell, Se, which has one less electron than Br, sits on a Br site. The addition of a Pb atom can be thought of as allowing a Tl vacancy to exist, whereas the addition of an Se atom allows a Br vacancy to exist.

residual donor concentration of 4 ppm will minimize the dark ionic conductivity of TlBr at room temperature.[26] Introducing dopants however has the potential to create deep level states in the band gap, which in turn can detrimentally affect carrier lifetimes and transport. Thus, TlBr poses an intriguing challenge of materials engineering: is it possible to mitigate the ionic conduction of TlBr without harming the excellent electronic transport properties?

Any strategy for doping TlBr must be evaluated for its effects on both the ionic and the electronic conductivity. There are currently very few studies on electronic effects of donor and acceptor dopants in TlBr, and none with specific deep level detection or attribution. The goal of this chapter is to elucidate the electronic effects of Pb and Se in TlBr by studying mid-gap levels potentially related to the dopants.

6.2 Experimental

6.2.1 Samples Used

Pb- and Se-doped TlBr samples were provided by Radiation Monitoring Devices, Inc. In contrast to all other samples presented in this dissertation that were grown by the TMZ method, the Pb- and Se-doped crystals were grown by the Vertical Bridgman method and nominally doped with 100 ppm Tl_2Se and 100 ppm $PbBr_2$ respectively. A 300-micron thick sample was cut from each crystal with a wire saw, and then lapped and polished. Glow Discharge Mass Spectroscopy (GDMS) was performed on the doped samples and the concentrations found to be 450 ppm wt Pb and 100 ppm wt Se respectively. The other dominant impurity in both doped samples was Cl, with a concentration of 15 ppm wt. All other impurities detected had concentrations less than 1.2 ppm wt. For PICTS measurements, contacts were deposited and the samples were mounted to sapphire substrates in the manner described in Section 3.3.1. The undoped sample used as a reference in this chapter is ZR43-62.YD-A1, whose preparation is also described in that section.

6.2.2 Measurement Details

The experimental details of the PICTS measurements are described in Section 3.2. As explained previously, only the temperature range 80-250 K was scanned in order to avoid ionic conduction effects and polarization. Details of the MWPC measurements are reported in chapter 5.2.2. Cathodoluminescence experimental details are described in 4.3.3.

6.3 Results and Discussion

6.3.1 PICTS on Pb- and Se-doped TlBr

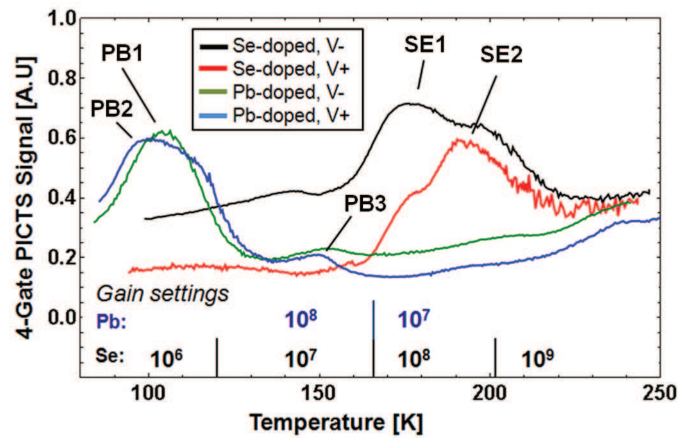

Figure 6.2: Four-gate PICTS spectra for Pb-doped and Se-doped TlBr, measured from 90-250 K for $e_{n,p}$=585 s^{-1}. V+ and V- denote the sign of the voltage applied to the illuminated contact. The gain settings of the current amplifier during the measurement indicate the change in photoconductivity of each sample with temperature.

Figure 6.2 shows PICTS spectra for the two doped TlBr crystals obtained using 4-gate PICTS analysis (see 2.2.2). The polarity of the bias applied to the illuminated top contact is noted for each spectrum. Clearly discernible peaks for which deep level parameters could be calculated are labeled. Figure 6.3 shows the Arrhenius plots for the detected traps, which yield the trap parameters summarized in Table 6.1. In order to calculate the apparent capture cross sections for the detected traps, the nature of the trap must be known. The values reported are based on determinations of trap type from the bias polarity, using the effective masses of electrons and holes found in literature.[77]

6.3.2 CL on Pb- and Se-doped TlBr

Figure 6.4 shows the results of the CL measurements. All three spectra feature peaks related to intrinsic transitions near 3.02 eV and 2.7 eV, as discussed in Chapter 4. The un-

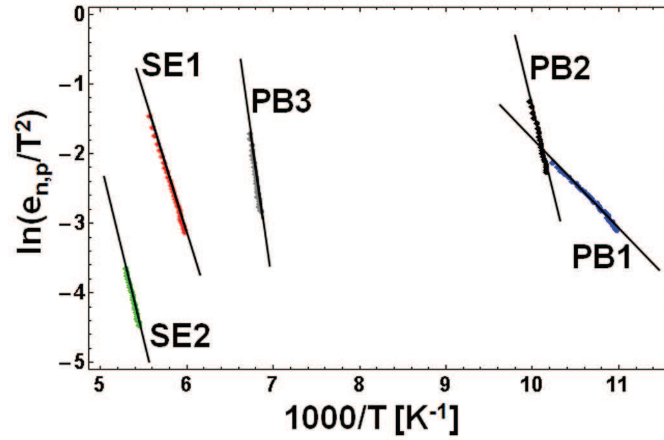

Figure 6.3: Arrhenius plots for the observed levels, showing data points and the resulting linear fits. The slope of the lines represents the activation energy of each trap. The apparent capture cross section is determined from the y-intercept.

Table 6.1: PICTS results for Pb- and Se-doped TlBr

Peak	Sample Dopant	$E_{activation}$ [eV]	Capture Cross Section [cm^2]	Tentative trap type
SE1	Se	0.35	1.9 x 10^{-12}	electron
SE2	Se	0.45	6.6 x 10^{-12}	hole
PB1	Pb	0.11	1.1 x 10^{-16}	electron
PB2	Pb	0.45	3.9*	hole
PB3	Pb	0.75	2.4 x 10^{3}*	hole

* Asterisks denote unphysically large capture cross sections.

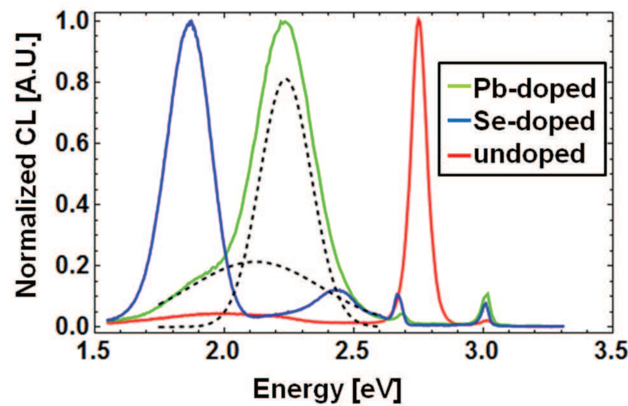

Figure 6.4: CL spectra for the TlBr samples taken at 5K. The dashed lines show a deconvolution of the two peaks evident in the Pb-doped spectrum between 1.8 and 2.5 eV.

doped sample shows no additional peaks in the measured range. Table 6.2 gives a numerical summary comparing the peaks found with PICTS and CL.

6.3.3 Comparison of PICTS and CL

The Se-doped TlBr PICTS spectra show two well-resolved peaks with excellent linear agreement in Arrhenius plots. Though both peaks are visible in the two spectra, Peak SE1 is more clearly resolved in the case where the top contact is negatively biased and primarily electron current flows through the bulk, whereas Peak SE2 shows up more clearly when the top contact is positively biased. This indicates that Peak SE1 is likely due to an electron trap, and Peak SE2 is due to a hole trap. Assuming that Peak SE1 and Peak SE2 are electron and hole traps respectively, the 1.86 eV peak (red, $\lambda = 667$ nm) seen with CL matches with recombination for an exciton involving electrons and holes trapped at these levels. Such radiative recombination involving deep donor-acceptor pairs is well established in indirect gap materials, such as GaP.[110, 111] The 2.43 eV (green, $\lambda = 510$ nm) luminescence observed with CL does not correspond to any traps identified with PICTS.

The Pb-doped sample yielded three resolvable PICTS peaks. Based on polarity assessments, Peak PB1 is likely due to an electron trap, while Peaks PB2 and PB3 are due to hole traps. The yellow emission (2.12 eV, $\lambda = 585$ nm) corresponds well to a transition between the PICTS traps identified as Peaks PB1 and PB2. The strongest luminescence at 2.23 eV matches with a band-edge to defect transition involving the 0.45 eV hole trap.

Figure 6.5 shows the Arrhenius plots of traps discovered in Pb- and Se-doped material compared to those found in all the other nominally undoped, C-doped, and O-doped TlBr samples included in this dissertation. It can be concluded from these plots that most of the discovered traps appear to be unique to the sample. Only Trap SE1 bears strong resemblance to the C3$''$ and U5 traps discovered in C-doped and nominally undoped TlBr respectively. Traps SE2 and PB3 stand out quite uniquely. PB1 and PB2 reside in the same vicinity as Trap U2, but have markedly different slopes and activation energies. It is thus possible that several of the observed traps are unique to the Pb- and Se-dopants. This is in contrast to all of the levels except for one found in C-doped TlBr, and the one level found in O-doped TlBr, which were also present in nominally undoped samples. However, it is also important to point out that the Pb- and Se-doped samples were grown by the vertical Bridgman as opposed to the traveling molten zone method. Different growth techniques can affect the populations of native defects present in a material, as well as the amount of mechanical defects and the dislocation density in the material.

Peaks PB2 and PB3 give reasonable energy values with good fits in Arrhenius plots, and yet both yield unphysically high capture cross sections. Similar behavior has been reported and attributed to the simultaneous emission of carriers from many traps and to strong photocurrent variations during carrier recombination.[58] There are several additional difficulties that may account for the anomalous cross sections. Peak PB2 is obscured by the presence of Peak PB1. They appear close in the spectra, though it is clear they are two different levels given the large difference in activation energy and the dependence on bias

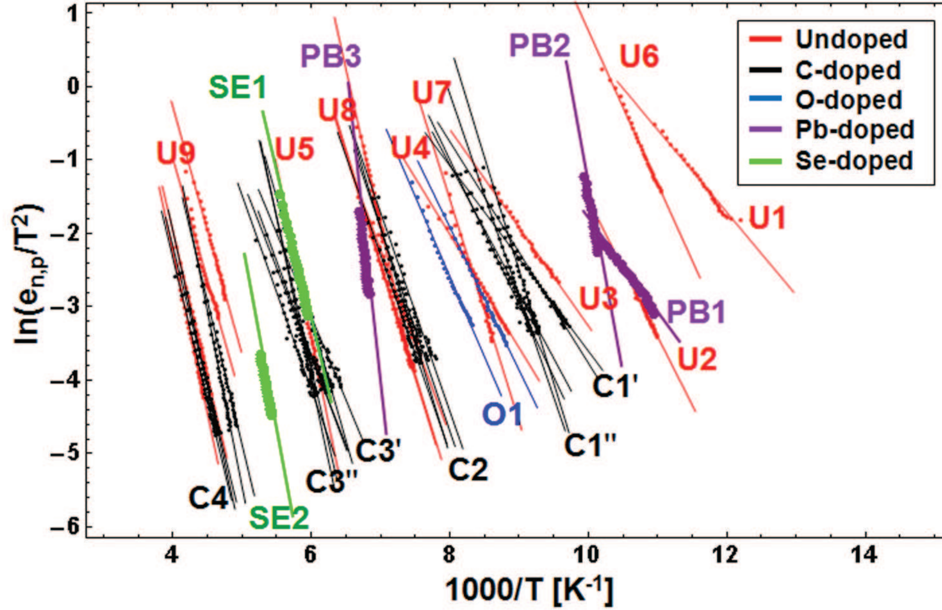

Figure 6.5: Arrhenius plots of traps discovered in Pb- and Se-doped material, compared to those found in nominally undoped, C-doped, and O-doped TlBr reported in Chapter 3. The Pb-doped and Se-doped traps are shown with enlarged plots markers for emphasis.

polarity. Peak PB2 does not stand out in the case of positive bias as much as Peak PB1 does for negative bias, and the fit for PB1 is correspondingly better. Peak PB3 is not as well defined as the other peaks in the samples. Over a large enough time window, the height and width of Peak PB3 changes significantly, indicating a strong deviation of the underlying current transient from single exponential behavior. The broadening is characteristic of the type discussed in section 3.3.3), and likely indicates the effect of mechanical damage and imperfections on the defect transitions.

Table 6.2: Comparison of PICTS and CL Results for TlBr:Pb and TlBr:Se

Dopant	CL [eV]	$\Delta E_{indirect}$	PICTS [eV]
Se	2.43	0.25	-
Se	1.86	0.82	0.35 (A) + 0.45 (B)
Pb	2.23	0.45	0.45 (D)
Pb	2.12	0.56	0.45 (D) + 0.11(C)
Pb	-	-	0.75 (E)

6.3.4 MWPC on Pb- and Se-doped TlBr

Figure 6.6 shows the results of the lifetime measurements. For the sake of simplest comparison, the transients were fitted to a single exponential. Photogeneration of free carriers with sub-bandgap light requires mid-gap states, which are present in the samples in different concentrations. Therefore different laser powers were used to generate transients of comparable magnitude, reflecting the different efficiencies of the excitation process in each sample. The lifetimes of both the Se-doped and Pb-doped samples were found to be more than an order of magnitude lower than in the undoped sample.

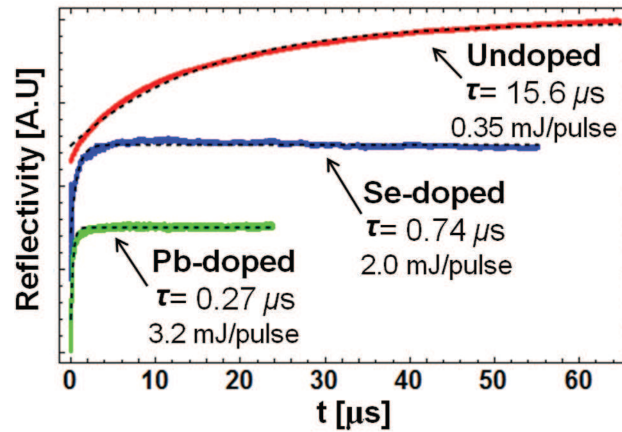

Figure 6.6: Plots of microwave photoconductivity transient data with single exponential fits (black dashed lines) showing the ambipolar lifetime in the three TlBr samples. The different laser powers used reflect the differing efficiencies of carrier generation with sub-bandgap light in the three samples. The curves are vertically offset for clarify.

6.3.5 Forming the Picture of Mid-Gap States

By comparing the optical emission and PICTS data, it is possible to construct a picture of mid-gap states in Pb- and Se-doped TlBr. The result of doing so is shown in Figure 6.7.

6.4 Conclusion and Future Outlook

In summary, the first tentative band picture assigning mid-gap states to specific dopant-related deep levels in TlBr has been achieved by correlating data from PICTS and CL measurements (see Figure 6.7). The presence of deep levels in both doped samples show a pronounced effect on the ambipolar carrier lifetime measured at room temperature. Carrier lifetimes in both the Pb- and Se-doped samples were dramatically lower than in the undoped samples, suggesting that Pb-doping and Se-doping has deleterious consequences for charge transport in TlBr.

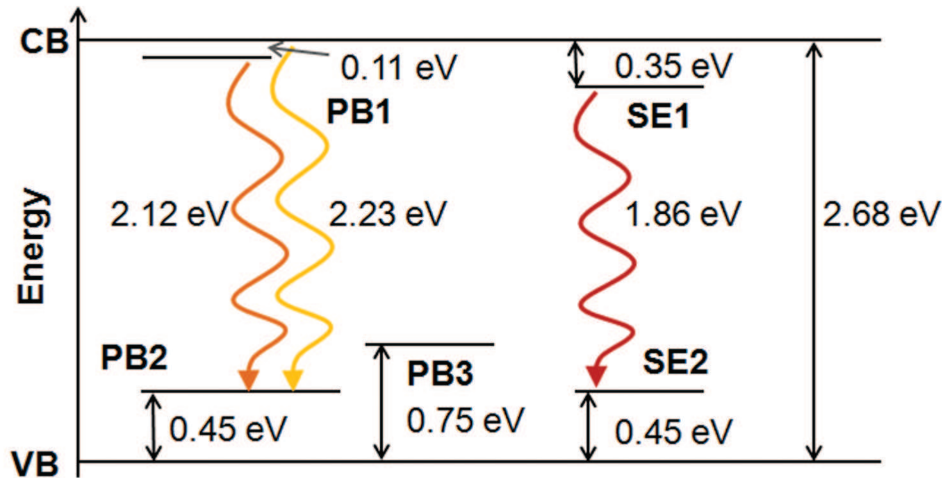

Figure 6.7: A schematic energy level diagram showing mid-gap states related to Pb- and Se-dopants in TlBr detected by PICTS. Curved arrows indicate optically active transitions measured with CL.

The present work does not conclusively prove that the deep levels detected are due to defect states introduced by the dopants. The defects in the doped samples could arise from other effects of the doping process, structural defects owing to the dopants, dopant clusters, and many other possibilities. Further experimental work is required to conclusively identify the level detected with PICTS and CL. It should be noted that a recent first-principles calculations paper predicts that Pb and Se *should not* form deep levels within the bandgap of TlBr.[73] If this paper is correct, then many of the explanations enumerated above could explain the experimentally observed deep levels in Pb- and Se-doped TlBr, as well as the reduced charge transport compared to undoped material.

Productive deep-level doping of a unique ionic material like TlBr must balance the beneficial effects of ionic conductivity mitigation and possibly Fermi level pinning with the detrimental effects of reduced mobility and lifetime. Unfortunately, in the case of Pb- and Se-dopants in particular, the electronic conductivity appears to be greatly reduced. It is hoped that other dopants may prove more suitable. The effectiveness of using deep-level, optical and lifetime measurements to identify the effects of dopants has been demonstrated, with the goal of improving the doping and device potential of TlBr.

Chapter 7

Conclusions and Future Work

The electrical and optical detection of deep levels presented in this dissertation are the first systematic studies of their kind on state-of-the-art detector-grade TlBr. The successful application of PICTS to TlBr has demonstrated that the kinds of studies that lead to the improvement of deep level engineering in CZT are also possible with TlBr. The electrical detection of deep levels has also proved that they are likely responsible for the observed high resistivity of the material.

The transient shapes discovered at temperatures higher than 250 K have shown that traditional PICTS analysis methods are inadequate for TlBr at these temperatures. It is possible that the observed shapes can be modeled with rate equations for carrier concentrations in which only electrons and holes are considered. A study attempting to reproduce the shapes with these equations could yield interesting information about trap parameters and the position of the Fermi level in TlBr. A similar study was conducted in order to explain anomalous negative PICTS peaks observed in measurements of SI GaAs above 300 K.[112] In that work, by fitting numerical solutions of the coupled rate equations governing free carrier populations to the SI GaAs PICTS data, the group was able to ascertain conditions for the position of the Fermi level relative to the deep levels in the material. It is also possible, however, that the observed transient shapes cannot be explained with an electronic conductivity model only. The appearance of the shapes at temperatures in which ionic conductivity is known to become significant suggest that ionic transport could be playing a role. Whether the origin of the shapes is ultimately electronic or ionic, developing a model to understand them would have great benefit, as it would enable more accurate analysis of trap signals at higher temperature. The application of naive four-gate analysis to several of the trap peaks visible above 250 K in the TlBr samples measured has yielded activation energies in the range of 0.8 eV - $\sim$2 eV. While these values are inaccurate because the shape of the underlying transients invalidates the analysis method, they do give an indication that a more accurate analysis could potentially reveal a trap or traps responsible for pinning the Fermi level in TlBr. As discussed in Section 3.5.2, such a trap must have an activation energy of $\sim$0.7 eV or higher.

The MWPC measurements performed in this dissertation have yielded experimental life-

time measurements in good general agreement with other more indirect methods of assessing carrier lifetimes. They have demonstrated the efficacy of using the measurement as a fast and contact-less way of assessing material quality through an estimation of the bulk lifetime. With properly prepared samples, MWPC measurements could be used to evaluate different surface processing techniques of TlBr. They have also proved useful for assessing the effects of various dopants on charge transport in TlBr. It has been shown that Pb-, Se-, and O-doping have strongly deleterious effects on charge transport, whereas C-doping does not. The data from the C-doped samples indicates that the presence of carbon may even improve carrier lifetime in TlBr, though a larger sample size of both C-doped and undoped samples would be desired to firmly establish this, along with data from other measurements such as Hecht analysis of the $\mu\tau$ product discussed in Section 5.1.1.

The PICTS measurements presented in this dissertation provide a useful starting point for further deep level studies in TlBr. With the establishment of a baseline of electrically detected traps in TlBr, it is possible to design experiments to determine the origin of the traps. The Arrhenius plots for all detected traps across all samples are shown in Figure 7.1. The figure contains a wealth of information to guide further experimental observations. It can be seen that some traps were detected in multiple samples of different doping and form relatively tight groups with consistent slopes and activation energies. The groups labeled *I* and *III* in Figure 7.1 fit this description. These traps are therefore likely related to single native defects or impurities common to all samples. Some distinct traps such as PB2, PB3, and SE2 do not fit into the groups, and are likely related to the respective Pb- and Se-dopants in the samples. Further PICTS experiments with more doped samples could confirm these observations. Meanwhile, the traps loosely grouped under the label *IV* show a broad range of activation energies and cross sections that could be explained either by distinct transitions from many different traps, or by broadened transitions related to mechanical damage and extended defects in the material.

Studies employing deliberate damage of TlBr samples could answer some of these questions about the origin of the traps in Figure 7.1. As an example, TlBr samples could be irradiated to alter the populations of native defects. The resulting changes in deep level concentrations would manifest in PICTS spectra. Studies in which TlBr samples are measured with PICTS before and after deliberate mechanical damage would also be useful to see if energy-level broadening effects due to plastic deformation could be detected with PICTS. Variations of PICTS technique in which the trap filling pulse is varied can also be performed to separate emission from interacting defects (such as a point defect in the vicinity of a dislocation) characterized by a Coulombic barrier from isolated single defects.[67] Annealing studies combined with PICTS and MWPC also have the potential to reveal much about defects and transport in TlBr. All of these studies can be combined with information from first principles calculations of both native and extrinsic defect energy levels in TlBr. Once the chemical or structural origin of the traps is understood and the defects responsible for the resistivity of TlBr identified, then growth process alterations designed specifically with deep level engineering in mind can be attempted to further improve the electronic properties of TlBr. This in turn would lead to improved device performance.

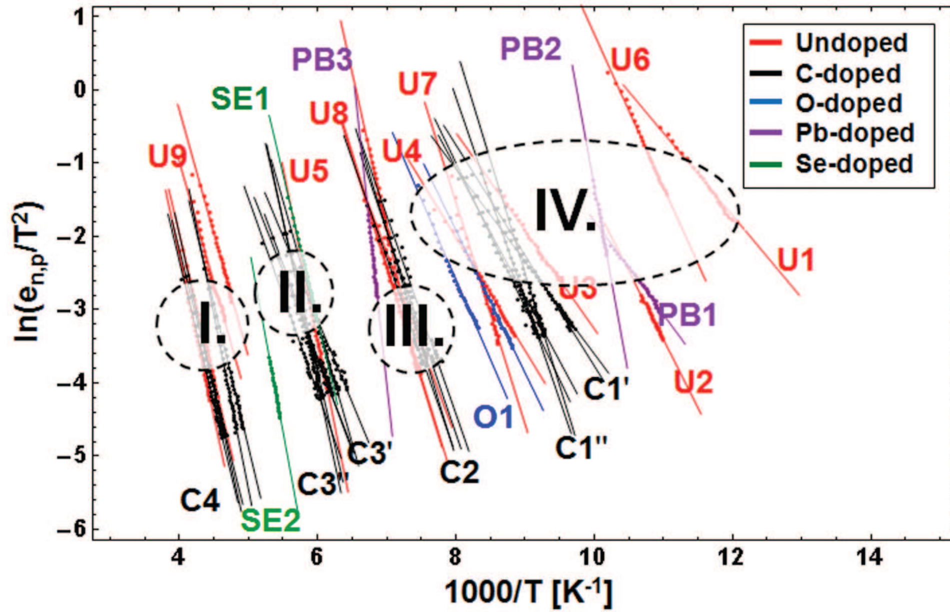

Figure 7.1: Arrhenius plots for all traps discovered with PICTS in all of the TlBr samples, differentiated in color by the sample dopant.

Perhaps the commercially most important direction for further application of the deep level techniques used in this dissertation is to evaluate the electronic effects of other dopants that may limit the ionic conductivity of TlBr. Despite the remarkable improvement of transport characteristics and energy resolution achievements, TlBr detectors will likely never be widespread unless the polarization problem is eliminated. Charge neutrality doping seems to hold great promise to help with the issue, but suitable dopants have yet to be found that are capable of lowering the ionic conductivity without significantly harming the electronic conductivity.

Bibliography

[1] I. A. E. Agency, "IAEA Illicit Trafficking Database (ITDB)." `http://www.iaea.org/newscenter/features/radsources/pdf/itdb_31122003.pdf`, 2003.

[2] C. A. Klein, "Bandgap dependence and related features of radiation ionization energies in semiconductors," *Journal of Applied Physics*, vol. 39, pp. 2029 –2038, March 1968.

[3] J. S. S. Hitch, R. Keyser and T. Twomey, "Why high-purity germanium (HPGe) radiation detection technology is superior to other detector technologies for isotope identification," tech. rep., Ortec, 2006.

[4] G. F. Knoll, *Radiation Detection and Measurement*. John Wiley & Sons, Inc., 2010.

[5] E. E. Haller, W. L. Hansen, and F. S. Goulding, "Physics of ultra-pure germanium," *Advances in Physics*, vol. 30, no. 1, pp. 93–138, 1981.

[6] M. Schieber, R. James, and T. Schlesinger, "Chapter 15: Summary and Remaining Issues for Room Temperature Radiation Spectrometers," in *Semiconductors for Room Temperature Nuclear Detector Applications* (T. Schlesinger and R. B. James, eds.), vol. 43 of *Semiconductors and Semimetals*, pp. 561 – 583, Elsevier, 1995.

[7] P. Luke and M. Amman, "Room-temperature replacement for Ge detectors: Are we there yet?," *Nuclear Science, IEEE Transactions on*, vol. 54, pp. 834 –842, August 2007.

[8] J. Fink, H. Krueger, P. Lodomez, and N. Wermes, "Characterization of charge collection in CdTe and CZT using the transient current technique," *Nuclear Instruments and Methods in Physics Research Section A: Accelerators, Spectrometers, Detectors and Associated Equipment*, vol. 560, no. 2, pp. 435 – 443, 2006.

[9] C. Szeles, "Advances in the crystal growth and device fabrication technology of CdZnTe room temperature radiation detectors," *IEEE Transactions on Nuclear Science*, vol. 51, pp. 1242 – 1249, June 2004.

[10] E. S. Elshazly, G. Tepper, and A. Burger, "Charge trapping in detector grade thallium bromide and cadmium zinc telluride: Measurement and theory," *Nuclear Instruments*

and Methods in Physics Research Section A: Accelerators, Spectrometers, Detectors and Associated Equipment, vol. 620, no. 2-3, pp. 279 – 284, 2010.

[11] K. Hitomi, M. Matsumoto, O. Muroi, T. Shoji, and Y. Hiratate, "Characterization of thallium bromide crystals for radiation detector applications," *Journal of Crystal Growth*, vol. 225, no. 2-4, pp. 129 – 133, 2001.

[12] T. Schlesinger, J. Toney, H. Yoon, E. Lee, B. Brunett, L. Franks, and R. James, "Cadmium zinc telluride and its use as a nuclear radiation detector material," *Materials Science and Engineering: R: Reports*, vol. 32, no. 45, pp. 103 – 189, 2001.

[13] A. N. Tyler, "In situ and airborne gamma-ray spectrometry," in *Analysis of Environmental Radionuclides* (P. P. Povinec, ed.), vol. 11 of *Radioactivity in the Environment*, pp. 407 – 448, Elsevier, 2008.

[14] P. J. Sellin, "Recent advances in compound semiconductor radiation detectors," *Nuclear Instruments and Methods in Physics Research Section A: Accelerators, Spectrometers, Detectors and Associated Equipment*, vol. 513, no. 12, pp. 332 – 339, 2003.

[15] H. Kim, L. Cirignano, A. Churilov, G. Ciampi, W. Higgins, F. Olschner, and K. Shah, "Developing larger TlBr detectors: Detector performance," *Nuclear Science, IEEE Transactions on*, vol. 56, pp. 819 –823, June 2009.

[16] K. Shah, J. Lund, F. Olschner, L. Moy, and M. Squillante, "Thallium bromide radiation detectors," *IEEE Transactions on Nuclear Science*, vol. 36, pp. 199 –202, February 1989.

[17] V. Kozlov, *TlBr raw material purification, crystal growth, annealing, detector fabrication and characterisation for gamma-ray detector applications.* PhD thesis, University of Helsinki, 2010.

[18] D. McGregor and H. Hermon, "Room-temperature compound semiconductor radiation detectors," *Nuclear Instruments and Methods in Physics Research Section A: Accelerators, Spectrometers, Detectors and Associated Equipment*, vol. 395, no. 1, pp. 101 – 124, 1997.

[19] I. Gazizov and V. Zaletin, "The sensitivity of pure and doped tlbr crystals," in *Nuclear Science Symposium Conference Record (NSS/MIC), 2010 IEEE*, pp. 3704 –3708, November 2010.

[20] V. Deich and M. Roth, "Improved performance lead iodide nuclear radiation detectors," *Nuclear Instruments and Methods in Physics Research Section A: Accelerators, Spectrometers, Detectors and Associated Equipment*, vol. 380, no. 1-2, pp. 169 – 172, 1996.

[21] M. Kouznetsov, I. Lisitsky, S. Zatoloka, and V. Gostilo, “Development of the technology for growing TlBr detector crystals,” *Nuclear Instruments and Methods in Physics Research Section A: Accelerators, Spectrometers, Detectors and Associated Equipment*, vol. 531, no. 1-2, pp. 174 – 180, 2004.

[22] A. Owens, M. Bavdaz, I. Lisjutin, A. Peacock, H. Sipila, and S. Zatoloka, “On the development of compound semiconductor thallium bromide detectors for astrophysics,” *Nuclear Instruments and Methods in Physics Research Section A: Accelerators, Spectrometers, Detectors and Associated Equipment*, vol. 458, no. 1-2, pp. 413 – 417, 2001.

[23] V. Kozlov, H. Andersson, V. Gostilo, M. Kemell, P. Kostamo, M. Kouznetsov, M. Leskel, H. Lipsanen, I. Lisitsky, M. Shorohov, and H. Sipil, “Improvements and problems of bridgmanstockbarger method for fabrication of TlBr single crystal detectors,” *Nuclear Instruments and Methods in Physics Research Section A: Accelerators, Spectrometers, Detectors and Associated Equipment*, vol. 607, no. 1, pp. 126 – 128, 2009.

[24] A. V. Churilov, W. M. Higgins, G. Ciampi, H. Kim, L. J. Cirignano, F. Olschner, and K. S. Shah, “Purification, crystal growth and detector performance of TlBr,” *Proc. SPIE*, vol. 7079, p. 70790K, 2008.

[25] D. Zhou, L. Quan, X. Chen, S. Yu, C. Wang, Z. Zheng, and S. Gong, “A novel method to grow thallium bromide single crystal and crystal habit discussion,” *Crystal Growth & Design*, vol. 9, no. 10, pp. 4296–4300, 2009.

[26] P. Bennett, K. Shah, L. Cirignano, M. Klugerman, L. Moy, F. Olschner, and M. Squillante, “Characterization of polycrystalline TlBr films for radiographic detectors,” *IEEE Transactions on Nuclear Science*, vol. 46, pp. 266 –270, June 1999.

[27] A. Bolotnikov, G. Camarda, G. Carini, Y. Cui, K. Kohman, L. Li, M. Salomon, and R. James, “Performance-limiting defects in CdZnTe detectors,” *Nuclear Science, IEEE Transactions on*, vol. 54, pp. 821 –827, August 2007.

[28] N. Zambelli, L. Marchini, M. Zha, and A. Zappettini, “Three-dimensional mapping of tellurium inclusions in CdZnTe crystals by means of improved optical microscopy,” *Journal of Crystal Growth*, vol. 318, no. 1, pp. 1167 – 1170, 2011.

[29] Y. Liao, E. Heidari, G. Abramovich, C. Nafis, A. Butt, J. Czechowski, K. Harding, and J. E. Tkaczyk, “Automated 3D IR defect mapping system for CZT wafer and tile inspection and characterization,” *Proc. SPIE 8133, Dimensional Optical Metrology and Inspection for Practical Applications*, pp. 81330P–81330P–12, 2011.

[30] K. Hitomi, T. Onodera, and T. Shoji, “Influence of zone purification process on TlBr crystals for radiation detector fabrication,” *Nuclear Instruments and Methods in Physics Research Section A: Accelerators, Spectrometers, Detectors and Associated Equipment*, vol. 579, no. 1, pp. 153 – 156, 2007.

[31] Q. Li, M. Beilicke, K. Lee, A. G. III, Q. Guo, J. Martin, Y. Yin, P. Dowkontt, G. D. Geronimo, I. Jung, and H. Krawczynski, "Study of thick CZT detectors for X-ray and Gamma-ray astronomy," *Astroparticle Physics*, vol. 34, no. 10, pp. 769 – 777, 2011.

[32] V. Gostilo, A. Owens, M. Bavdaz, I. Lisjutin, A. Peacock, H. Sipila, and S. Zatoloka, "Single detectors and pixel arrays based on TlBr," *Nuclear Science, IEEE Transactions on*, vol. 49, pp. 2513 – 2516, October 2002.

[33] H. Kim, A. Churilov, G. Ciampi, L. Cirignano, W. Higgins, S. Kim, P. ODougherty, F. Olschner, and K. Shah, "Continued development of thallium bromide and related compounds for gamma-ray spectrometers," *Nuclear Instruments and Methods in Physics Research Section A: Accelerators, Spectrometers, Detectors and Associated Equipment*, vol. 629, no. 1, pp. 192 – 196, 2011.

[34] A. V. Churilov, G. Ciampi, H. Kim, W. M. Higgins, L. J. Cirignano, F. Olschner, V. Biteman, M. Minchello, and K. S. Shah, "TlBr and $TlBr_xI_{1x}$ crystals for γ-ray detectors," *Journal of Crystal Growth*, vol. 312, no. 8, pp. 1221 – 1227, 2010.

[35] K. Hitomi, T. Tada, T. Onodera, S. Kim, Y. Xu, T. Shoji, and K. Ishii, "TlBr capacitive Frisch grid detectors," *Nuclear Science, IEEE Transactions on*, vol. PP, no. 99, pp. 1 –6, 2012.

[36] G. A. Samara, "Pressure and temperature dependences of the ionic conductivities of the thallous halides TlCl, TlBr, and TlI," *Phys. Rev. B*, vol. 23, pp. 575–586, January 1981.

[37] C. P. Flynn, *Point Defects and Diffusion*. Clarendon, Oxford, 1972.

[38] S. R. Bishop, W. Higgins, A. Churilov, G. Ciampi, H. Kim, L. Cirignano, V. Biteman, J. Tower, K. Shah, and H. Tuller, "Characterization of conductivity in single crystal TlBr," *ECS Transactions*, vol. 28, no. 11, pp. 333–338, 2010.

[39] S. R. Bishop, W. Higgins, G. Ciampi, A. Churilov, K. S. Shah, and H. L. Tuller, "The defect and transport properties of donor doped single crystal TlBr," *Journal of The Electrochemical Society*, vol. 158, no. 2, pp. J47–J51, 2011.

[40] H. L. Tuller and S. R. Bishop, "Point defects in oxides: Tailoring materials through defect engineering," *Annual Review of Materials Research*, vol. 41, no. 1, pp. 369–398, 2011.

[41] S. R. Bishop, H. L. Tuller, G. Ciampi, W. Higgins, J. Engel, A. Churilov, and K. S. Shah, "The defect and transport properties of acceptor doped TlBr: role of dopant exsolution and association," *Physical Chemistry Chemical Physics*, vol. 14, pp. 10160–10167, 2012.

[42] P. Blood and J. Orton, *The Electrical Characterization of Semiconductors: Majority Carriers and Electron States*. Academic Press, 1992.

[43] F. Urbach, "Messmethoden and ergebnisse: Der theorie der thermolumineszenz," *Akademie der Wissenschaften, Weiner, Berlin (IIA)*, vol. 139, p. 363, 1930.

[44] G. A. Dussel and R. H. Bube, "Theory of thermally stimulated conductivity in a previously photoexcited crystal," *Phys. Rev.*, vol. 155, pp. 764–779, March 1967.

[45] D. Lang, "Deep-level transient specroscopy: A new method to characterize traps in semiconductors," *Journal of Applied Physics*, vol. 45, no. 7, pp. 3023–3032, 1974.

[46] R. Williams, "Determination of deep centers in conducting gallium arsenide," *Journal of Applied Physics*, vol. 37, pp. 3411 –3416, aug 1966.

[47] D. Lang and R. Logan, "A study of deep levels in GaAs by capacitance spectroscopy," *Journal of Electronic Materials*, vol. 4, pp. 1053–1066, 1975.

[48] C. Hurtes, M. Boulou, A. Mitonneau, , and D. Bois, "Deep-level spectroscopy in high-resistivity materials," *Applied Physics Letters*, vol. 32, p. 821, 1978.

[49] J. C. Balland, J. P. Zielinger, M. Tapiero, J. G. Gross, and C. Noguet, "Investigation of deep levels in high-resistivity bulk materials by photo-induced current transient spectroscopy. II. Evaluation of various signal processing methods," *Journal of Physics D: Applied Physics*, vol. 19, no. 1, p. 71, 1986.

[50] O. Yoshie and M. Kamihara, "Photo-induced current transient spectroscopy in high-resistivity bulk material. I. computer controlled multi-channel PICTS system with high-resolution," *Japanese Journal of Applied Physics*, vol. 22, no. Part 1, No. 4, pp. 621–628, 1983.

[51] M. Tapiero, N. Benjelloun, J. P. Zielinger, S. El Hamd, and C. Noguet, "Photoinduced current transient spectroscopy in high-resistivity bulk materials: Instrumentation and methodology," *Journal of Applied Physics*, vol. 64, pp. 4006 –4012, October 1988.

[52] K. Yasutake, H. Kakiuchi, A. Takeuchi, K. Yoshii, and H. Kawabe, "Deep-level characterization in semi-insulating GaAs by photo-induced current and Hall effect transient spectroscopy," *Journal of Materials Science: Materials in Electronics*, vol. 8, pp. 239–245, 1997.

[53] F. Nava, C. Canali, A. Castaldini, A. Cavallini, S. D'Auria, C. D. Papa, C. Frigeri, L. Zanotti, A. Cetronio, C. Lanzieri, and A. Zichichi, "Influence of electron traps on charge-collection efficiency in GaAs radiation detectors," *Nuclear Instruments and Methods in Physics Research Section A: Accelerators, Spectrometers, Detectors and Associated Equipment*, vol. 349, no. 1, pp. 156 – 159, 1994.

[54] F. Nava, M. Alietti, C. Canali, A. Cavallini, C. Chiossi, C. del Papa, V. Re, and C. Lanzieri, "Performances of SI GaAs detectors fabricated with implanted ohmic contacts," *Nuclear Science, IEEE Transactions on*, vol. 43, pp. 1130 –1136, June 1996.

[55] P. Hlinomaz, V. Šmíd, J. Krištofik, and J. Mareš, "A comparison of different types of signal processing in PICTS measurements," *Solid State Communications*, vol. 78, no. 11, pp. 947 – 951, 1991.

[56] V. Kazukauskas, A. Ziminskij, V. Bozhko, and G. Muronchuk, "Persistent photocurrent and defects in TlBr," *Materialwissenschaft und Werkstofftechnik*, vol. 42, no. 1, pp. 75–78, 2011.

[57] V. Kazukauskas, A. Ziminskij, N. Vainorius, V. Gostilo, M. Shorohov, and V. Bozh, "Long-lasting current transient phenomena in TlBr," *Acta Physica Polonica A*, vol. 119, 2010.

[58] N. Smirnov, I. Lisitsky, M. Kuznetsov, A. Govorkov, and E. Kozhukhova, "Electrophysical characteristics of TlBr crystals grown in various ambients," in *Nuclear Science Symposium Conference Record, 2006. IEEE*, vol. 6, pp. 3700 –3704, November 2006.

[59] J. S. Blakemore, *Semiconductor Statistics*. Dover Publications, Inc., 1962,1987.

[60] M. Fiederle, V. Babentsov, J. Franc, A. Fauler, and J.-P. Konrath, "Growth of high resistivity CdTe and (Cd,Zn)Te crystals," *Crystal Research and Technology*, vol. 38, no. 7-8, pp. 588–597, 2003.

[61] V. Babentsov, J. Franc, P. Hschl, M. Fiederle, K. W. Benz, N. V. Sochinskii, E. Dieguez, and R. B. James, "Characterization of compensation and trapping in CdTe and CdZnTe: Recent advances," *Crystal Research and Technology*, vol. 44, no. 10, pp. 1054–1058, 2009.

[62] M.-H. Du, "First-principles study of native defects in TlBr: Carrier trapping, compensation, and polarization phenomenon," *Journal of Applied Physics*, vol. 108, September 2010.

[63] W. Walukiewicz, "Mechanism of Fermi-level stabilization in semiconductors," *Phys. Rev. B*, vol. 37, pp. 4760–4763, March 1988.

[64] H. M. Smith, D. J. Phillips, I. D. Sharp, J. W. Beeman, D. C. Chrzan, N. M. Haegel, E. E. Haller, G. Ciampi, H. Kim, and K. S. Shah, "Electronic effects of Se and Pb dopants in TlBr," *Applied Physics Letters*, vol. 100, pp. 202102 –202102–4, May 2012.

[65] J. C. Balland, J. P. Zielinger, C. Noguet, and M. Tapiero, "Investigation of deep levels in high-resistivity bulk materials by photo-induced current transient spectroscopy. I. Review and analysis of some basic problems," *Journal of Physics D: Applied Physics*, vol. 19, no. 1, p. 57, 1986.

[66] W. A. Doolittle and A. Rohatgi, "A novel computer based pseudo-logarithmic capacitance/conductance dlts system specifically designed for transient analysis," *Review of Scientific Instruments*, vol. 63, p. 5733, 1992.

[67] P. Omling, E. R. Weber, L. Montelius, H. Alexander, and J. Michel, "Electrical properties of dislocations and point defects in plastically deformed silicon," *Phys. Rev. B*, vol. 32, pp. 6571–6581, November 1985.

[68] V. V. Kveder, Y. A. Osipyan, W. Schrter, and G. Zoth, "On the energy spectrum of dislocations in silicon," *Physica Status Solidi (A)*, vol. 72, no. 2, pp. 701–713, 1982.

[69] W. Schröter, J. Kronewitz, U. Gnauert, F. Riedel, and M. Seibt, "Bandlike and localized states at extended defects in silicon," *Phys. Rev. B*, vol. 52, pp. 13726–13729, Nov 1995.

[70] M. Shorohov, F. Muktepavela, L. Grigorjeva, J. Maniks, and D. Millers, "Surface processing of TlBr single crystals used for radiation detectors," *Nuclear Instruments and Methods in Physics Research Section A: Accelerators, Spectrometers, Detectors and Associated Equipment*, vol. 607, no. 1, pp. 120 – 122, 2009.

[71] C. Kisielowski and E. R. Weber, "Inhomogeneities in plastically deformed silicon single crystals. II. Deep-level transient spectroscopy investigations of p - and n -doped silicon," *Phys. Rev. B*, vol. 44, pp. 1600–1612, July 1991.

[72] C. Marquardt and R. Williams, "Recombination centers in TlBr," *Journal of Luminescence*, vol. 9, no. 5, pp. 440 – 448, 1974.

[73] C. R. Leão and V. Lordi, "Simultaneous control of ionic and electronic conductivity in materials: Thallium bromide case study," *Phys. Rev. Lett.*, vol. 108, p. 246604, June 2012.

[74] G. F. Neumark, "Effect of deep levels on semiconductor carrier concentrations in the case of "strong" compensation," *Phys. Rev. B*, vol. 26, pp. 2250–2252, August 1982.

[75] M.-H. Du, "First-principles study of impurities in TlBr," *Journal of Applied Physics*, vol. 111, pp. 073519 –073519–4, April 2012.

[76] A. D. Brothers and D. W. Lynch, "Optical properties of AgCl, AgBr, TlCl, and TlBr under hydrostatic pressure," *Phys. Rev.*, vol. 180, pp. 911–918, Apr 1969.

[77] R. Z. Bachrach and F. C. Brown, "Exciton-optical properties of TlBr and TlCl," *Phys. Rev. B*, vol. 1, pp. 818–831, January 1970.

[78] L. Grabner, "Exciton emission and donor-acceptor association in thallium bromide," *Phys. Rev. B*, vol. 4, pp. 1335–1339, August 1971.

[79] R. Shimizu, T. Murahashi, and T. Kōda, "Indirect edge of TlBr as observed in the luminescence excitation spectra," *Journal of the Physical Society of Japan*, vol. 33, no. 3, pp. 866–866, 1972.

[80] J. Nakahara and K. Kobayashi, "Edge emissions and broad band emissions in thallous halides," *Journal of the Physical Society of Japan*, vol. 40, no. 1, pp. 180–188, 1976.

[81] C. W. Jurgensen and H. G. Drickamer, "High-pressure studies of the absorption edges of three thallous halides," *Phys. Rev. B*, vol. 30, pp. 7202–7205, December 1984.

[82] V. Kohlová, I. Pelant, J. Hála, M. Ambroz, and K. Vacek, "Luminescence of direct-and indirect-gap electron-hole plasma in TlBr," *Solid State Communications*, vol. 62, no. 2, pp. 105 – 108, 1987.

[83] I. Pelant, V. Kohlová, J. Hála, M. Ambroz, and K. Vacek, "Direct-indirect gap intervalley scattering of electrons in TlBr electron-hole plasma," *Solid State Communications*, vol. 64, no. 6, pp. 939 – 942, 1987.

[84] K. Hayakawa, K. Hitomi, T. Shoji, and C. Onodera, "Photoluminescence analysis of TlBr crystals for radiation detector applications," in *Nuclear Science Symposium Conference Record (NSS/MIC), 2009 IEEE*, pp. 1647 –1648, November 2009.

[85] P. Yu and M. Cardona, *Fundamentals of Semiconductors*. Springer, 2001.

[86] Y. Toyozawa, "On the dynamical behavior of an exciton," *Progress of Theoretical Physics Supplement*, vol. 12, pp. 111–140, 1959.

[87] R. H. Bube, *Photoelectronic Properties of Semiconductors*. Cambridge University Press, 1992.

[88] L. Grabner, "Isoelectronic donor iodine and broad-band photoluminescence in TlBr," *Phys. Rev. B*, vol. 14, pp. 2514–2519, September 1976.

[89] O. Engström and A. Alm, "Thermodynamical analysis of optimal recombination centers in thyristors," *Solid-State Electronics*, vol. 21, no. 1112, pp. 1571 – 1576, 1978.

[90] R. Shimizu, T. Kōda, and T. Murahashi, "Exciton luminescence in TlBr and TlCl," *Journal of the Physical Society of Japan*, vol. 36, no. 1, pp. 161–168, 1974.

[91] L. Grigorjeva and D. Millers, "The model of recombination process in TlBr," *Nuclear Instruments and Methods in Physics Research Section B: Beam Interactions with Materials and Atoms*, vol. 191, no. 14, pp. 131 – 134, 2002.

[92] A. Fujii, H. Ueda, M. Tabuki, and K. Miyazaki, "Extrinsic self-trapping of excitons in TlBr(I)," *Journal of Luminescence*, vol. 112, no. 1-4, pp. 84 – 87, 2005.

[93] D. S. McClure and C. Pedrini, "Excitons trapped at impurity centers in highly ionic crystals," *Phys. Rev. B*, vol. 32, pp. 8465–8468, Dec 1985.

[94] D. J. Phillips, K. E. Blaine, L. J. Cirignano, G. Ciampi, and N. M. Haegel, "Cathodoluminescence and spatial variation in mobility-lifetime product in bulk doped thallium bromide," *IEEE Transactions on Nucle*, vol. 59, p. 2608, 2012.

[95] T. Kawai, K. Kobayashi, M. Kurita, and Y. Makita, "Drift mobilities of electrons and holes in thallous bromide," *Journal of the Physical Society of Japan*, vol. 30, no. 4, pp. 1101–1105, 1971.

[96] K. Hitomi, M. Matsumoto, O. Muroi, T. Shoji, and Y. Hiratate, "Thallium bromide optical and radiation detectors for X-ray and gamma-ray spectroscopy," *Nuclear Science, IEEE Transactions on*, vol. 49, pp. 2526 – 2529, October 2002.

[97] F. Olschner, M. Toledo-Quinones, K. Shah, and J. Lund, "Charge carrier transport properties in thallium bromide crystals used as radiation detectors," *Nuclear Science, IEEE Transactions on*, vol. 37, pp. 1162 –1164, jun 1990.

[98] V. Gostilo, A. Owens, M. Bavdaz, I. Lisjutin, A. Peacock, H. Sipila, and S. Zatoloka, "A comparison of the X-ray performance of TlBr crystals grown by the Bridgeman-Stockbarger and travelling molten zone methods," *Nuclear Instruments and Methods in Physics Research Section A: Accelerators, Spectrometers, Detectors and Associated Equipment*, vol. 509, no. 1-3, pp. 47 – 51, 2003.

[99] T. Onodera, K. Hitomi, T. Shoji, Y. Hiratate, and H. Kitaguchi, "Spectroscopic performance of pixellated thallium bromide detectors," *IEEE Transactions on Nuclear Science*, vol. 52, pp. 1999 – 2002, October 2005.

[100] P. Luke and E. Eissler, "Performance of CdZnTe coplanar-grid gamma-ray detectors," *Nuclear Science, IEEE Transactions on*, vol. 43, pp. 1481 –1486, June 1996.

[101] A. Sanders and M. Kunst, "Characterization of silicon wafers by transient microwave photoconductivity measurements," *Solid-State Electronics*, vol. 34, no. 9, pp. 1007 – 1015, 1991.

[102] G. C. Tepper, R. Kessick, and C. Szeles, "Investigation of the electronic properties of cadmium zinc telluride surfaces using pulsed laser microwave cavity perturbation," pp. 79–89, 2001.

[103] O. Ambacher, W. Rieger, P. Ansmann, H. Angerer, T. Moustakas, and M. Stutzmann, "Sub-bandgap absorption of gallium nitride determined by photothermal deflection spectroscopy," *Solid State Communications*, vol. 97, no. 5, pp. 365 – 370, 1996.

[104] M. Kunst and G. Beck, "The study of charge carrier kinetics in semiconductors by microwave conductivity measurements. II.," *Journal of Applied Physics*, vol. 63, pp. 1093 –1098, February 1988.

[105] M. Schofthaler and R. Brendel, "Sensitivity and transient response of microwave reflection measurements," *Journal of Applied Physics*, vol. 77, pp. 3162 –3173, April 1995.

[106] J. Vaitkus, V. Gostilo, R. Jasinskaite, A. Mekys, A. Owens, S. Zatoloka, and A. Zindulis, "Investigation of degradation of electrical and photoelectrical properties in TlBr crystals," *Nuclear Instruments and Methods in Physics Research Section A: Accelerators, Spectrometers, Detectors and Associated Equipment*, vol. 531, no. 1-2, pp. 192 – 196, 2004.

[107] V. Kozlov, M. Kemell, M. Vehkamki, and M. Leskel, "Degradation effects in TlBr single crystals under prolonged bias voltage," *Nuclear Instruments and Methods in Physics Research Section A: Accelerators, Spectrometers, Detectors and Associated Equipment*, vol. 576, no. 1, pp. 10 – 14, 2007.

[108] J. Vaitkus, J. Banys, V. Gostilo, S. Zatoloka, A. Mekys, J. Storasta, and A. Žindulis, "Influence of electronic and ionic processes on electrical properties of TlBr crystals," *Nuclear Instruments and Methods in Physics Research Section A: Accelerators, Spectrometers, Detectors and Associated Equipment*, vol. 546, no. 1-2, pp. 188 – 191, 2005.

[109] K. Hitomi, Y. Kikuchi, T. Shoji, and K. Ishii, "Polarization phenomena in TlBr detectors," *IEEE Transactions on Nuclear Science*, vol. 56, pp. 1859 –1862, August 2009.

[110] M. Gershenzon, F. A. Trumbore, R. M. Mikulyak, and M. Kowalchik, "Radiative recombination between deep donor-acceptor pairs in GaP," *Journal of Applied Physics*, vol. 36, pp. 1528 –1537, May 1965.

[111] M. Gershenzon, F. A. Trumbore, R. M. Mikulyak, and M. Kowalchik, "Evidence for radiative recombination between deep donor-acceptor pairs in GaP at room temperature," *Journal of Applied Physics*, vol. 37, pp. 483 –486, February 1966.

[112] S. Schmerler, T. Hahn, S. Hahn, J. R. Nikla, and B. Gr̀undig-Wendrock, "Explanation of positive and negative PICTS peaks in SI-GaAs," *Journal of Materials*, vol. 19, December 2008.

[113] L. G. Schulz, "Polymorphism of cesium and thallium halides," *Journal of Chemical Physics*, vol. 18, p. 996, 1950.

[114] L. G. Schulz, "Polymorphism of cesium and thallium halides," *Acta Crystallographica*, vol. 4, pp. 487–489, November 1951.

[115] I. H. Khan, "On the polymorphism of the thallium halides," *Proceedings of the Physical Society*, vol. 76, no. 4, p. 507, 1960.

[116] G. E. Morse and A. Lawson, "The temperature and pressure dependence of the elastic constants of thallium bromide," *Journal of Physics and Chemistry of Solids*, vol. 28, no. 6, pp. 939 – 950, 1967.

[117] G. A. Samara, "Temperature and pressure dependence of the dielectric constants of the thallous halides," *Phys. Rev.*, vol. 165, pp. 959–969, January 1968.

[118] M. Blackman and I. H. Khan, "The polymorphism of thallium and other halides at low temperatures," *Proceedings of the Physical Society*, vol. 77, no. 2, p. 471, 1961.

[119] J. Ungelenk, "Zur polymorphie der thalliumhalogenide in aufdampfschichten," *Physik der kondensierten Materie*, vol. 1, pp. 152–175, 1963.

[120] G. Kresse and J. Hafner, "*Ab initio* molecular dynamics for liquid metals," *Phys. Rev. B*, vol. 47, pp. 558–561, January 1993.

[121] J. Perdew, M. Ernzerhof, and K. Burke, "Rationale for mixing exact exchange with density functional approximations," *Journal of Chemical Physics*, vol. 105, pp. 9982–9985, December 1996.

[122] J. P. Perdew, K. Burke, and M. Ernzerhof, "Generalized gradient approximation made simple," *Phys. Rev. Lett.*, vol. 77, pp. 3865–3868, Oct 1996.

[123] G. Kresse and D. Joubert, "From ultrasoft pseudopotentials to the projector augmented-wave method," *Phys. Rev. B*, vol. 59, pp. 1758–1775, Jan 1999.

[124] K. Heidrich, W. Staude, J. Treusch, and H. Overhof, "Optical properties and electronic structure of polymorphous TICI and TIBr," *Phys. Rev. Lett.*, vol. 33, pp. 1220–1223, November 1974.

[125] J. McClelland and D. Lynch, "Electroabsorption of excitons in f.c.c. TlBr and TlCl," *Solid State Communications*, vol. 20, no. 3, pp. 265 – 268, 1976.

Appendix A

Polymorphism of TlBr and First Principles Band Structure Calculations

A.1 The Polymorphism of TlBr

At room temperature, bulk TlBr has a CsCl crystal structure that is well established by X-ray diffraction measurements (XRD). There are several experimental reports of TlBr assuming two other crystal structures as well however. In the early 1950's, Schulz reported the results of growing TlBr thin films on LiF, NaCl, and KBr substrates. It was found that for very thin films, the TlBr took on a NaCl (rock-salt) structure. As films were grown thicker, new grains not in contact with the substrate took the normal CsCl structure. Films thicker than several hundred angstroms featured diffraction patterns that showed only the CsCl structure.[113, 114] In 1960, Khan deposited TlBr thin films on four types of substrates - cleaved faces of single crystals, polished and etched faces of ground crystal surfaces, single crystal films of silver and gold deposited on NaCl and mica, and polycrystalline films of alkali halides deposited on to amorphous bases. The TlBr films grown on the cleaved faces and the etched and polished faces of several single crystals (LiF, NaF, NaCl, KCl, KBr, KI, RbI) assumed an NaCl structure. Once again, Khan observed the normal CsCl diffraction pattern for films with thicknesses above several hundred angstroms. TlBr films grown on the metal films as well as a few other substrates showed the normal CsCl structure, raising the question of whether the NaCl form of TlBr arose out of interaction with the substrate.[115]

Another study by Blackman and Kahn in 1966 explored the effects of temperature on the process. They deposited thin films of TlBr on amorphous substrates at temperatures $\sim$110 K, below the Debye temperature of TlBr of $\sim$130 K. [116, 117] They found that at low temperature, thin TlBr films assumed an NaCl structure, proving that the form could occur even without a substrate also featuring a rock-salt crystal structure. However, diffraction rings related to the CsCl structure were also visible, and as the films were grown

thicker, the NaCl pattern decreased in intensity relative to the CsCl pattern. The NaCl pattern disappeared entirely before room temperature was reached.[118] In 1963, a study by Ungelenk described the room temperature evaporation of TlBr thin films onto cleaved faces of alkali halide crystals with an NaCl structure. In contrast to previous work, he found that the films did not have NaCl or CsCl structures, but instead grew in an orthorhombic structure, similar to that of TlI. In agreement with previous studies however, it was found once again that above a certain thickness, the films assumed the CsCl structure.[119]

Despite some contrasting results between these reports, it seems well established that thin films of TlBr with thicknesses less than hundreds of angstroms have been grown with both NaCl and orthorhombic crystal structures on a variety of substrates, at temperatures ranging from $\sim$110 K to room temperature. All reports found that films with thicknesses equal to or greater than hundreds of angstroms at room temperature exhibited only the CsCl structure, independent of the substrate choice.

The report of spontaneous growth of TlBr in the NaCl phase at low temperature on an amorphous substrate by Blackman and Kahn raises an interesting question regarding the phase stability of the CsCl phase at lower temperatures. At least one modern paper has posited a phase change to explain anomalous electrical behavior observed in TlBr when cooling past $\sim$ 180 K.[10]. A vast majority of reports of measurements of bulk TlBr at low temperatures assume a CsCl structure and ignore the possibility of a phase change. The reports of TlBr thin films existing in phases other than CsCl all note that thicker films revert to the CsCl structure, making it unlikely that bulk TlBr undergoes a phase change at low temperature. If a phase change does occur however, many of the results described both in literature and in this dissertation would be affected. As an example, all of the thermal and optical activation energies for traps measured with PICTS, Cl, and PL reported in this dissertation are referenced to the band structure of CsCl-type TlBr. If the crystal structure of the measured samples changed upon cooling, these results would need to be referenced to the band structure of the new phase.

In this chapter, first principles calculations of the band structures of TlBr with NaCl and orthorhombic structures are presented, and compared to experimental data. The calculations were performed by Yuzhi Zhou. To distinguish notation for the three phases of TlBr, the convention of Landolt-Bornstein is used: TlBr(I) denotes the CsCl phase, TlBr(II) denotes the orthorhombic phase, and TlBr(III) corresponds to the NaCl phase.

A.2 Phase Stability and Band Structures for TlBr(I), TlBr(II), and TlBr(III)

A.2.1 Description of Density Functional Theory Calculations

Density functional calculations were performed using the plane-wave DFT software package VASP.[120] In order to improve the potential accuracy of the calculated band structure, a PBE0 hybrid functional was used in this study.[121] With the PBE0 functional, 25% of

exact Hartree-Fock exchange energy is mixed with 75% of the exchange energy from the general gradient approximation proposed by Perdew, Burke, and Ernzerhof (PBE) to represent the total exchange energy.[122] With this hybrid functional, the direct and indirect gaps of TlBr in the CsCl phase have been reported and shown to be quite close to experimental values.[62] The correlation energy was described using a PBE functional, and electron-ion interactions were treated with projector augmented wave (PAW) potentials.[123] The convergence of the cutoff energy and k-point grids was tested. All calculations were performed in a plane-wave basis with a 320 eV cutoff energy. For the three phases considered, three different k-point grids were used to sample the Brillouin zone. A 666 Monkhorst-Pack grid was used to sample the Brillouin zone of the CsCl structure. A 466 grid was used for the orthorhombic structure, and a 444 grid was used for the NaCl structure. Spin-orbit coupling was included in all calculations. The unit cells of the three phases were fully relaxed until the Hellmann-Feynman force was below 0.02 eV/ $\AA$.

A.2.2 Summary of Results

First principles calculations were done to determine the relative phase stability of the three phases. The results are presented in Table A.1. It was found that the most stable phase at a temperature of 0 K is the NaCl phase, followed by the orthorhombic, and finally the CsCl structure observed at room temperature. Thus, the CsCl phase observed at room temperature is the least energetically favorable of the three at 0 K, suggesting that a phase transition at low temperature is possible.

Table A.1: Relative Stability of Three Phases for TlBr

Phase	Free Energy [eV]
CsCl	-10.2061
Orthorhombic	-10.2501
NaCl	-10.2917

The band structure of all three phases was calculated. A summary of the results is given in Table A.2. The calculated values for the CsCl structure are extremely close to the experimental values for the indirect and direct gaps of TlBr, which are approximately 2.68 eV and 3.02 eV at low temperatures (see Chapter 4).

A.2.3 Comparison of Calculated Band Structures and Experiments

As previously noted, the agreement between the experimental and calculated bandgaps for the CsCl phase is excellent. Much less experimental literature exists probing the band structure of the other phases of TlBr. However, at least two experimental studies employing

Table A.2: Direct and Indirect Bandgaps for Three Phases of TlBr

Phase	Indirect Gap [eV]	Direct Gap [eV]
CsCl	2.69	3.05
Orthorhombic	N/A	3.33
NaCl	N/A	3.34

absorption and electroabsorption measurements of TlBr thin films stabilized in the NaCl phase report direct bandgaps near 3.30 eV and at 3.33 eV respectively.[124, 125] These values are in excellent agreement with the the calculated value of 3.34 eV. Thus, the PBE0 hybrid functional leads to very close agreement between calculated and experimental bandgap values for at least two phases of TlBr.

In the PL measurements reported in Section 4.3.2, narrow emission peaks near 3.36 eV were observed. Narrow peaks in PL measurements often correspond either to intrinsic transitions related to the band structure, or interatomic transitions. The value of 3.36 eV is in excellent agreement with calculated band structures if the peak is interpreted as a direct bandgap transition in either TlBr(II) or TlBr(III). The peaks near 3.36 eV show up predominantly in unpolished TlBr samples, suggesting a relationship between the peak and the surface quality. It is possible that both TlBr(II) and TlBr(III) phases are present on the surface of the unpolished TlBr samples at low temperature. Unfortunately, the peaks near 3.3 eV are unresolvable in PICTS spectra taken from samples at room temperature. Only upon cooling the unpolished samples to 8 K do the peaks become evident. Thus, if the PL peaks near 3.36 eV seen at 8 K are related to the NaCl and orthorhombic phases of TlBr, it is not possible to determine whether the two other phases of TlBr nucleate as the sample is cooled or whether the phases are stabilized at thes surface and present even at room temperature.

A.3 Conclusion

Calculated band structures performed by Yuzhi Zhou for three phases of TlBr observed in thin films have been reported in this chapter. Phase stability calculations show that the CsCl phase of TlBr is the least energetically favorable of the three phases at zero temperature. However, it is still unknown whether bulk TlBr undergoes a phase change at low temperature. Literature reports of TlBr thin film growth all find that TlBr assumes a CsCl structure beyond a critical thickness of approximately one to two hundred angstroms. Thus, it is unlikely that bulk TlBr undergoes a phase transition at low temperature. Nevertheless, it is reasonable to interpret several peaks seen near 3.3 eV with PL measurements on unpolished TlBr samples as evidence for mixed phases in TlBr at low temperature, as these energies correspond very well to the calculated and observed direct transitions in TlBr(II) and TlBr(III). Because the peaks were only seen on unpolished samples however, the mixed

phases are likely to exist only at the surface. From the PL data alone, it is not possible to determine whether the mixed phases nucleate as the TlBr samples are cooled, or whether they are present on the surface even at room temperature.

Appendix B

Mathematica Notebook for PICTS Analysis

B.1 PICTS Analysis Notebook

This *Mathematica* notebook was written to perform 2- and 4-gate analysis on PICTS data recorded with the system described in this dissertation. The program loads the raw PICTS data, computes 2- and 4-gate spectra, and allows Arrhenius analysis of the resulting traps in teh spectra. The steps of the program are commented.

A. Visualizing the raw data

In this section, the raw PICTS data is visualized to see what the recorded current transients look like at different temperatures, before the analysis begins.

1. Enter information about where the files are and what they consist of

In[5]:=
```
(* User inputs *)
WorkingDirectory =
  "C:\\Documents and Settings\\VT Hall\\My Documents\\Holland\\PICTS Data\\SI
    GaAs\\112111 SI GaAs #6 The Definitive Run - 2 sensors\\tsens2";
samplingFrequency = 1 000 000;
fileHeaderLength = 8;
SetDirectory[WorkingDirectory];
TempFileNames = FileNames["TEqu*.txt"];
Print[StringForm["There are `` files in the directory.", Length[TempFileNames]]]
SamplesRead = Length[Import[FindFile[TempFileNames[[1]]], "table"]] - fileHeaderLength;
Print[StringForm["Each file has `` samples in it", SamplesRead]]
```

```
There are 532 files in the directory.

Each file has 145000 samples in it
```

2. Read in data from the files: Temperature, Current vs time data

This next code reads in the temperatures for which a current transient was recorded, and loads a logarithmically sampled amount of data points for each current transient at each temperature into memory.

In[15]:=
```
temperatureArray =
  Table[getTempFromT2[OpenRead[TempFileNames[[i]]]], {i, 1, Length[TempFileNames]}];
signalDataArray = getReducedSignalData[TempFileNames, SamplesRead];
```

3. Visualize the Data

In[19]:=
```
transientPlots = Table[ListLinePlot[signalDataArray[[i]], PlotRange → {All, All},
    PlotStyle → Black, Frame → True], {i, 1, Length[signalDataArray]}];
```

Printed by Mathematica for Students

In[148]:=
```
Manipulate[Show[transientPlots[[i]], ImageSize → 450, Axes → False,
  PlotRange → {{0, .0008}, All}, FrameLabel → {"time [s]", "Current"},
  LabelStyle → Directive[FontFamily → "Helvetica", 14, Bold],
  PlotLabel → Style[Framed[StringForm["T = `` K", temperatureArray[[i]]]],
    FontFamily → "Helvetica", 16, Bold]], {i, 1, Length[transientPlots], 1}]
```

Out[148]=

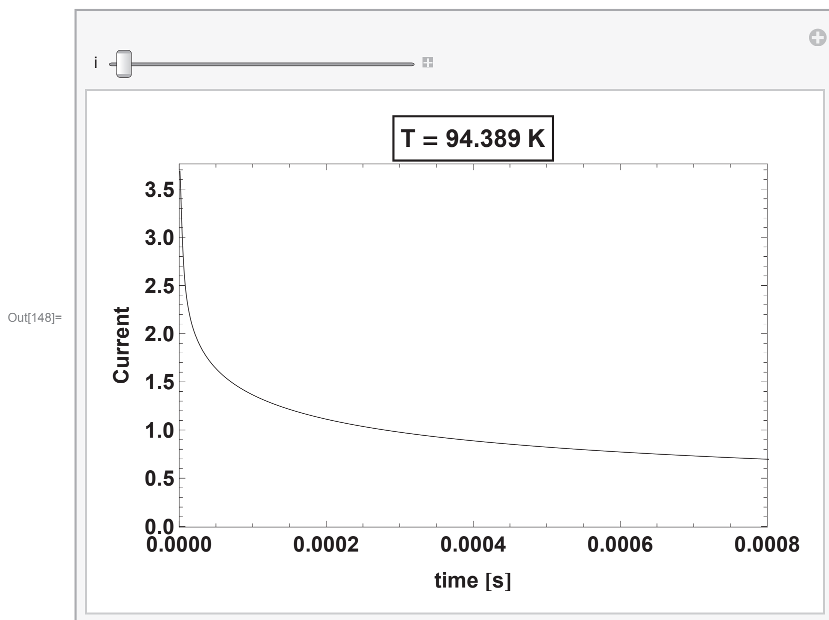

B. 4-Gate Analysis: Visualization

In this section, the sets of 4 gates that will be used to analyze the PICTS signal are chosen and displayed against the current transients to make sure they fall within a reasonable range where the signal is strong, and where the f astrecombination component of the transient is not relevant.

1. Choose the gates

In[58]:=
```
firstGate = 100;
closenessFactor = 1.2;
gateAdd = 43;
multiplier1 = 1 + (1 / closenessFactor);
multiplier2 = 7;
FinalT1Multiplier = multiplier2 * 10;
numSpectra = 30;
fourGateList =
 Table[{Round[(firstGate + (gateAdd * i))], Round[(firstGate + (gateAdd * i)) * multiplier1],
   Round[(firstGate + (gateAdd * i)) * multiplier2],
   Round[(firstGate + (gateAdd * i)) * FinalT1Multiplier]}, {i, 0, numSpectra - 1}]
```

Out[65]=
```
{{100, 183, 700, 7000}, {143, 262, 1001, 10 010}, {186, 341, 1302, 13 020},
 {229, 420, 1603, 16 030}, {272, 499, 1904, 19 040}, {315, 578, 2205, 22 050},
 {358, 656, 2506, 25 060}, {401, 735, 2807, 28 070}, {444, 814, 3108, 31 080},
 {487, 893, 3409, 34 090}, {530, 972, 3710, 37 100}, {573, 1050, 4011, 40 110},
 {616, 1129, 4312, 43 120}, {659, 1208, 4613, 46 130}, {702, 1287, 4914, 49 140},
 {745, 1366, 5215, 52 150}, {788, 1445, 5516, 55 160}, {831, 1524, 5817, 58 170},
 {874, 1602, 6118, 61 180}, {917, 1681, 6419, 64 190}, {960, 1760, 6720, 67 200},
 {1003, 1839, 7021, 70 210}, {1046, 1918, 7322, 73 220}, {1089, 1997, 7623, 76 230},
 {1132, 2075, 7924, 79 240}, {1175, 2154, 8225, 82 250}, {1218, 2233, 8526, 85 260},
 {1261, 2312, 8827, 88 270}, {1304, 2391, 9128, 91 280}, {1347, 2470, 9429, 94 290}}
```

2. Visualize the gates

In[66]:=
```
gateGraphics = getGateGraphics[fourGateList];
```

In[67]:=
```
logTransientPlots = Table[ListLogPlot[signalDataArray[[i]], PlotRange → {All, All},
    PlotStyle → Black, Joined → True, Frame → True], {i, 1, Length[signalDataArray]}];
```

In[149]:=
```
Manipulate[
 Manipulate[Show[logTransientPlots[[i]], gateGraphics[[j]], ImageSize → 450, Axes → False,
   PlotRange → {All, {Log[.001], Log[10]}}, FrameLabel → {"time [s]", "Log Current"},
   LabelStyle → Directive[FontFamily → "Helvetica", 16, Bold],
   PlotLabel → Style[Framed[StringForm["T = `` K", temperatureArray[[i]]]],
     FontFamily → "Helvetica", 20, Bold]],
  {i, 1, Length[transientPlots], 1}], {j, 1, Length[gateGraphics], 1}]
```

Out[149]=

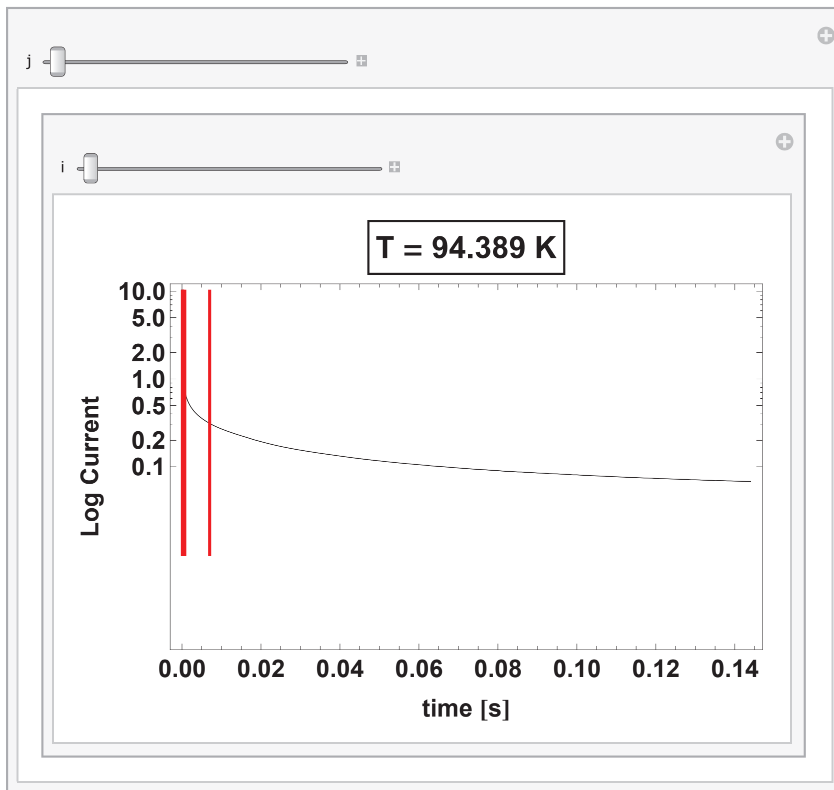

In[150]:=
```
Manipulate[
 Manipulate[Show[logTransientPlots[[i]], gateGraphics[[j]], ImageSize → 450, Axes → False,
   PlotRange → {{0, .01}, {Log[.001], Log[10]}}, FrameLabel → {"time [s]", "Log Current"},
   LabelStyle → Directive[FontFamily → "Helvetica", 16, Bold],
   PlotLabel → Style[Framed[StringForm["T = `` K", temperatureArray[[i]]]],
     FontFamily → "Helvetica", 20, Bold]],
  {i, 1, Length[transientPlots], 1}], {j, 1, Length[gateGraphics], 1}]
```

Out[150]=

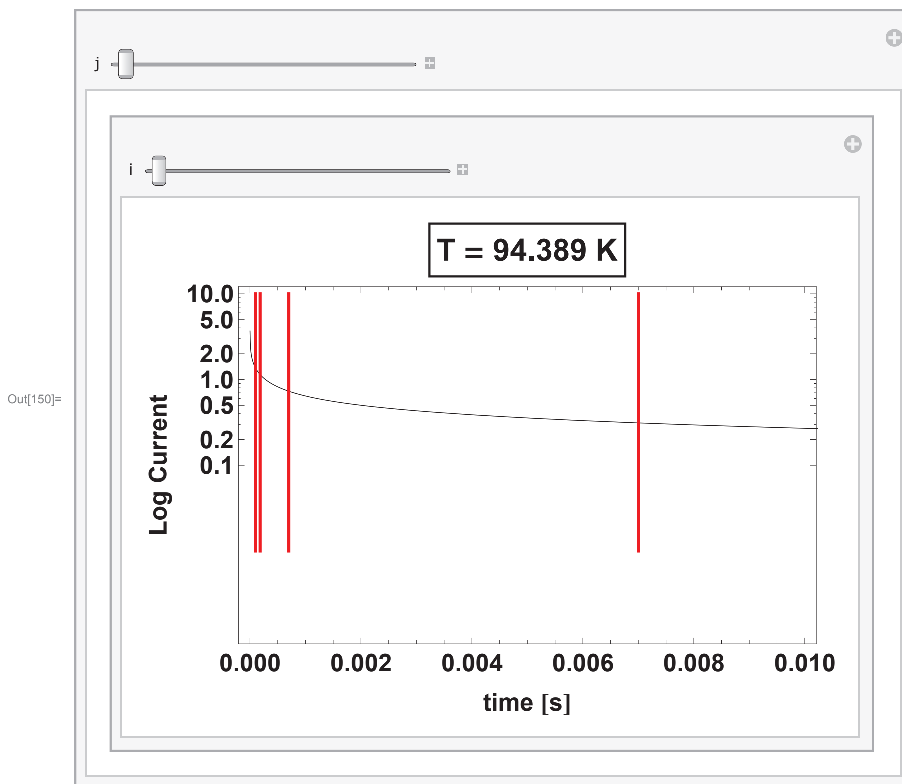

C. Computing the 4-Gate (and 2-Gate) Spectra

In this section, the 4-gate and 2-gate PICTS spectra are computed (as described in Chapter 2).

1. Get the points from the files

In[71]:=
```
fourGates = getFilePointsFromFourGateList[fourGateList, TempFileNames];
```

In[72]:=
```
(* These are the actual times,
which could be used later for calculating the emission rates *)
fourGateTimes = Table[{fourGates[[1]][[j]][[1]][[1]],
    fourGates[[1]][[j]][[2]][[1]], fourGates[[1]][[j]][[3]][[1]],
    fourGates[[1]][[j]][[4]][[1]]}, {j, 1, Length[fourGates[[1]]]}];
rateWindowsInMilliseconds = Table[(fourGateTimes[[i]][[3]] - fourGateTimes[[i]][[2]]) *
    10^3, {i, 1, Length[fourGateTimes]}];
```

2. Compute the spectra

In[74]:=
```
picts4GateSpectra = produceTrueFourGateSpectrum[temperatureArray, fourGates];
picts2GateSpectra = produceTrueTwoGateSpectrum[temperatureArray, fourGates];
```

3. Plot the Spectra

4 Gate Spectra:

In[153]:=
```
fourGatePlots = Table[ListLinePlot[picts4GateSpectra[[i]], PlotStyle → {ColorList[[i]]},
    PlotRange -> {All, {0.2, 0.6}}], {i, 1, Length[picts4GateSpectra]}];
masterPlot = Show[fourGatePlots, PlotRange → {All, All}, Frame → True,
  FrameLabel → {"T [K]", "Four Gate Signal [A.U.]"},
  LabelStyle → Directive[FontFamily → "Helvetica", 14, Bold], ImageSize → 450]
```

Out[154]=

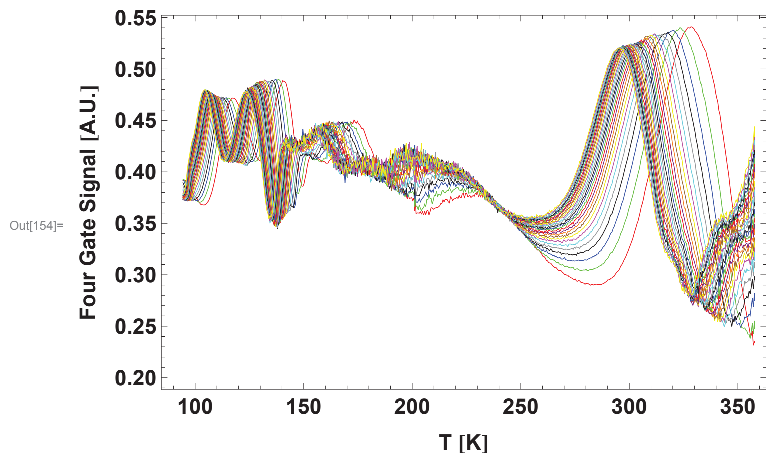

In[157]:=
```
Manipulate[Show[fourGatePlots[[i]], PlotRange → {All, All}, Frame → True, PlotLabel →
   Style[Framed[StringForm["Rate Window: `` ms", rateWindowsInMilliseconds[[i]]]],
    FontFamily → "Helvetica", 14, Bold], FrameLabel → {"T [K]", "Four Gate Signal [A.U.]"},
  LabelStyle → Directive[FontFamily → "Helvetica", 14, Bold], ImageSize → 450],
 {i, 1, Length[fourGatePlots], 1}]
```

Out[157]=

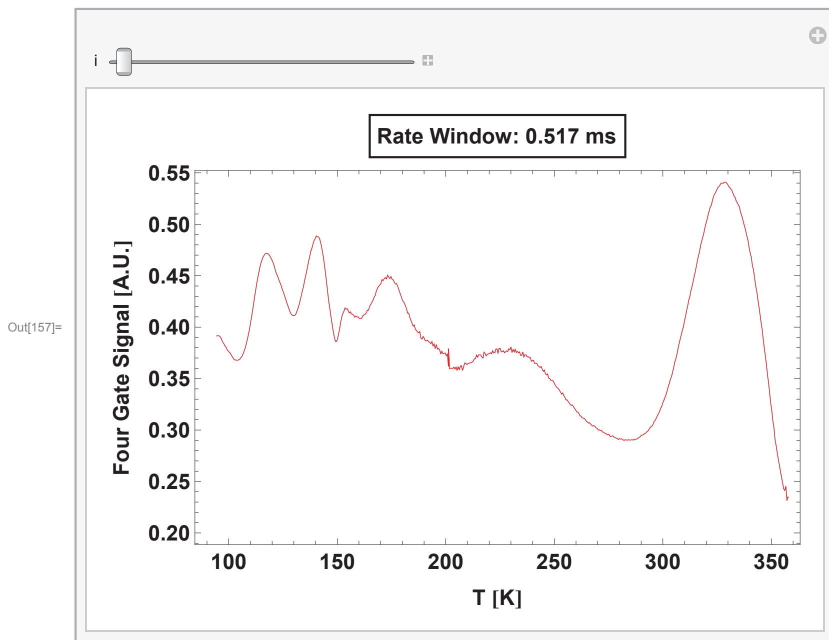

2 Gate Spectra:

In[79]:=
```
twoGatePlots = Table[ListLinePlot[picts2GateSpectra[[i]], PlotStyle → {ColorList[[i]]},
    PlotRange -> {All, All}], {i, 1, Length[picts4GateSpectra]}];
```

```
In[159]:= Show[twoGatePlots, PlotRange → {All, All},
  Frame → True, FrameLabel → {"T [K]", "Four Gate Signal [A.U.]"},
  LabelStyle → Directive[FontFamily → "Helvetica", 14, Bold], ImageSize → 450]
```

Out[159]=

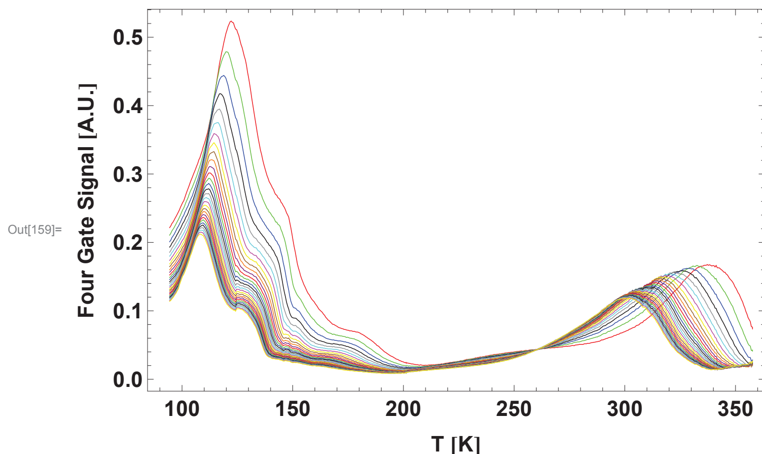

Comparison of Four-Gate and Two-Gate:

```
In[160]:= Show[twoGatePlots[[1]], fourGatePlots[[2]], PlotRange → {All, All},
  Frame → True, FrameLabel → {"T [K]", "Four Gate Signal [A.U.]"},
  LabelStyle → Directive[FontFamily → "Helvetica", 14, Bold], ImageSize → 450]
```

Out[160]=

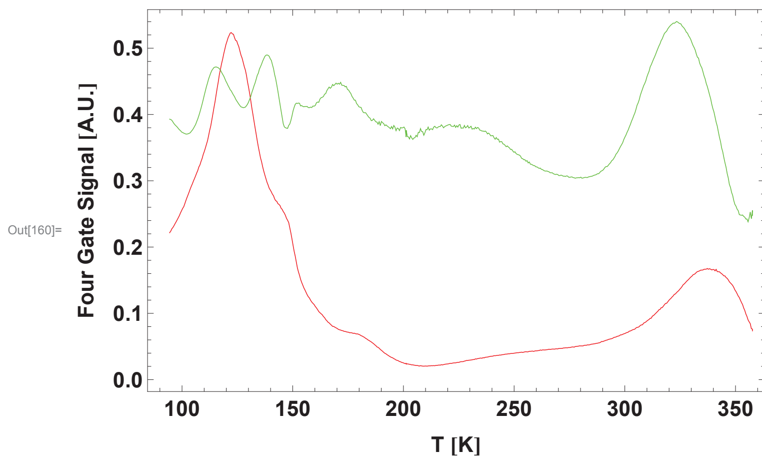

Trap peaks are much more clearly resolved in the 4-gate spectrum displayed above, compared to the 2-gate spectrum. Thus, the four-gate spectra are used for further Arrhenius analysis. The two-gate spectrum is shown just for comparison.

D. Analyze a Peak

In this section, a specific deep level is isolated and analyzed according to the Arrhenius analysis presented in chapter 2.

1. Pick a peak to analyze

```
In[161]:= masterPlot
```

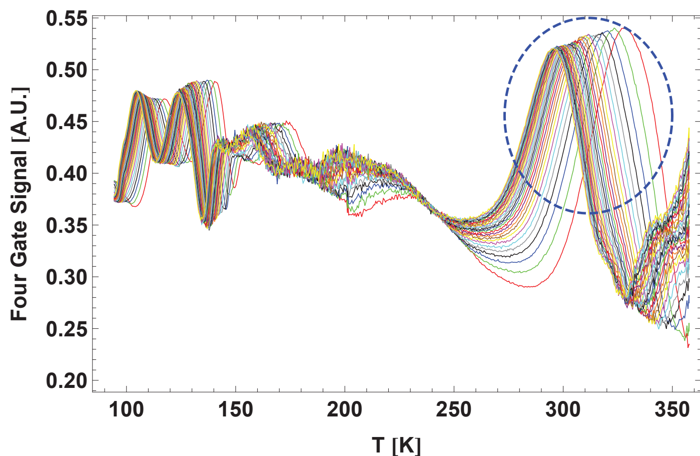

2. Fit the peak to get the maxima (recall - each maximum is one e_n(T))

In order to find the emission rate of the trap under analysis as a function of temperature, the maximumh of the peaks in each spectrum must be found. In the following code, the peaks are fit to Gaussians in order to find the maxima.

In[162]:=
```
plotToShow = fourGatePlots;
spectraToUse = picts4GateSpectra;
LowerTemp = 280;
UpperTemp = 350;
LowerVolt = 0.3;
UpperVolt = .55;
Show[plotToShow, AxesOrigin → {LowerTemp, LowerVolt},
 PlotRange → {{LowerTemp, UpperTemp}, {LowerVolt, UpperVolt}},
 Frame → True, FrameLabel → {"T [K]", "Four Gate Signal [A.U.]"},
 LabelStyle → Directive[FontFamily → "Helvetica", 16, Bold], ImageSize → 450]
```

Out[168]=

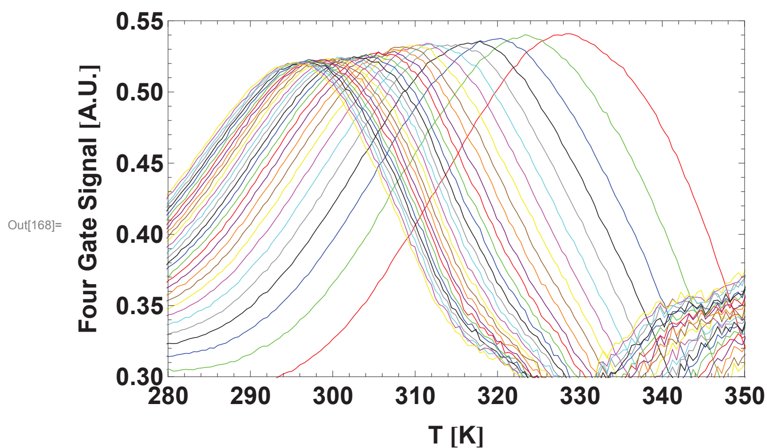

In[89]:=
```
OffsetsandAmps =
  {{329.5, 0.5377}, {324.2, 0.5363}, {319.9, 0.5356}, {315.9, 0.5314}, {313.3, 0.5272},
   {312.3, 0.5335}, {310.2, 0.5349}, {308.7, 0.5258}, {307.3, 0.5181}, {306.8, 0.5139},
   {306.6, 0.5097}, {306, 0.5153}, {306, 0.5286}, {306, 0.5349}, {304.3, 0.5426},
   {303.7, 0.5328}, {303.6, 0.5286}, {302.8, 0.5167}, {302.5, 0.5118}, {302.3, 0.509},
   {301.9, 0.5061}, {301.1, 0.5026}, {300.6, 0.5012}, {299.5, 0.5005}, {299.1, 0.5026},
   {298.8, 0.5068}, {298.8, 0.5167}, {298.6, 0.5223}, {297.8, 0.53}, {296.8, 0.5237},
   {296.8, 0.5202}, {295.7, 0.5139}, {295.2, 0.5097}, {294.2, 0.5111}, {293.5, 0.5153}};
TEndPoints = getQuadraticTempEndpoints[{288, 312}, {310, 335}, 30];
```

In[169]:=
```
temperatureIndices = ConvertEndpointArrays[spectraToUse, TEndPoints]
gaussianFits = findGaussianFits[spectraToUse, temperatureIndices, OffsetsandAmps];
plotDataWithFits[spectraToUse, gaussianFits, temperatureIndices, TEndPoints];
plotsOfJustFits = Table[Plot[A * Exp[- ((x - XOffset) ^2) / σ] /. gaussianFits[[i]],
    {x, TEndPoints[[i]][[1]], TEndPoints[[i]][[2]]},
    PlotStyle → {ColorList[[i]], Dashed, Thick}], {i, 1, Length[arrFits]}];
plotOfGaussianFits = Show[plotsOfJustFits, plotToShow,
  PlotRange → {{LowerTemp, UpperTemp}, {LowerVolt, UpperVolt}}, Frame → True,
  Axes → False, FrameLabel → {"T [K]", "Four Gate Signal [A.U.]"},
  LabelStyle → Directive[FontFamily → "Helvetica", 16, Bold], ImageSize → 450]
```

Out[169]=
```
{{439, 485}, {435, 481}, {432, 479}, {428, 475}, {426, 473}, {422, 469},
 {420, 467}, {418, 463}, {416, 461}, {412, 459}, {410, 457}, {408, 455},
 {406, 453}, {404, 451}, {402, 449}, {402, 447}, {400, 445}, {398, 443},
 {396, 443}, {396, 441}, {394, 439}, {394, 439}, {392, 437}, {392, 437},
 {392, 437}, {390, 435}, {390, 435}, {390, 435}, {390, 435}, {390, 435}}
```

Out[173]=

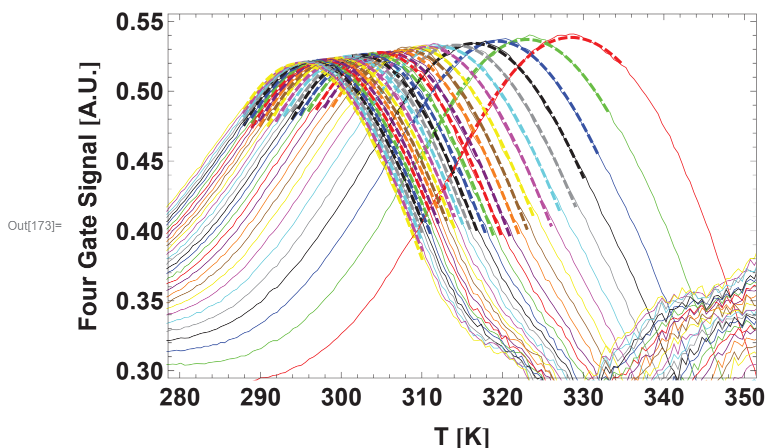

3. Make the Arrehnius Plot

In[178]:=
```
criticalRates = computeCriticalEmissionRate[fourGateTimes];
criticalTemps = Table[XOffset /. gaussianFits[[i]][[2]], {i, 1, Length[gaussianFits]}];
FinalArrheniusPlotData =
  Table[{1 / criticalTemps[[i]], Log[criticalRates[[i]] / (criticalTemps[[i]]^2)]},
   {i, 1, Length[criticalTemps]}];
ArrhPlot = ListPlot[FinalArrheniusPlotData, PlotMarkers → Automatic,
  Frame → True, Axes → False, FrameLabel → {"1/T", "Ln[en(T)/T2]"},
  LabelStyle → Directive[FontFamily → "Helvetica", 14, Bold], ImageSize → 550]
```

Out[181]=

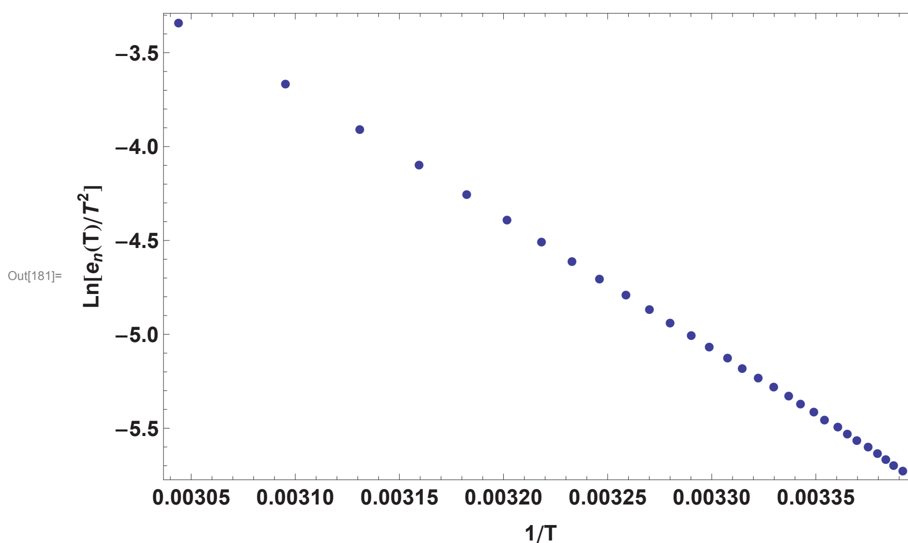

4. Fit the Plot, Extract Parameters of Interest

Once the Arrhenius Plot is constructed from the trap data, a line is fit to the plot and the activation energy and capture cross sections are calculated.

In[100]:=
```
plotTitle = "SI GaAs #6 - 11/21/2011";
startingPointToUse = 1;
endingPointToUse = 30;
McE = 1;
McH = 2;
MassE = 0.067 * ElectronMass;
MassH = 0.34 * ElectronMass;

linFit = LinearModelFit[
   FinalArrheniusPlotData[[startingPointToUse ;; endingPointToUse]], {x}, {x}];
Print["Activation Energy (from slope):"]
-Convert[(linFit[[1]][[2]][[2]] * (BoltzmannConstant * Kelvin)), ElectronVolt]
gammafacElectrons =
  Convert[ 2 * Sqrt[3] * McE * (2 * Pi) ^ (3 / 2) * BoltzmannConstant ^ 2 * MassE / PlanckConstant ^ 3,
   1 / (Kelvin ^ 2 * Centimeter ^ 2 * Second)];
gammaFacHoles = Convert[ 2 * Sqrt[3] * McH * (2 * Pi) ^ (3 / 2) * BoltzmannConstant ^ 2 *
    MassH / PlanckConstant ^ 3, 1 / (Kelvin ^ 2 * Centimeter ^ 2 * Second)];
Print["CC FOR ELECTRONS"]
ccElectrons = E ^ linFit[[1]][[2]][[1]] / gammafacElectrons * (1 / (Kelvin ^ 2 * Second))
Print["CC FOR HOLES"]
ccHoles = E ^ linFit[[1]][[2]][[1]] / gammaFacHoles * (1 / (Kelvin ^ 2 * Second))
```

Activation Energy (from slope):

Out[109]= 0.595553 ElectronVolt

CC FOR ELECTRONS

Out[113]= 2.29788×10^{-13} Centimeter^2

CC FOR HOLES

Out[115]= 2.26409×10^{-14} Centimeter^2

Finally, the calculated trap information is displayed in a clean plot.

In[182]:=
```
scaledFinalArrhPlotData =
  Table[{FinalArrheniusPlotData[[i]][[1]] * 1000, FinalArrheniusPlotData[[i]][[2]]},
   {i, 1, Length[FinalArrheniusPlotData]}];
scaledLinFit = LinearModelFit[scaledFinalArrhPlotData[[
    startingPointToUse ;; endingPointToUse]], {x}, {x}];
activationEnergy = -Convert[(linFit[[1]][[2]][[2]] * (BoltzmannConstant * Kelvin)),
    ElectronVolt];
activationEnergyContracted = NumberForm[activationEnergy / ElectronVolt, 3];
Rsquared = linFit["RSquared"];
dataPlot = ListPlot[scaledFinalArrhPlotData[[
    startingPointToUse ;; endingPointToUse]], PlotMarkers → Automatic];
fitPlot = Plot[scaledLinFit[x], {x, 1000 * 1 / criticalTemps[[Length[criticalTemps]]],
    1000 * 1 / criticalTemps[[startingPointToUse]]}, PlotStyle → {Black}];
infoString = StringForm["E_A: `` eV,     R^2: ``
 ccE: `` cm^2
 ccH: `` cm^2", activationEnergyContracted, NumberForm[Rsquared, 4],
   NumberForm[ccElectrons / Centimeter^2, 2], NumberForm[ccHoles / Centimeter^2, 2]];
infoGraphic = Graphics[Text[StyleForm[infoString,
     FontSize → 20, FontWeight → "Bold"], {3.3, -4}]];

Show[dataPlot, fitPlot, infoGraphic,
 Frame → True, FrameLabel → {"1000/T [K^-1]", "ln(En/T^2)"},
 LabelStyle → Directive[FontFamily → "Helvetica", 20, Bold],
 PlotLabel → plotTitle, ImageSize → 550]
```

Out[191]=

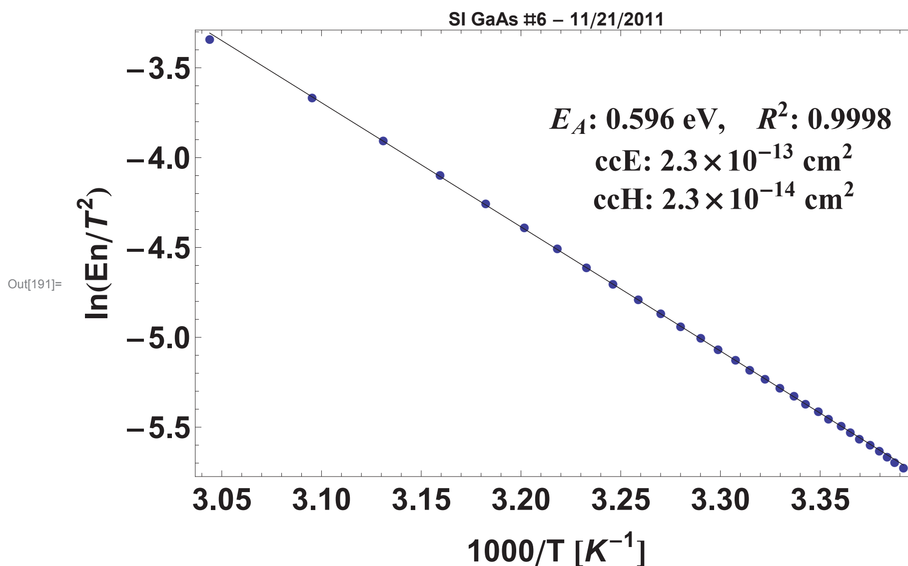

B.2 Additional Functions Used in PICTS Analysis Notebook

```
In[1]:= << Units`
        << PhysicalConstants`

In[3]:= ColorList = {Red, Green, Blue, Black, Gray, Cyan, Magenta, Yellow, Brown, Orange, Purple,
           Red, Green, Blue, Black, Gray, Cyan, Magenta, Yellow, Brown, Orange, Purple, Red,
           Green, Blue, Black, Gray, Cyan, Magenta, Yellow, Brown, Orange, Purple, Red, Green,
           Blue, Black, Gray, Cyan, Magenta, Yellow, Brown, Orange, Purple, Red, Green, Blue,
           Black, Gray, Cyan, Magenta, Yellow, Brown, Orange, Purple, Red, Green, Blue, Black,
           Gray, Cyan, Magenta, Yellow, Brown, Orange, Purple, Red, Green, Blue, Black, Gray,
           Cyan, Magenta, Yellow, Brown, Orange, Purple, Red, Green, Blue, Black, Gray, Cyan,
           Magenta, Yellow, Brown, Orange, Purple, Red, Green, Blue, Black, Gray, Cyan, Magenta,
           Yellow, Brown, Orange, Purple, Red, Green, Blue, Black, Gray, Cyan, Magenta, Yellow,
           Brown, Orange, Purple, Red, Green, Blue, Black, Gray, Cyan, Magenta, Yellow, Brown,
           Orange, Purple, Red, Green, Blue, Black, Gray, Cyan, Magenta, Yellow, Brown, Orange,
           Purple, Red, Green, Blue, Black, Gray, Cyan, Magenta, Yellow, Brown, Orange, Purple,
           Red, Green, Blue, Black, Gray, Cyan, Magenta, Yellow, Brown, Orange, Purple,
           Red, Green, Blue, Black, Gray, Cyan, Magenta, Yellow, Brown, Orange, Purple};

In[4]:= getTempFromT2[stream_] :=
         Module[{strm = stream}, Skip[strm, Record]; temp = Read[strm, Number]; Close[strm]; temp]

In[5]:= getVoltageAndTimePointsWorksWithDuplicates[stream_, pointArray_] :=
         Module[{strm = stream, arrPts = pointArray, gatesArr, fileLine, incrementer},
          Skip[strm, Record, 4 + arrPts[[1]]];
          gatesArr = Table[{i, i}, {i, 1, Length[arrPts]}]; incrementer = 0;
          Do[If[z + incrementer <= Length[arrPts], fileLine = ReadList[strm, Number, 2];
             gatesArr[[z + incrementer]][[1]] = fileLine[[1]]; gatesArr[[z + incrementer]][[2]] =
              fileLine[[2]]; If[z + incrementer < Length[arrPts], If[arrPts[[z + incrementer + 1]] ==
                 arrPts[[z + incrementer]], gatesArr[[z + incrementer + 1]][[1]] = fileLine[[1]];
               gatesArr[[z + incrementer + 1]][[2]] = fileLine[[2]]; incrementer += 1;]];
             If[z + incrementer < Length[arrPts], Skip[strm, Record,
                (arrPts[[z + incrementer + 1]] - arrPts[[z + incrementer]] - 1)]]],
           {z, 1, Length[arrPts]}]; Close[strm]; gatesArr]

In[6]:= getReducedData[reducedArray_, fileNames_] :=
         Module[{gates = reducedArray, files = fileNames},
          Table[getVoltageAndTimePointsWorksWithDuplicates[OpenRead[files[[j]]], gates],
           {j, 1, Length[files]}]]

In[7]:= getReducedSignalData[tempFileNames_, lengthFile_] :=
         Module[{temperatureFiles = tempFileNames, len = lengthFile,  part1, part2, part3,
           part4, part5, part6, arrPts, allReducedTransients, allReducedTransientPlots,
           arrTemperatures, fixedTransients}, part1 = Table[i, {i, 1, 100}];
          part2 = Table[i, {i, 102, 1000, 2}];
          part3 = Table[i, {i, 1010, 1500, 10}];
          part4 = Table[i, {i, 1600, 50 000, 100}];
          part5 = Table[i, {i, 51 000, len - 1000, 1000}];
          arrPts = Join[part1, part2, part3, part4, part5];
          allReducedTransients = getReducedData[arrPts, temperatureFiles];
          allReducedTransients]

In[8]:= getGateGraphics[gates_] := Table[
           Table[ListLogPlot[{{gates[[j]][[i]] / 1 000 000, .01}, {gates[[j]][[i]] / 1 000 000, 10}},
             Joined → True, PlotStyle -> {ColorList[[j]], Thick}],
            {i, 1, Length[gates[[1]]]}], {j, 1, Length[gates]}];
```

```
In[9]:= getFilePointsFromFourGateList[arrGates_, tempFileNames_] :=
  Module[{gates = arrGates, fileNames = tempFileNames, flattenedGates, gatesPlusIndices,
    sortedGatesAndIndices, pointsToGet, reducedDataOutOfOrder, reOrderingData,
    reSortedGates, numGroups, fourGates}, flattenedGates = Flatten[gates];
   gatesPlusIndices = Table[{i, flattenedGates[[i]]}, {i, 1, Length[flattenedGates]}];
   sortedGatesAndIndices = Sort[gatesPlusIndices, #1[[2]] < #2[[2]] &];
   pointsToGet =
    Table[sortedGatesAndIndices[[i]][[2]], {i, 1, Length[sortedGatesAndIndices]}];
   reducedDataOutOfOrder = getReducedData[pointsToGet, fileNames];
   reOrderingData = Table[
     Table[{reducedDataOutOfOrder[[i]][[j]], sortedGatesAndIndices[[j]][[1]]},
      {j, 1, Length[sortedGatesAndIndices]}], {i, 1, Length[reducedDataOutOfOrder]}];
   reSortedGates = Table[Sort[reOrderingData[[i]], #1[[2]] < #2[[2]] &],
     {i, 1, Length[reOrderingData]}];
   numGroups = Length[reSortedGates[[1]]] / 4;
   fourGates = Table[Table[
      {reSortedGates[[j]][[(i - 1) * 4 + 1]][[1]], reSortedGates[[j]][[(i - 1) * 4 + 2]][[1]],
       reSortedGates[[j]][[(i - 1) * 4 + 3]][[1]], reSortedGates[[j]][[(i - 1) * 4 + 4]][[1]]},
      {i, 1, numGroups}], {j, 1, Length[reSortedGates]}]; fourGates]

In[10]:= produceTrueFourGateSpectrum[temperatureArray_, fourPointgroups_] :=
  Module[{arrTemps = temperatureArray, points = fourPointgroups},
   Table[Table[{arrTemps[[j]], (points[[j]][[i]][[2]][[2]] - points[[j]][[i]][[3]][[2]]) /
        (points[[j]][[i]][[1]][[2]] - points[[j]][[i]][[4]][[2]])},
     {j, 1, Length[arrTemps]}], {i, 1, Length[points[[1]]]}]]

In[11]:= produceTrueTwoGateSpectrum[temperatureArray_, fourPointgroups_] :=
  Module[{arrTemps = temperatureArray, points = fourPointgroups},
   Table[Table[{arrTemps[[j]], (points[[j]][[i]][[1]][[2]] - points[[j]][[i]][[2]][[2]])},
     {j, 1, Length[arrTemps]}], {i, 1, Length[points[[1]]]}]]

In[12]:= linearPointModel[lowT_, highT_, numPoints_] :=
  Module[{lowTemp = lowT, highTemp = highT, points = numPoints, arrTemps},
   arrTemps = Table[N[lowT + (i / (numPoints - 1)) * (highT - lowT)], {i, 1, numPoints - 2}];
   arrTemps = Join[{lowT}, arrTemps]; arrTemps = Join[arrTemps, {highT}]]

In[13]:= quadraticPointModel[lowT_, highT_, numPoints_] :=
  Module[{lowTemp = lowT, highTemp = highT, points = numPoints, initialTemps, finalTemps},
   initialTemps = linearPointModel[lowT, highT, points];
   finalTemps = Table[Round[N[lowT + ((initialTemps[[i]] - lowT) ^ 2 / (highT - lowT))]],
     {i, 1, Length[initialTemps]}]; Reverse[finalTemps]]

In[14]:= getQuadraticTempEndpoints[lowRangePair_, highRangePair_, numPoints_] :=
  Module[{low = lowRangePair, high = highRangePair, points = numPoints, lowTs, highTs},
   lowTs = quadraticPointModel[low[[1]], low[[2]], points];
   highTs = quadraticPointModel[high[[1]], high[[2]], points];
   Table[{lowTs[[i]], highTs[[i]]}, {i, 1, Length[lowTs]}]]

In[15]:= ConvertTempToIndex[temperature_, arrTempValues_] :=
  Module[{temp = temperature, arrTs = arrTempValues},
   i = 1; While[arrTempValues[[i]] < temp, i ++]; (i - 1)]
```

```
In[16]:= ConvertEndpointArrays[spectraData_, arrTemperatureEndpoints_] := Module[
  {spectra = spectraData, arrTEndpoints = arrTemperatureEndpoints, leftGates, rightGates},
  leftGates = Table[ConvertTempToIndex[arrTEndpoints[[i]][[1]], spectra[[i]][[All, 1]]],
    {i, 1, Length[arrTEndpoints]}];
  rightGates = Table[ConvertTempToIndex[arrTEndpoints[[i]][[2]], spectra[[i]][[All, 1]]],
    {i, 1, Length[arrTEndpoints]}];
  Table[{leftGates[[i]], rightGates[[i]]}, {i, 1, Length[leftGates]}]]

In[17]:= findGaussianFits[arraySpectra_, temperatureEndpoints_, arrayAmplitudesAndOffsets_] :=
 Module[{arrSpectra = arraySpectra, tEndpoints = temperatureEndpoints,
   arrAmpsAndOffs = arrayAmplitudesAndOffsets, arrFits},
  arrFits = Table[FindFit[arrSpectra[[i]][[tEndpoints[[i]][[1]] ;; tEndpoints[[i]][[2]]]],
     A * Exp[- ((x - XOffset) ^ 2) / σ], {{A, arrAmpsAndOffs[[i]][[2]]},
      {XOffset, arrAmpsAndOffs[[i]][[1]]}, σ}, {x}], {i, 1, Length[arrSpectra]}]; arrFits]

In[18]:= plotDataWithFits[arraySpectra_, arrayFits_, arrTemperatureEndpointIndices_,
  arrTemperatures_] := Module[{arrSpectra = arraySpectra,
   arrFits = arrayFits, arrTIndices = arrTemperatureEndpointIndices,
   arrTemps = arrTemperatures, dataPlots, fitPlots}, dataPlots =
   Table[ListLinePlot[arrSpectra[[i]][[arrTIndices[[i]][[1]] ;; arrTIndices[[i]][[2]]]],
     PlotMarkers → Automatic, PlotStyle → {ColorList[[i]]}], {i, 1, Length[arrSpectra]}];
  fitPlots = Table[Plot[A * Exp[- ((x - XOffset) ^ 2) / σ] /. arrFits[[i]],
     {x, arrTemps[[i]][[1]], arrTemps[[i]][[2]]},
     PlotStyle → {ColorList[[i]], Dashed}], {i, 1, Length[arrFits]}];
  Table[Show[dataPlots[[i]], fitPlots[[i]]], {i, 1, Length[fitPlots]}]]

In[68]:= computeCriticalEmissionRate[arrayTaus_] :=
 Table[(1 / (arrayTaus[[i]][[3]] - arrayTaus[[i]][[2]])) *
   Log[(arrayTaus[[i]][[3]] - arrayTaus[[i]][[1]]) /
     (arrayTaus[[i]][[2]] - arrayTaus[[i]][[1]])], {i, 1, Length[arrayTaus]}]
```

Appendix C

Mathematica Notebook for Calculation of Photo-Generated Free Carrier Concentrations in MWPC Experiments

A *Mathematica* notebook to calculate the concentrations of free carriers in TlBr generated by laser light pulses during a MWPC experiment.

This notebook calculates the generation rate of free carriers in TlBr as a function of depth into the material using the following equation:

$G(x) = (1\text{-R})\ \alpha(h\nu)\Phi_o \exp[-\alpha(h\nu)\ x]$

In this equation, ***G*** is the rate, ***R*** is the surface reflectivity, α is the absorption coefficient, ***Φo*** is the incident photon flux, and ***x*** is the distance into the material from the illuminated surface

First, units and physical constants are imported.

```
In[1]:= << Units`
        << PhysicalConstants`
```

I. The case of excitation with below-bandgap laser light

In this section, the concentration of photo-generated free carriers as a function of depth is calculated for an excitation wavelength of 532 nm (2.33 eV). First, the necessary parameters are defined, with comments:

```
SurfaceReflectivity = .5; (* The surface reflectivity is likely much lower,
but this is a conservative guess*)
alpha = 10 Centimeter^-1;
(* There are no reports in literature of this value for TlBr. The value chose here
  is a reasonable low-end estimate based on similar results reported for sub-
 bandgap absorption in GaN (a wide indirect bandgap semiconductor like TlBr.) *)
areaOfBeam = (1 Milli Meter)^2;
(* The area of the laser spot used in an MWPC measurement *)
timeOfIllumination = 3 Nano Second; (* The duration of the laser pulse *)
energyOfPulse = 280 Micro Joule; (* The energy of the laser pulse *)
laserEnergyLow = N[1240 / 532] ElectronVolt;
(* The energy of laser used in the case of sub-bandgap excitation *)
illuminatedVolume = Convert[1 Milli Meter * 1 Milli Meter * 500 Micron, Centimeter^3];
(* This is the approximate dimension of the
 volume of the TlBr device illuminated with laser light *)
```

From these parameters, the flux can be calculated as follows:

```
In[10]:= laserPower = energyOfPulse / timeOfIllumination; (* Calculation of the laser power *)
         numberOfPhotons = Convert[energyOfPulse, ElectronVolt] / laserEnergyLow;
         PhiNaught = numberOfPhotons / ((timeOfIllumination) * areaOfBeam);
```

Now, the generation rate is defined:

```
In[13]:= generationRate[x_] := (1 - SurfaceReflectivity) * alpha * PhiNaught * Exp[-alpha * x];
```

To make sure everything is correct so far, we can perform a unit check:

```
In[14]:= Convert[generationRate[1 Micron], Centimeter^-3 * Second^-1]
```

Out[14]= $\dfrac{1.2484\times10^{26}}{\text{Centimeter}^3\ \text{Second}}$

These are the correct units. Now the generation rate as a function of depth is calculated from 0 to 3 mm, in order to be plotted.

```
In[15]:= belowBandgapPlotData =
           Table[{x, Log10[Convert[generationRate[Convert[x Micron, Centimeter]] *
                 timeOfIllumination, Centimeter^-3] * Centimeter^3]}, {x, 0, 3000}];
```

In[16]:=
```
ListLinePlot[belowBandgapPlotData, PlotStyle → {Black, Thick}, PlotRange → {All, All},
 Frame → True, FrameLabel → {"Depth [μm]", "Log10(Photo-generated
Carrier Concentration [cm^-3])"},
 LabelStyle → Directive[FontFamily → "Helvetica", 14, Bold],
 PlotRange → {{0, 300}, All}, ImageSize → 400]
```

Out[16]=

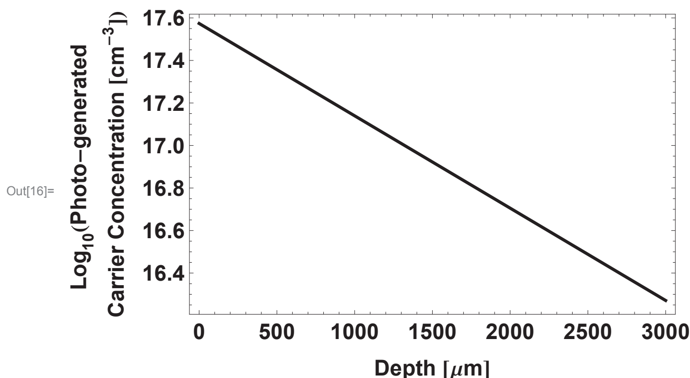

To estimate the number of free carriers generated by the below-bandgap laser pulse, we can integrate the rate and multiply by the volume as follows:

In[17]:=
```
NumberOfFreeCarriersGeneratedBelowBandGapCase =
 illuminatedVolume * Convert[Integrate[(1 - SurfaceReflectivity) * alpha * PhiNaught *
     Exp[-alpha * x Centimeter] * timeOfIllumination, {x, 0, .05}], Centimeter^-3]
```

Out[17]= 7.37545×10^{12}

II. The case of excitation with above-bandgap laser light

The same analysis is now repeated for an excitation wavelength of 355 nm (3.49 eV). Most of the parameters are the same as in the previous section, with a few differences noted in comments.

In[18]:=
```
SurfaceReflectivity = .5;
alpha = 10^5 Centimeter^-1;
(* This is an experimental value of alpha taken from Bachrach and Brown,
Phys.Rev.B,1:818-831,Jan 1970. *)
areaOfBeam = (1 Milli Meter)^2;
timeOfIllumination = 3 Nano Second;
energyOfPulse = 300 Micro Joule;
laserPower = energyOfPulse / timeOfIllumination;
laserEnergyHigh = N[1240 / 355] ElectronVolt; (* above-bandgap excitation *)
numberOfPhotons = Convert[energyOfPulse, ElectronVolt] / laserEnergyHigh;
PhiNaught = numberOfPhotons / ((timeOfIllumination) * areaOfBeam);
generationRate[x_] := (1 - SurfaceReflectivity) * alpha * PhiNaught * Exp[-alpha * x];
illuminatedVolume = Convert[1 Milli Meter * 1 Milli Meter * 500 Micron, Centimeter^3];
```

In[27]:=
```
aboveBandgapPlotData =
  Table[{x, Log10[Convert[generationRate[Convert[x Micron, Centimeter]] *
       timeOfIllumination, Centimeter^-3] * Centimeter^3]}, {x, 0, 20}];
```

In[28]:=
```
ListLinePlot[aboveBandgapPlotData, Axes → False,
 PlotStyle → {Red, Thick}, PlotRange → {All, All}, Frame → True,
 FrameLabel → {"Depth [μm]", "Log10(Photo-generated
Carrier Concentration [cm^-3])"},
 LabelStyle → Directive[FontFamily → "Helvetica", 14, Bold],
 PlotRange → {{0, 300}, All}, ImageSize → 400]
```

Out[28]=

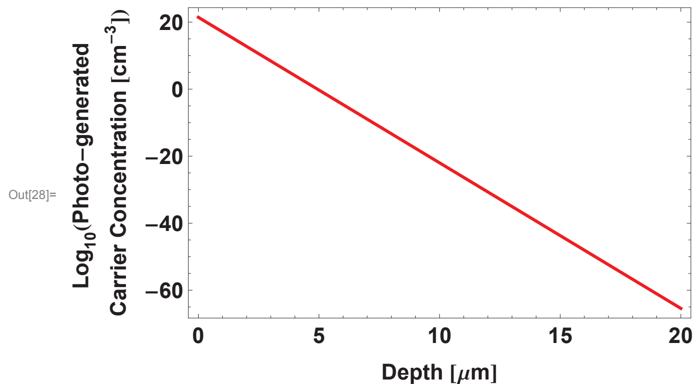

In[29]:=
```
NumberOfFreeCarriersGeneratedAboveBandGapCase =
 illuminatedVolume * Convert[Integrate[(1 - SurfaceReflectivity) * alpha * PhiNaught *
    Exp[-alpha * x Centimeter] * timeOfIllumination, {x, 0, .05}], Centimeter^-3]
```

Out[29]= 1.34016×10^{13}

III. A comparison of the depth profiles of photo-generated free carriers in the cases of above- and below-bandgap excitaiton.

In[30]:=
```
belowBandgapPlotForComparison = ListPlot[belowBandgapPlotData,
   Joined → True, PlotRange → {{0, 300}, {0, 25}}, PlotStyle → {Black, Thick}];
```

In[31]:=
```
aboveBandgapPlotForComparison = ListPlot[aboveBandgapPlotData,
   Joined → True, PlotRange → {{0, 300}, {0, 25}}, PlotStyle → {Red, Thick}];
```

In[33]:=
```
Show[belowBandgapPlotForComparison, aboveBandgapPlotForComparison,
  Frame → True, FrameLabel → {"Depth [μm]", "Log10(Photogenerated Carrier
Concentration [cm-3])"}, LabelStyle → Directive[FontFamily → "Helvetica", 20, Bold],
  PlotRange → {{0, 50}, All}, ImageSize → 550]
```

Out[33]=